This electronic thesis or dissertation has been downloaded from Explore Bristol Research, http://research-information.bristol.ac.uk

Author:
Safari, Ali

Title:
Improved Defect Characterisation Using Ultrasonic Arrays

General rights
Access to the thesis is subject to the Creative Commons Attribution - NonCommercial-No Derivatives 4.0 International Public License. A copy of this may be found at https://creativecommons.org/licenses/by-nc-nd/4.0/legalcode This license sets out your rights and the restrictions that apply to your access to the thesis so it is important you read this before proceeding.

Take down policy
Some pages of this thesis may have been removed for copyright restrictions prior to having it been deposited in Explore Bristol Research. However, if you have discovered material within the thesis that you consider to be unlawful e.g. breaches of copyright (either yours or that of a third party) or any other law, including but not limited to those relating to patent, trademark, confidentiality, data protection, obscenity, defamation, libel, then please contact collections-metadata@bristol.ac.uk and include the following information in your message:

- Your contact details
- Bibliographic details for the item, including a URL
- An outline nature of the complaint

Your claim will be investigated and, where appropriate, the item in question will be removed from public view as soon as possible.

Improved Defect Characterisation Using Ultrasonic Arrays

By

Ali Safari

Department of Mechanical Engineering

University of Bristol

A dissertation submitted to the University of Bristol in accordance with the requirements for award of the degree of Doctor of Philosophy in the Faculty of Engineering

December 2019

Word Count: 33,101

Abstract

There has been a rapid increase in the use of ultrasonic arrays for non-destructive evaluation with the aim of detecting and characterising defects which are detrimental to structural integrity. In parallel with this development, a variety of methods have been introduced to characterise defects using ultrasonic arrays, for example, by using imaging techniques or by extracting the scattering coefficient matrices of the defect. The aim of this thesis is to develop a methodology for improving defect characterisation using ultrasonic phased arrays, which consists of two key parts. The first part is to assess how a characterisation method performs by evaluating its spatial performance against a range of key variables including defect size and orientation. This is done by introducing a mapping approach and taking advantage of computer power and fast hybrid modelling techniques to simulate defects at different locations on a mesh-grid in front of the array and applying the characterisation methods to each simulated defect separately. The second part of the development of the methodology is to study the optimisation of arrays for defect characterisation by exploring the effect of array parameters and parameters associated with the sample and defect on characterisation. These parameters include; aperture size, centre frequency, material noise, defect type and geometric reflectors such as the back-wall. It is shown that different optimal arrays emerge, depending on how the optimal is defined, e.g. the optimal array might be the one that most accurately characterises the defect or produces a given level of characterisation accuracy using the minimum number of elements. It is also shown that the optimal array design varies depending on the size and orientation of the defect as well as its location.

Dedication and Acknowledgements

Firstly, I would like to express my sincere gratitude to my supervisors Prof. Bruce Drinkwater, Dr. Jie Zhang and Dr. Alexander Velichko for their continuous and invaluable support, guidance, patience and encouragements throughout my PhD. I would also like to specially thank Prof. Drinkwater for offering me this PhD position and providing funding from the UNDT group.

My sincere thanks also go to Prof. Paul Wilcox for reviewing my PhD annual progress and for providing such in-depth knowledge and helpful advices to improve my research.

I would like to thank all my friends and colleagues in the UNDT group for creating an amazing work environment and making this chapter of my life as fun and joyful as one could ever wish for.

I also wish to thank my mother (1961 – 2012), who, as a single mum, never doubted me and supported me all her life to see me grow and succeed. She has always encouraged and inspired me to be my best and her single biggest wish was to see me succeed academically and to attend my graduation ceremony.

I would also like to express my great appreciation to my father and brother for their support and encouragements throughout the years of my studies.

Last but not least, I would like to thank my dear wife, Mahya Entesari, for all her sacrifices, without which, this PhD would have not been possible. Thank you for always being there for me at some of the most difficult times of my life.

Author's Declaration

I declare that the work in this dissertation was carried out in accordance with the requirements of the University's *Regulations and Code of Practice for Research Degree Programmes* and that it has not been submitted for any other academic award. Except where indicated by specific reference in the text, the work is the candidate's own work. Work done in collaboration with, or with the assistance of, others, is indicated as such. Any views expressed in the dissertation are those of the author.

SIGNED: .... DATE: ....

Table of Contents

List of Figures:

List of Tables:

Chapter 1

Introduction

When solid structures go through typical operating conditions such as humidity and temperature variations and fatigue loading, defects such as cracks can start to form, which can eventually cause structural failure [1]. Thus, it is crucial to use reliable inspection and maintenance during manufacture and in-service operation in order to ensure safety and to protect the environment against catastrophic failures [2]. Non-destructive evaluation (NDE) [3–7] is extensively used in a wide range of safety critical applications, such as the aerospace [8–12], petroleum [13, 14], railway [15–24], and nuclear industries [25–28]. The prediction of the remaining life of a component in structural integrity assessments is enhanced by detection and characterisation of defects, which are the main objectives of NDE, and there are various techniques including (but not limited to) ultrasonic testing [6, 25, 29–31], eddy-current testing [32–38], X-ray computed tomography [39, 40], infrared thermography [26, 41] and magnetic flux leakage testing [42–45]. This thesis focuses on developing methodologies to improve non-destructive defect characterisation using ultrasonic arrays.

Ultrasonic arrays have seen a rapid increase in recent years in their non-destructive evaluation (NDE) applications due to their advantages over other NDE techniques [46]. Firstly, ultrasound is considered safe for humans and is capable of detecting surface defects as well as internal defects. In contrast, radiographic testing uses X-rays, one of the other widely used NDE techniques, which are harmful. Moreover, in order to increase penetration depth in radiography, stronger radiation is required which significantly adds to the safety concerns [47]. Secondly, ultrasonic arrays provide better inspection flexibility compared to single ultrasonic transducers as ultrasonic arrays are capable of combining the pulse-echo and pitch-catch inspection configurations [46]. This can significantly improve the imaging and post-processing capabilities of an ultrasonic system, which can enhance defect detection and characterisation.

Generally, there are two types of ultrasonic modelling for NDE, forward modelling and inverse problems. In forward modelling, the scattered field of a defect is calculated and in the inverse modelling, details of the target defect are obtained by measuring its scattering information [48]. Forward modelling can provide the basis for any inversion methods, and is said to be "inductive and predictive" [48] as the same base model can be used to solve scattered fields of multiple defects of distinct parameters (e.g., size and orientation angle). Ying et al. [49] studied the scattering of plane longitudinal waves by spherical defects and developed scattered field expressions for elastic spheres, spherical cavities, and rigid spheres. The scattering of elastic waves by a cylindrical cavity (which replicates the commonly used side-drilled hole test defect) was studied by Brind et al. [50] and a far-field solution to the scattering problem derived. In the NDE community, cracks are regarded as "the defects of most concern" [51] and are of particular interest, as they have regions of stress concentrations and can rapidly grow in a structure [52]. Hence, their scattering behaviour is widely studied in literature, including planar cracks [53], penny-shaped cracks [54], and surface-breaking cracks [55]. In this thesis, a fast semi-analytical algorithm developed by Glushkov et al. [56] is extensively used. In this method, the crack opening displacements are solved based on traction-free boundary conditions at crack sides and then the integral representation of the scattered wave field [57] is adopted in order to calculate the scattered field of the crack. In reality, naturally occurring cracks have some degree of roughness [58]. Ogilvy [59] and Thorsos [60] studied the forward modelling of rough cracks using the Kirchhoff approximation [61]. In their studies, the surface roughness correlation length was found to have a major impact on the Kirchhoff approximation away from the low grazing angle regions [60]. In another study, the performance of the Kirchhoff approximation was compared to a finite element local scattering model [62] it was concluded that the two methods have a difference of less than 8% when the incident and scattering angles are in the range [-80°, 80°] relative to the crack normal direction [58].

In case of defects with irregular or complex shapes, a numerical forward model is typically used as an analytic solution would be difficult to derive. Numerical models use methods such as finite elements [63], finite differences [64] or boundary element methods [65]. Frehner et al. [66] compared the finite element and finite difference approaches and it was found that the finite element method has the advantage of unstructured meshes compared to the finite difference method. Wilcox et al. [67] proposed a general finite element model which can solve the complete scattered field of any arbitrary scatterer in 2D geometries, and the same authors later generalised the model for 3-dimensional geometries and anisotropic media [62]. The benefit of the finite element local scattering model is that the size of the modelling domain is minimised by positioning the loading nodes around a region that encloses the defect [62].

In contrast, the inverse scattering problem is still a challenge to the NDE community, in particular, for the characterisation of small sub-wavelength defects and with the presence of measurement noise. Defect characterisation techniques have been studied by many authors in literature [37, 43, 75, 76, 46, 68–74], and cracks are frequently chosen as the main defect type. For example, the time-of-flight diffraction (TOFD) method measures the diffracted signals from crack tips and it was shown, under ideal conditions, to be able to measure the size of vertical cracks with a mean error of ±0.13 mm [71]. The scattering amplitude of cracks can also be directly measured for sizing a crack or a so-called 6dB drop approach [72] can be used. In this method, the crack is scanned in pulse-echo mode from an ultrasonic probe and the captured signal amplitude is used to size the crack by measuring the distance where the signal amplitude drops by 6dB (i.e. 1/2) from its peak value.

In recent years, with the development of ultrasonic arrays [46] and high-resolution imaging techniques, such as the total focusing method (TFM) [73] and the inverse wave field extrapolation (IWEX) method [74], the capabilities of ultrasonic imaging have seen a significant increase. It was shown that for cracks as small as 1.6λ, defect characterisation performs well when using an image-based 6dB drop approach [75]. For small surface-breaking cracks, a so-called half-skip TFM (HSTFM) has been proposed for more accurate characterisation [76]. The authors described the advantage of HSTFM as the capability to capture specular reflections from the crack face by altering the delay laws of the TFM. It was shown that the method can accurately size cracks as small as 0.5 mm (1.5λ) with an 18 MHz array [76].

Although there have been a variety of methods introduced to characterise defects using ultrasonic arrays (some of which have been discussed here and will be reviewed in more detail in the next Chapter), the robustness of these techniques is typically not fully understood, especially with regards to the location of defects relative to arrays, and there is no agreed methodology for assessing their performance. Instead, these methods are often assessed by simply applying them to a few specific defects located at specific positions and it is assumed that the performance is similar for other defects at other locations [68–70]. Moreover, ultrasonic phased arrays are typically designed to achieve optimal imaging performance, for example by keeping the pitch to half wavelength of the centre frequency to avoid grating lobes and selecting the highest frequency able to achieve adequate signal-to-noise performance at some predefined penetration depth. However, it is currently unknown whether an optimal phased array for detection and imaging is also optimal for defect characterisation in all scenarios and in what way and to what extent characterisation is affected by array parameters.

2.1 Aims and Objectives

The main objectives of this thesis are to develop an assessment methodology for defect characterisation using ultrasonic phased arrays and to explore the possibilities of array design optimisation for the sole purpose of characterising defects. In this thesis, a spatial assessment method is introduced to map the performance of characterisation algorithms against the key variables that affect their accuracy, such as the location, size and orientation angle of defects, as well as the extent of any structural noise. This will enable us to understand where the methods work best and where they fail as well as providing a basis for quantifying future developments. This thesis also aims to investigate the effect of ultrasonic array parameters on defect characterisation. In order to achieve this, it is assumed that the defect has been detected and the requirement is to determine its characteristics, i.e. size and orientation angle in the case of a crack. The effect of array parameters and parameters associated with the sample and the defect, which have a significant impact on characterisation accuracy, are then explored.

2.2 Thesis Outline

This thesis is organised as follows. In Chapter 2, the use of ultrasonic phased arrays for NDE applications is introduced. The different geometry designs with their benefits and disadvantages are discussed and their capabilities such as beam steering and focusing is explained. The concept of Full Matrix Capture (FMC) as well as the Scattering Coefficient Matrix (S-matrix) are also explored and their uses in NDE inspections, particularly in defect characterisation, are discussed. Some of the post processing methods for imaging and defect characterisation, such as Total Focusing Method (TFM) and a characterisation approach based on comparing the similarity of the scattering matrices are also presented in detail. The forward hybrid model, which is used throughout the thesis for the simulation of cracks and noise simulation, are described and validated in Chapter 3. First, the overall ray model is introduced and then the simulation of each term of the model, such as the input signal, beam spreading, directivity function and crack scattering coefficient matrix are explained in more detail. Chapter 4 introduces a spatial assessment method to map the performance of array-based characterisation methods against the key parameters, which have a significant impact on their accuracy. Then in a case study, a defect characterisation method is assessed and the key factors governing its performance are identified. In Chapter 5, the effect of ultrasonic array parameters specifically on defect characterisation is investigated and the possibility of optimised array designs for this purpose is explored. Using the scenario of an embedded crack, as a case study, an optimal array is then proposed based on the impact of different parameters, such as aperture size, centre frequency, material noise and defect type. Finally, the key findings of the thesis are briefly summarised in Chapter 6 and directions for future work are suggested.

Chapter 2

Literature Review of Phased Array Imaging and Defect Characterisation

2.1 Introduction

In this Chapter the use of ultrasonic phased arrays for NDE applications is introduced. The different geometry designs with their benefits and disadvantages are discussed and their capabilities such as beam steering and focusing is explained. The concept of Full Matrix Capture (FMC) as well as the Scattering Coefficient Matrix (S-matrix) are also explored and their uses in NDE inspections, particularly in defect characterisation, are discussed. Some of the post processing methods for imaging and defect characterisation, such as Total Focusing Method (TFM) are also presented.

2.2 Ultrasonic Arrays

Ultrasonic inspection has traditionally been performed using single or multiple transducers [77, 78]. A single transducer can be used both as a transmitter and a receiver to complete a pulse-echo testing. Other inspection methods have also been proposed where separate probes are used as transmitter and receiver. In these techniques, such as pitch-catch and through transmission inspections methods, transducers have a fixed angle and are able to illuminate a limited area within the test sample. In these methods, the probes need to be mechanically moved in order to create an image of the component. In case of the defects having a range of possible orientations, the inspection is carried out multiple times using probes of different angles.

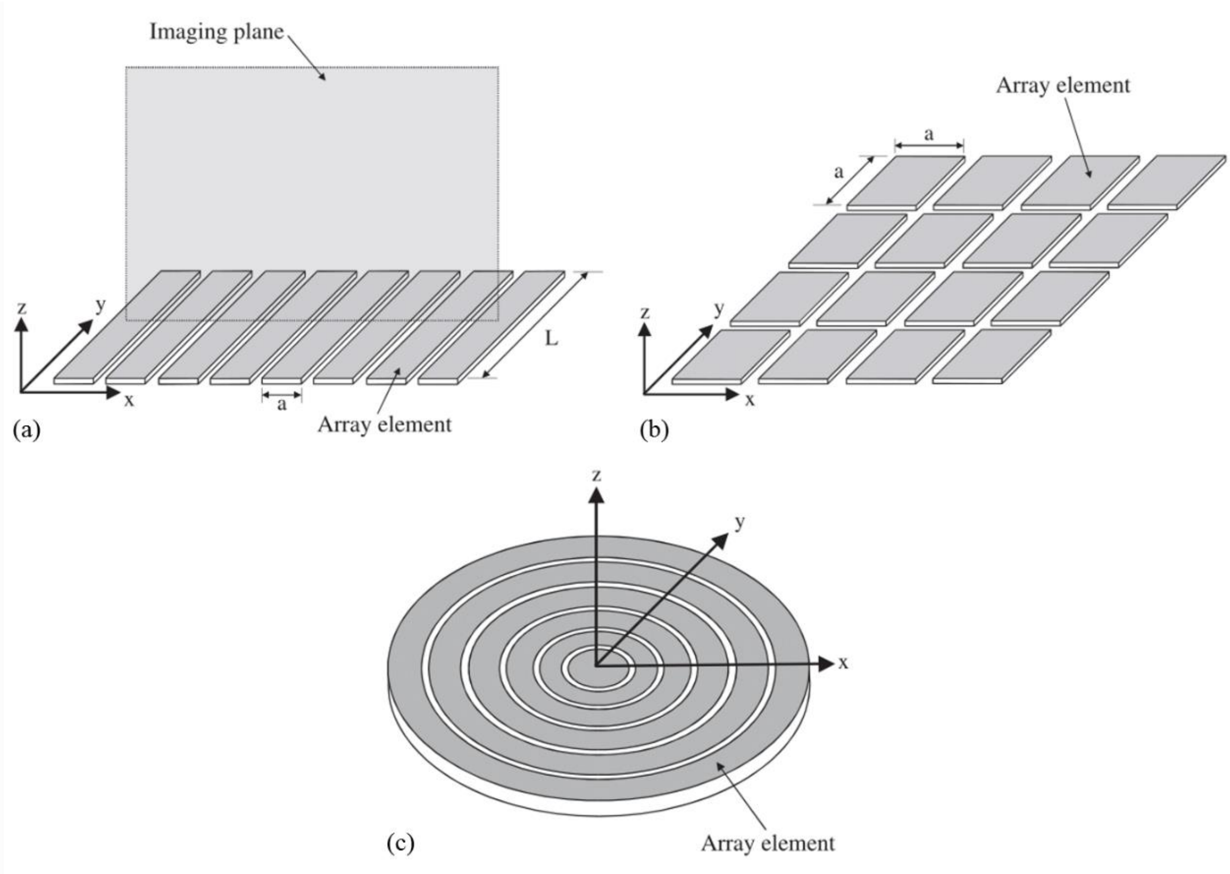

Figure 2.1: Common array transducer configurations: (a) 1D linear array, (b) 2D array and (c) annular array [46]**.**

Ultrasonic phased arrays are arrangements of individually connected transducers, which are referred to as the elements of the array. Generally, the arrangement of the elements within the array are classified as 1D, 2D or annular [46]. The most popular type of array in industry is a 1D linear array as shown in Figure 2.1 (a), where the array lies in the x-y plane and the normal direction is parallel to the z-axis. A 1D array using in this way produces a 2D image in the x-z plane. 1D arrays are able to steer and focus the beams within a 2D inspection plane. Figure 2.1

(b) shows a 2D or mosaic array, which contains a number of elements arranged in a 2D grid. There have been some work done on the optimisation of the grid configuration [79–81]. 2D arrays are capable of steering and focusing beams within a 3D inspection volume. In both 1D and 2D arrays, the steering and focusing range is limited by beam directivity and attenuation. Figure 2.1 (c) illustrates an annular array, which is circular arrangement of elements and does not allow beam steering, but it is capable of providing variable focal depths. Various array designs are also reviewed in detail in [46, 82].

2D arrays have a relatively complex operation and manufacture, which increases the difficulty and cost of production. The size of 2D arrays are also currently limited to a relatively small number of elements, which is due to the limitations in array controller technology and computing power. Thus, despite of the various applications discussed in [83, 84], they have not found widespread use in industry yet [46]. With regards to annular arrays, the lack of beam steering capability has limited its applications as defects can occur at a range of orientations in many inspections. Therefore, currently, 1D linear arrays are the most popular types of arrays in industry [46].

Elements within linear arrays are relatively long and narrow, which can be approximated as line sources, which produce a semi-cylindrical wavefront. The element width in the y-dimension in Figure 2.1 is considerably larger than the wavelength, which would minimise beam-spread in this dimension. Array elements are normally made from a piezocomposite material, due to the cross-talk reduction and bandwidth improvement that they offer [85].

In order to be able to independently manipulate elements, each element is separately connected to an electrical delay line, which is connected to a multiplexer. This allows beam steering and focusing in both transmission and reception [46]. The beam profile generated by a single element probe is defined by its mechanical design, which is fixed and cannot be changed [46]. However, array transducers have a greater flexibility and are capable of mimicking wave fields produced from multiple single element probes. This means a single ultrasonic array can be used to undertake several different inspections. Elements can be fired individually or as a group of elements (termed the aperture). They can be fired in-phase with each other to create a plane wave within the test sample or different delay and focal laws can be applied to each element in order to steer or focus the beam.

Figure 2.2 shows a schematic diagram of the operation of a 1D array for the case of beam steering. In order to generate the plane wavefront in Figure 2.2 (indicated by solid green line), a time delay must be applied to the two adjacent elements so that a constructive interference occurs along this line. This means the element 2 should be fired when the signal from the element 1 has travelled a distance r, which is given by:

$$r = p \sin \theta \tag{2.1}$$

where p is the element pitch (distance between the centres of two adjacent elements) and θ is the angle of steering. The relative time delay Δt for element 2, which is required for a wave to travel this distance is then given by:

$$\Delta t = \frac{r}{c} \tag{2.2}$$

where c is the speed of sound in the test medium.

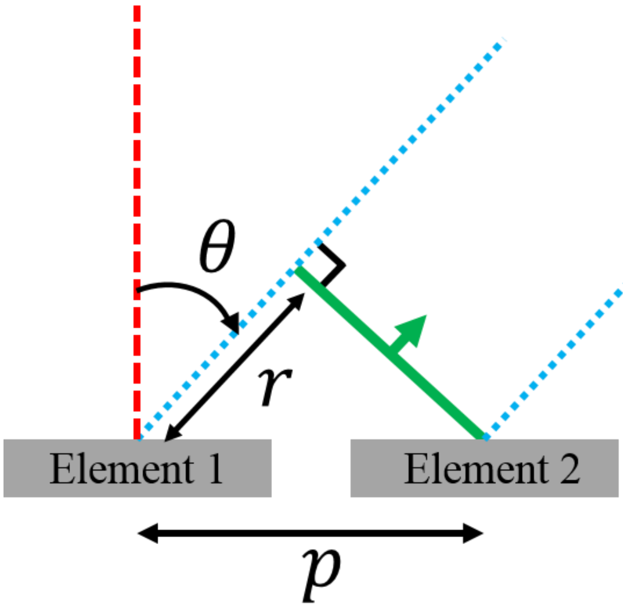

Figure 2.2: Schematic diagram of beam steering using a phased array. The red line is normal to the elements and the blue lines indicate the direction of beam steering

A potential downside with phased array transducers is the occurrence of grating lobes, which are due to the unwanted constructive interferences between the signals transmitted from each element [46]. Grating lobes are a property of all ultrasonic arrays and depend on element pitch, frequency and bandwidth [46]. Grating lobes occur at an angle defined by [86]:

$$\theta_{grating} = \sin^{-1}\left(\sin\theta_{steering} - \frac{n\lambda}{p}\right) \tag{2.3}$$

where $\theta_{steering}$ is array steering angle in radians, n is integer numbers (±1, ±2, …), λ is wavelength and p is the element pitch. By keeping the element pitch less than or equal to λ/2, grating lobes can be removed under all operational conditions.

Figure 2.3 illustrates the pressure field in a steel sample where a 32-element array with 5 MHz centre frequency is simulated and the delay laws are selected to create a beam steering at 45°. The wavelength at centre frequency (λ) in a steel sample where speed of sound is 5900 m/s is approximately 1.18 mm. Element pitch in Figure 2.3 (a) and (b) is 0.5 λ and 1 λ respectively and it can be seen that a grating lobe is clearly visible in (b).

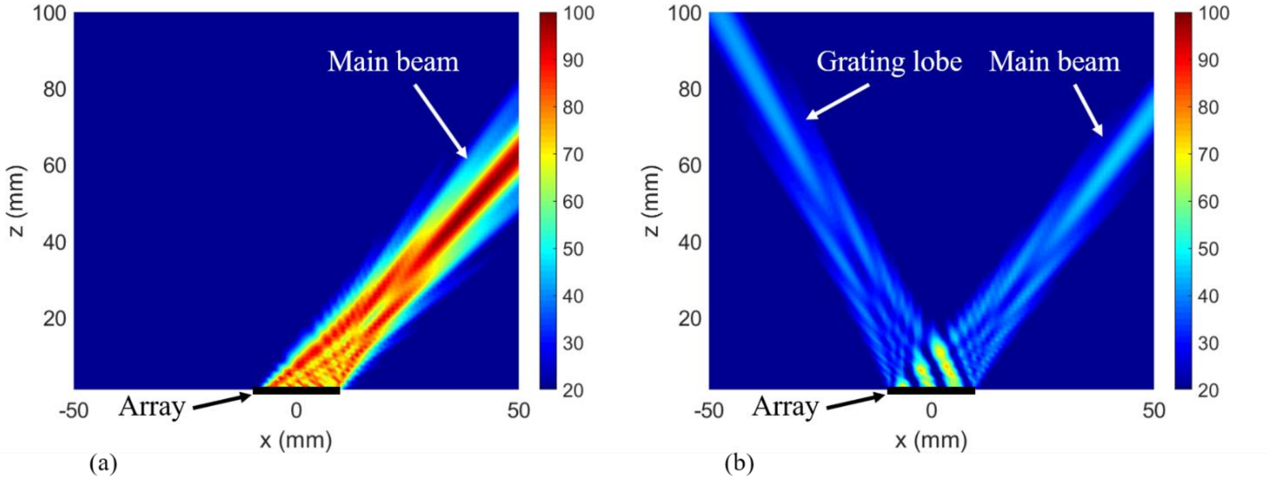

Figure 2.3: Pressure field simulated in a steel sample using a 32-element array with 5 MHz centre frequency and an element pitch of (a) 0.5 λ and (b) 1 λ. Delay laws are selected to steer beam at 45° in both cases.

2.2.1 Full Matrix Capture

Holmes et al. [73] demonstrated an array inspection approach, which is to capture the full matrix of data experimentally. This operation is referred to as full matrix capture (FMC). FMC is a matrix containing the time domain signals (A-Scans) transmitted and received by every single pair of elements within the array, such that if an array has N number of elements, the FMC would be a 3D $N \times N \times T$ matrix representing the corresponding signals to every pair of transmitter-receiver elements. This is the largest amount of data that can possibly be captured by an array at a given location and can be written as:

$$F(t) = \begin{bmatrix} f_{1,1}(t) & f_{1,2}(t) & \cdots & f_{1,N}(t) \\ f_{2,1}(t) & f_{2,2}(t) & \cdots & f_{2,N}(t) \\ \vdots & \vdots & \ddots & \vdots \\ f_{N,1}(t) & f_{N,2}(t) & \cdots & f_{N,N}(t) \end{bmatrix} \tag{2.4}$$

where $f_{i,j}$ represents the corresponding time domain signal transmitted from the i^{th} element and received by the j^{th} element. These signals are vectors themselves (amplitudes over equal intervals of time). The recent advances in computers mean that such large data (typically around 6 MB for a 64-element array with 2000 time intervals) can be quickly and easily captured and processed on a regular PC. Any post-processing algorithm can then be applied to the stored data set. This method also future-proofs the inspection as the more advanced algorithms developed in the future can be applied to the same data set. It should be noted that this approach has been used in the seismic field for some time [87] but it has not been used in NDE until recent research work. Holmes et al. [73] also introduced a post-processing technique, where the array is focused on every point in the field of view and termed this the total focusing method (TFM). This method is reviewed in more detail later in this Chapter.

2.3 Scattering Matrix

Figure 2.4 demonstrates a typical array measurement setup. The scattering coefficient field (S-matrix) [68, 69] of a defect consists of far-field scattering coefficients for different incident/scattering angles and describes how the ultrasonic wave is scattered by a defect at a given incident angle. This angular scattering information of the defect can be extracted from the FMC data set when measurements from all possible transmitter-receiver pairs are recorded (see section 2.4.2). A S-matrix is defined in 2D as [75]:

$$S(\theta_{in}, \theta_{sc}, \omega) = \frac{a_{sc}(\omega)}{a_{in}(\omega)}\sqrt{\frac{d_{sc}}{\lambda}}\, e^{-\frac{i\omega d_{sc}}{c}} \tag{2.5}$$

where θ_{in} and θ_{sc} are the incident and scattering angles respectively (as shown in Figure 2.4), ω is angular frequency, a_{in} is the amplitude of the incident plane wave, a_{sc} is the amplitude of the scattered wave, d_{sc} is the (far field) distance, where the scattering amplitude a_{sc} is measured, λ is the wavelength and c is the speed of sound in the test medium. Note that the incident and scattering waves can either be in longitudinal (L) or shear (S) modes. Thus, the S-matrix can be defined either in LL mode (i.e. longitudinal-incident-longitudinal-scattering), LS, SL or SS mode. Throughout this thesis, the LL S-matrix is used consistently as the adopted experimental measurement configurations in this thesis typically involve an ultrasonic array in direct contact mode, where the array elements are sensitive mostly to longitudinal waves. The incident and scattering angles refer to the clockwise angle from the array normal and the orientation angle of a defect, such as cracks, refers to the anti-clockwise angle from the horizontal (i.e. x dimension in Figure 2.4). Note that for a defect with size l, the far field assumption is valid if $l^2/\lambda z_0 < 1$ where z_0 is the distance from the array to the defect [88]. For example, for a defect that is located at (0, 20 mm) in a medium where the speed of sound is 6000 m/s and the frequency is 5 MHz, l should be smaller than 4.9 mm in order for the far field assumption of the defect to be valid. This expression is obtained from ultrasonic transducer theory where the pressure field from a circular transducer consists of a series of maxima and minima in the area near to the transducer, and then decays beyond this point [89]. Therefore, the near field length is defined as the distance between the transducer and the last maxima [77].

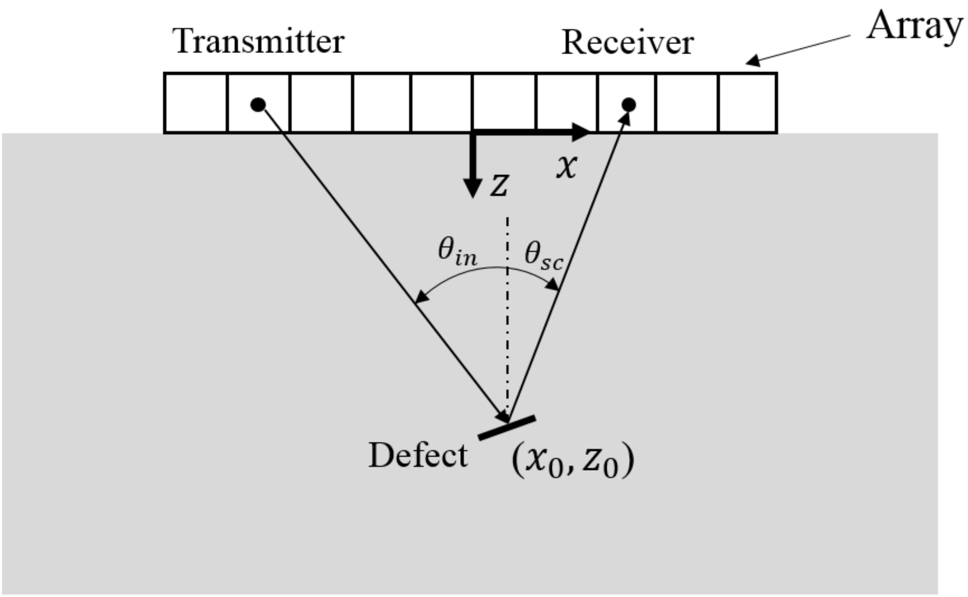

Figure 2.4: Schematic diagram of a typical linear ultrasonic array measurement setup.

There are different methods for modelling the S-matrix of a defect, such as in [50], which proposes an analytical solution for a side-drilled hole and [56], which describes a far field asymptotic solution for arbitrarily shaped and oriented planar cracks. For the other types of defects such as elliptical defects, rough cracks and surface-breaking cracks, a finite element local scattering (FELS) model [62] can be used to simulate the S-matrix. Modelling these S-matrices are useful to generate defect databases for characterisation purposes (explained in more detail in Chapter 3). Figure 2.5 (a) and (b) illustrate example S-matrices (amplitude) of a hole with 1λ diameter and a crack with 1λ length with 0º orientation angle. The differences between the S-matrices of different defects is the basis of some of the newer defect characterisation methods such as [68] and [69]. It can be seen from Figure 2.5 that the S-matrix of a hole has constant values along the diagonal lines, where $\theta_{sc} = \theta_{in} + C$ (C is a constant), which means a hole's S-matrix is only a function of the difference between the incident and scattering angles. Note that when C= ±180°, the two diagonal lines $\theta_{sc} = \theta_{in} \pm 180°$ indicate the forward scattering coefficients (i.e. the shadowing effect) of a defect. The S-matrix of a crack, however, shows a strong angular dependency to both incident and scattering angles and the high amplitude area in the pulse-echo component corresponds to the specular reflection.

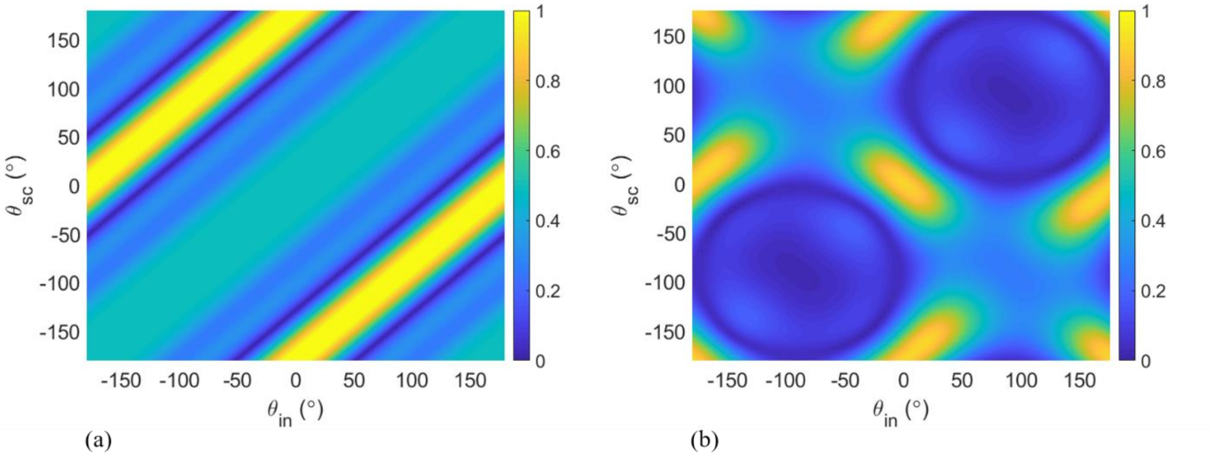

(a) (b)

Figure 2.5: Scattering matrices (amplitude) of (a) a 1λ side-drilled hole and (b) a 1λ crack.

2.4 Post Processing

2.4.1 Imaging Using Total Focusing Method

As discussed in section 2.2.1, one of the advantages of using FMC is the ability to apply any type of post-processing algorithm to the stored data set in order to produce an image or characterise a defect. One of the most powerful post-processing imaging algorithms is the total focusing method (TFM). Its imaging performance [73, 90] is considered to be the "gold standard" by many authors [91]. The method uses the FMC data to synthetically focus the ultrasound beam at every pixel within the 2D image in the x-z plane [73]. As shown in Figure 2.6, in order to produce an image, the TFM algorithm synthetically focuses on every pixel within the image such that if x is the direction along the array and z is the dimension into the test sample, the image intensity at every given coordinate, $I(x, z)$ is given by [92]:

$$I(x,z) = \left| \sum h_{i,j} \left(\frac{\sqrt{(x_i - x)^2 + z^2} + \sqrt{\left(x_j - x\right)^2 + z^2}}{c} \right) \right| \tag{2.6}$$

where $h_{i,j}(t)$ is the complex Hilbert transform of the time domain signal transmitted from element i and received by element j and c is the longitudinal velocity of sound in the test sample. This summation is applied to all possible transmitter-receiver pairs and as a result, uses the maximum amount of information available for each point in the x-z plane.

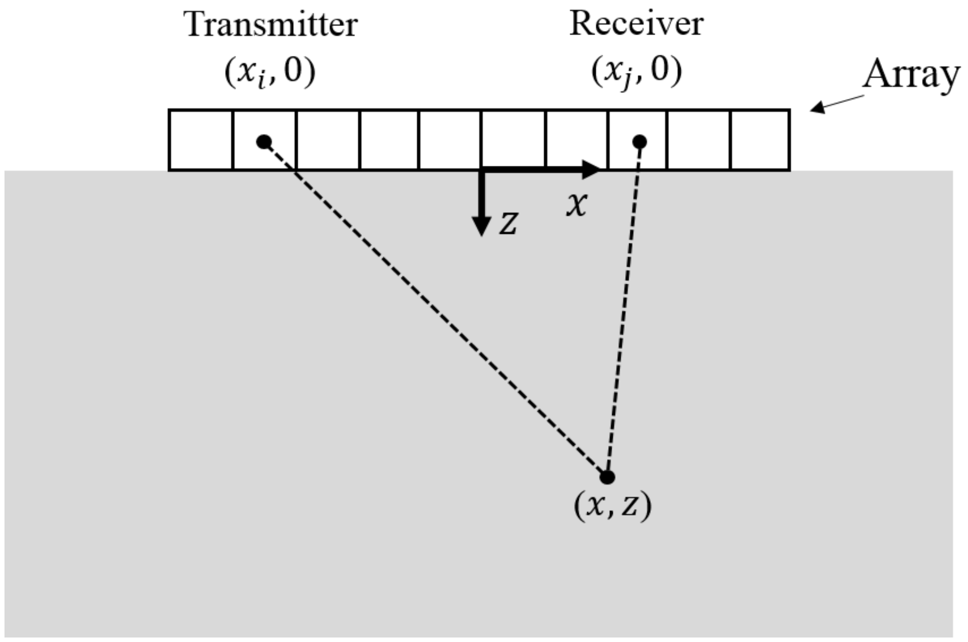

Figure 2.6: Schematic diagram showing geometry and notations used for TFM calculation in equation (2.6).

This approach is particularly useful for small point like reflectors and has out-performed other methods for this type of inspection [73]. Wilcox et al. [93] have further developed the TFM into the vector TFM (VTFM) algorithm. This allows the investigation of angular reflectivity characteristics of any point within the inspection volume, which provides valuable insight into the defect orientation and therefore assists with defect characterisation.

Although TFM can generate high resolution images, the geometry of small defects can be difficult or impossible to extract directly from the image. Frequency domain algorithms, such as the wave number algorithm ($\omega - k$ algorithm) [94] and back propagation method (BPM) [95] have shown to produce slightly better resolution than the time domain TFM [96]. However, frequency algorithms are more complicated to implement, and are not as flexible. There are other synthetically focused methods such as synthetic aperture focusing technique (SAFT) available [97, 98]. SAFT algorithm works by using the same element for both transmission and reception whilst moving along the surface of the test component. This is equivalent to a focused B-scan [99]. It was shown [73] that the TFM offers a better SNR and resolution compared to SAFT, which is due to the fact that in TFM the signals are averaged over all the array elements, which reduces the incoherent noise in the image. Despite being computationally intensive, the TFM is very flexible and further post-processing procedures can easily be added to the core algorithm [90, 100].

2.4.2 S-matrix Extraction

There have been different methods developed to extract the S-matrix from the FMC array data, such as the subarray approach [101] and inverse imaging approaches [95]. If there is only one isolated defect in a sample, S-matrix extraction is straightforward as equation (2.5) can be directly applied to the data from each transmit-receive element combination. However, typically, there are geometric features (or possibly other defects) that are close to the target defect and the FMC data is a superposition of the responses from all features. Therefore, extraction methods are required to obtain the S-matrix of a defect and reduce the effect of surrounding geometrical features, defects and noise [70]. The subarray method works by applying TFM imaging to subarray apertures and is given by [101]:

$$S_{sub}(\theta_k,\theta_l) = \frac{1}{{N_{sub}}^2}\sum_{i\in\alpha_k, j\in\alpha_l} S(\theta_i,\theta_j) \tag{2.7}$$

where N_{sub} is the number of elements in each subarray, α_k and α_l correspond to the k-th and l-th subarrays with the corresponding incident (θ_k) and scattering (θ_l) angles of the defect with respect to the subarray centre (see Figure 2.7). The scattering coefficient $S(\theta_i,\theta_j)$, is measured from the FMC data corresponding to the i-th transmitter element and the j-th receiver element. In order to calculate $S(\theta_i,\theta_j)$, for every pair of i-j elements, the arrival time of the signal from the transmitter element i (within the subarray k) to the target defect and back to the receiver element j (within the subarray l) is calculated and the corresponding values in the FMC are taken. Knowing the location of the point where S-matrix is being measured from (typically a maximum in the TFM image), every transmitting element then corresponds to an incident angle θ_i and likewise, every receiving element corresponds to a scattering angle θ_j.

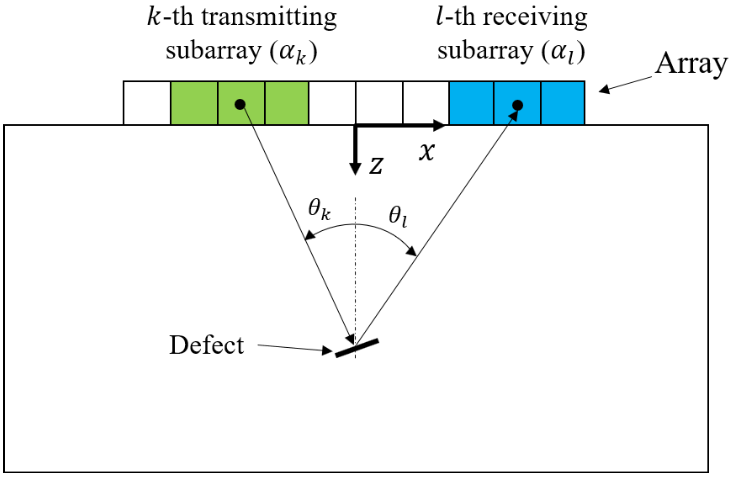

Figure 2.7: Schematic diagram of the subarray approach. Here, the number of elements in each subarray (N_{sub}) is 3.

The size of the subarray (i.e. the number of elements in each subarray) is a compromise between spatial resolution (i.e. a larger subarray leads to better focusing) and an angular blurring effect (i.e. a larger subarray averages the S-matrix over a wider range of angles). Hence, noise can be removed to some extent by averaging over the subarray elements, but the obtained S-matrix is a "smoothed" version [101]. This smoothing means that it is difficult to extract the phase of a S-matrix from the subarray method. In order to extract the phase of a defect's S-matrix, the inverse imaging approach can be used where a reversible forward imaging process is applied, and the scattering energy of the defect is distributed in the vicinity of the scatterer's location in the image [95]. Thus, by applying spatial filtering to the image, the scattering information of each defect can be obtained, and both the amplitude and phase of the defect's S-matrix can be measured.

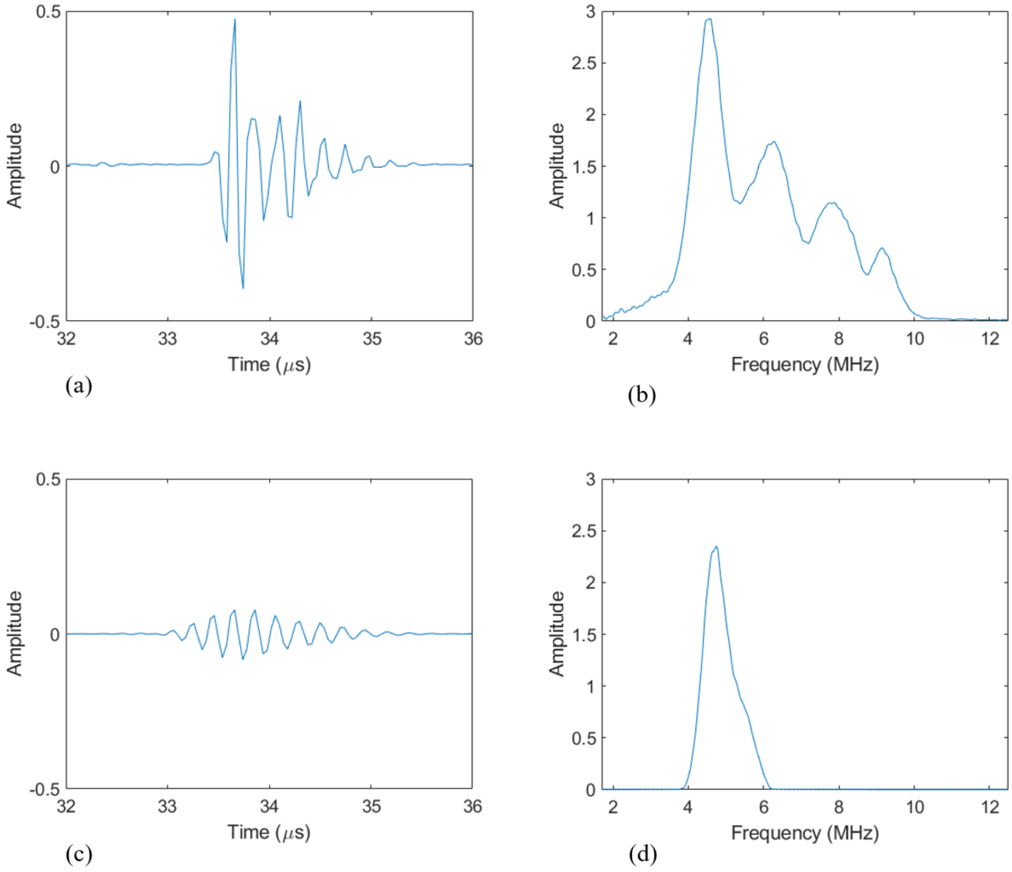

(a) (b) (c) (d)

Figure 2.8: Effect of Hanning band pass frequency filter (with 25% bandwidth at 5 MHz) on a pulse-echo signal received from the back-wall of a mild steel sample using a 5 MHz probe. (a) and (b) are unfiltered signals in time and frequency domains respectively. (c) and (d) are filtered signals in time and frequency domains respectively.

In this thesis, the subarray approach is used for S-matrix extraction, with each subarray consisting of 8 elements (i.e. 4λ, if array pitch is equal to half wavelength). Prior to this process, a de-noising Hanning band pass filter is also applied to the FMC data in frequency domain. Figure 2.8 shows an experimental pulse-echo signal captured by a 5 MHz transducer, in both time and frequency domains before and after applying the filter at 5 MHz with a 25% bandwidth.

2.4.3 Defect Characterisation

Defect characterisation is about finding the characteristics (typically size, shape and orientation) of defects, particularly crack-like defects, which are of the most important and challenging types. There have been a variety of methods introduced to characterise crack-like defects using ultrasonic arrays, such as image-based characterisation (for larger defects) [75] and characterisation by using the S-matrix (for smaller defects) [68, 70, 101]. These methods are discussed below.

2.4.3.1 Image Based Defect Characterisation

In case of a crack-like defect, the characterisation involves measuring the size and orientation angle from the array's captured data [102]. When the size of defect is relatively large, characterisation can directly be performed from the image. One method to achieve this is called the 6dB box fitting approach [75] where a rectangular box is fitted around the defect's image such that all pixels within the -6dB of the peak amplitude is covered. The size of the crack is then characterised as the length of the longer dimension of the fitted box and the orientation is estimated by measuring the orientation of the fitted box [102].

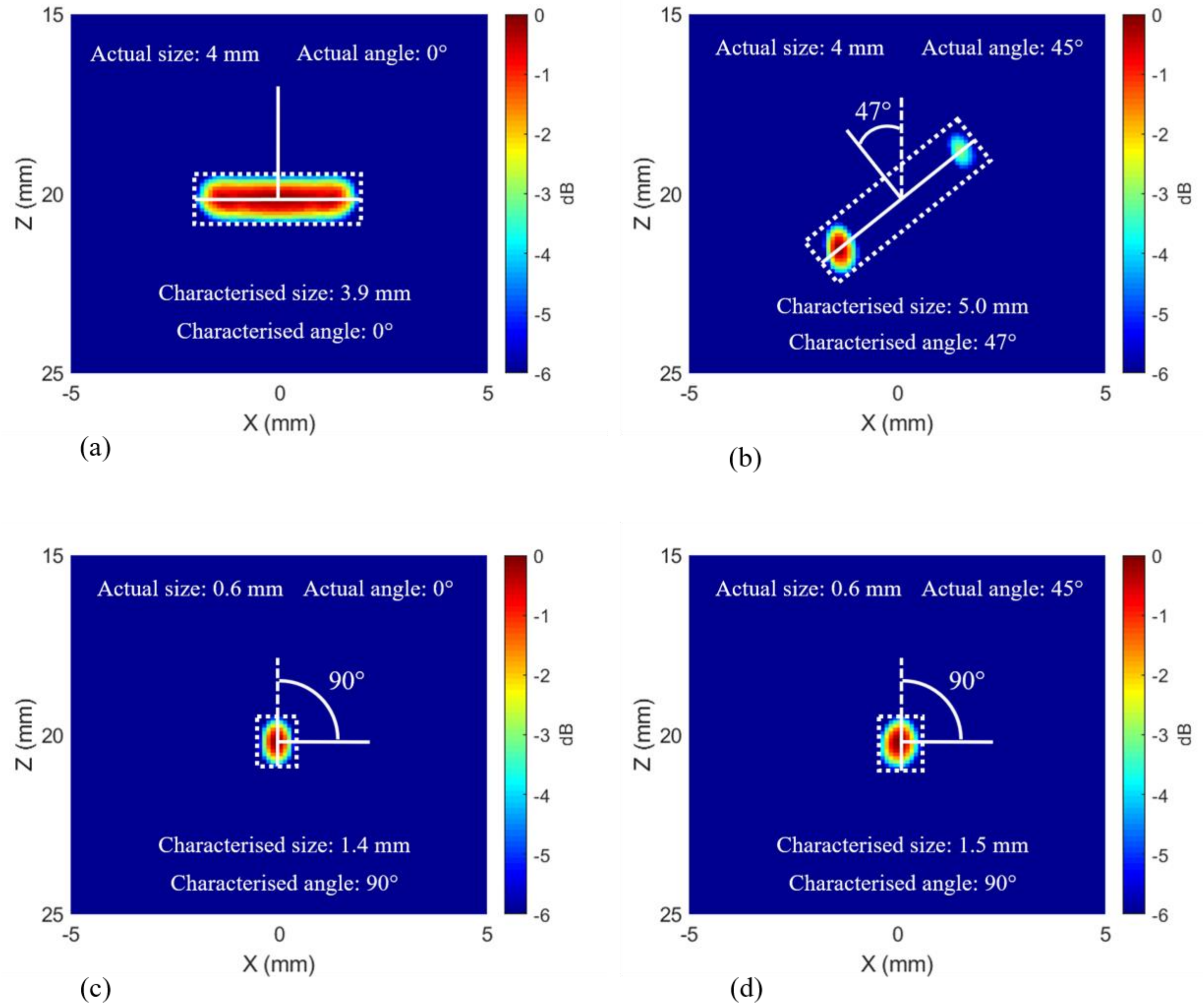

Figure 2.9: TFM image based characterisation of simulated cracks where the measurement configuration shown in Figure 2.4 is adopted. (a) is a 4 mm, 0° crack, (b) is a 4 mm, 45° crack, (c) is a 0.6 mm 0° crack and (d) is a 0.6 mm 45° crack. All cracks are simulated with an array of 64 elements, 5 MHz centre frequency (wavelength: 1.18 mm) and pitch of 0.5λ. Defects are simulated 20 mm directly below the centre of array. The white dotted boxes include (with minimum area) all the pixels within -6dB from the maximum TFM value in each plot.

Figure 2.9 (a) - (d) illustrates this method and the characterisation results from a range of crack-like defects: a 4 mm, 0° crack, a 4 mm, 45° crack, a 0.6 mm, 0° crack, and a 0.6 mm, 45° crack. All cracks are simulated for an array of 64 elements, 5 MHz centre frequency (wavelength: 1.18 mm) and pitch of 0.5λ. The cracks are simulated as being located 20 mm directly below the centre of array. From Figure 2.9, it can be seen that the image-based characterisation method is accurate for the 4 mm, 0° crack, where the size and orientation of crack are both measured with small errors. For the 4 mm, 45° crack, the orientation angle is correctly characterised from the TFM image, however, its size is overestimated by 25%. This error can be improved by taking the distance between the two peaks that result from the crack tips, which gives the size of 4 mm. For the two 0.6 mm cracks, the image-based characterisation approach fails as the orientation is incorrectly characterised as 90° and sizes measured to be 1.4 mm and 1.5 mm. This is consistent with the discussion in [75], which concludes that this characterisation method is only capable of sizing cracks larger than 0.6λ with orientation angles of less than 30° and when the noise level is low.

At AMEC Foster Wheeler (now Wood plc), an experimental study was carried out where TFM method was used to show the differences between different defects in a ferritic steel specimen including rough and smooth cracks, linear pores and porosity [103]. For porosity and linear pores, individual pores were clearly resolved in the images [103]. For the smooth crack, only the tips were detected in the TFM image, and for the rough crack, the TFM image was continuous due to the individual facets reflecting the ultrasonic waves [103].

In image-based characterisation methods, the image quality, such as resolution and signal-to-noise ratio are critical to the accuracy of measurements. The inverse wave field extrapolation (IWEX) method [74] uses a similar approach to the TFM, where the image amplitude at each grid point (pixel) is calculated, assuming a defect exists at each grid point. This method is based on the general Rayleigh II integral [74, 104] and is given as:

$$P(\overrightarrow{r_A}, \omega) = \int P(\vec{r}_0, \omega) \frac{\partial G}{\partial \vec{n}} dS \tag{2.8}$$

where $P(\overrightarrow{r_A}, \omega)$ is the spectrum of the pressure field at $\overrightarrow{r_A}$, $P(\vec{r}_0, \omega)$ is the measured spectrum of the wave field at $\vec{r}_0$ on S, G is the Green's function, and $\vec{n}$ is the normal to S (see Figure

2.10). In order to back-propagate the array data to the image domain (i.e. the sample area with the defects), the anti-causal Green's function [74] needs to be used in equation (2.8). Assuming the array measurement is taken in the far field of the defect, we have [74]:

$$P(\overrightarrow{r_A}, \omega) = \sqrt{\frac{jk}{2\pi}} z_A \int P(\vec{r}_0, \omega) \frac{1}{\sqrt{\Delta r} \Delta r} \times \exp(jk\Delta r)\, dx \tag{2.9}$$

where $\Delta r = |\overrightarrow{r_A} - \vec{r}_0|$ is the distance between the evaluation and observation points. The image amplitude of a point A in the image domain is calculated as the amplitude of the extrapolated wave field at the time when the transmitted wave reaches the point A.

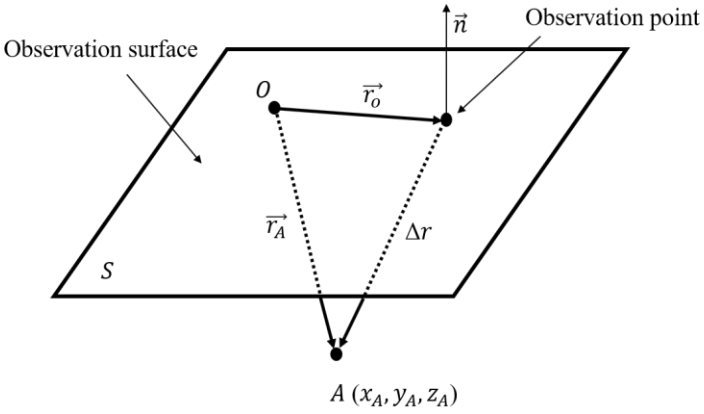

Figure 2.10: The Rayleigh II integral illustration. The wave pressure field at point *A* can be solved from the wave pressure field at observation surface *S*. Figure is reproduced from [74]**.**

Authors of [74] tested the imaging capability of the IWEX approach by applying it to a 1.5 mm side-drilled hole located 10 mm below an array of 64 elements with centre frequency of 4 MHz and pitch of 0.85 mm. The experiment was performed in a 20 mm-thick block of steel. They presented the results from different illumination paths of the side-drilled hole. It was shown that when using the L-L path to the hole, the front face of the side-drilled hole was reconstructed, and when using the back-wall reflected signals (the LL-LL path, i.e.

longitudinal-hole-back wall-hole-longitudinal), the back face (far side) of the hole was reconstructed successfully. The authors also tested other defects including a 2 mm notch. The method failed to image the notch when using the L-L path, as a result of the presence of a so-called "dead zone", however, when using the LL-LL path, the IWEX approach was able to clearly image the notch. From that image, the size of defect was accurately extracted but its orientation angle (45°) could not be measured.

When performing array inspections on a component with an irregular surface, it is difficult to carry out measurements in the direct contact mode. Therefore, other solutions are adopted, such as immersion testing where water is used as the couplant, or the use of a specially designed array shoe (also known as a wedge), which can be used in contact measurements [105]. When using these methods, the complex wave refraction at the interface of the two media must be taken into consideration. That means in order or apply an imaging algorithm which is based on delay laws, the incident point at the interface needs to be identified. In [105], the incident point was determined in an iterative search process based on the Fermat's minimum-propagation-time principle [106]. In an alternative to using full immersion, a fluid-filled flexible membrane device was designed in [107], which could be attached to an array and placed on a surface in order to measure the surface profile to a high accuracy [107].

The incident point can be calculated analytically given that the interface between the two media is planar [108]. For a given point of transmitter element (x_1,z_1) and a focal point (x_2,z_2) (points A and B in Figure 2.11), Snell's law gives the relationship [108]:

$$\frac{\beta(x_1 - x_0)^2}{(z_1 - z_0)^2 + (x_1 - x_0)^2} = \frac{(x_2 - x_0)^2}{(z_2 - z_0)^2 + (x_2 - x_0)^2} \tag{2.10}$$

where $\beta = (v_2/v_1)^2$. In [108], the use of Snell's law for non-planar interfaces was discussed and a numerical algorithm proposed. The authors also suggested that curve-fitting methods can be used to determine the geometry of interfaces in practical applications [108].

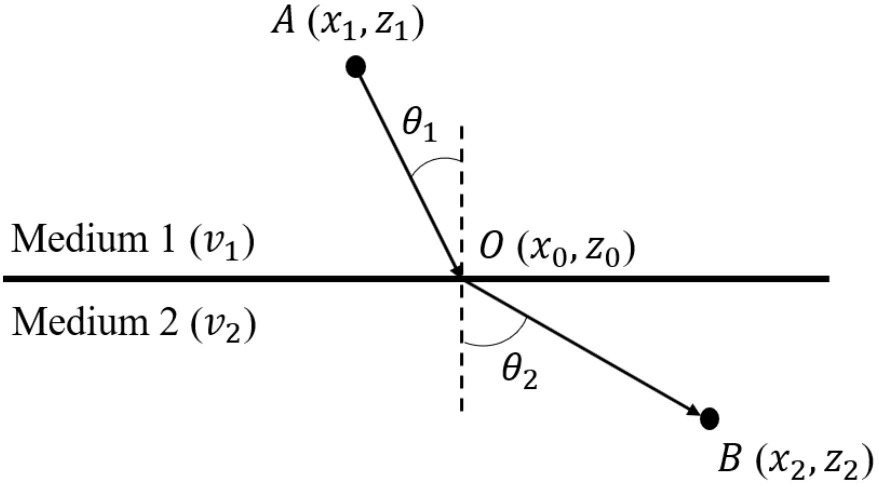

Figure 2.11: Wave refraction at a planar interface between two media of different sound velocities. Figure is reproduced from [108]**.**

2.4.3.2 Defect Characterisation Using the S-Matrix by Measuring the Half Width at Half Maximum (HWHM)

As the image-based characterisation methods struggle to measure properties of small crack-like defects, an alternative method was introduced which works by extracting the defect's S-matrix from experimental measurements [75]. When defects are smaller than 2λ, they are more distinguishable from their S-matrices than from their ultrasonic images. Figure 2.12 (a) and (b) show the S-matrices of the two 0.6 mm cracks with orientation angles of 0° and 45° whose TFM images were shown in Figure 2.9 (c) and (d). From Figure 2.12, it can be seen that the two defects have distinguishable S-matrices, whereas their TFM images look almost identical. Figure 2.12 (c) and (d) show the S-matrices of two 1.2 mm cracks with orientation angles of 0° and 45° respectively and it can be seen that both Figure 2.12 (a) and (b) are also distinguishable from Figure 2.12 (c) and (d). The angular range of the S-matrices in Figure 2.12 is from -60° to 60° for both the incident and scattering angles, but in a real experimental measurement, this angular range is determined by the array-defect configuration.

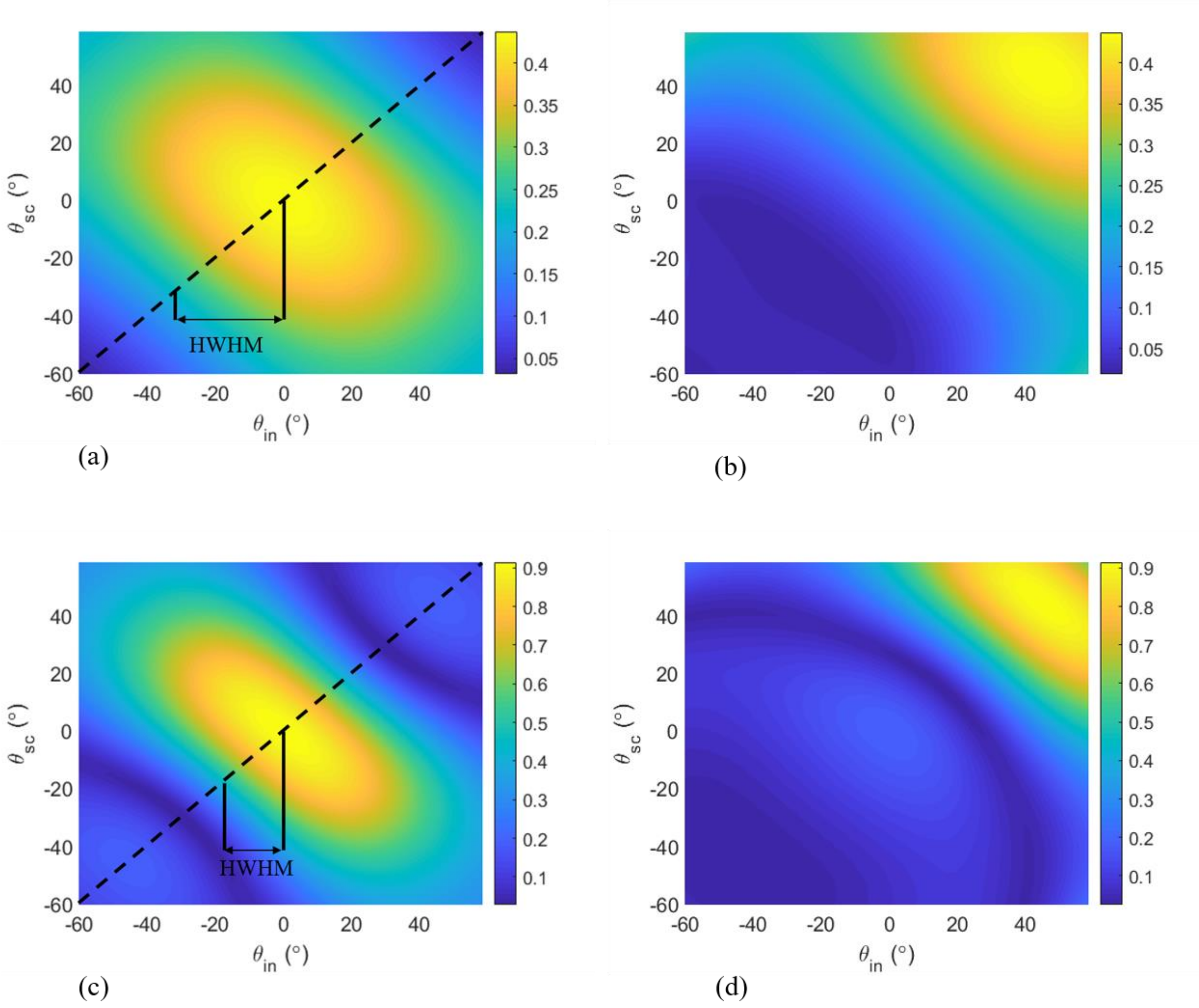

(a) (b)

(c) (d)

Figure 2.12: S-matrices of (a) a 0.6 mm, 0° crack, (b) a 0.6 mm, 45° crack, (c) a 1.2 mm, 0° crack and (d) a 1.2 mm, 45° crack.

In [75], the half width at half maximum (HWHM) of a S-matrix is defined as the angular region within which the pulse-echo amplitude drops by 6dB (i.e. 1/2) from its peak amplitude as shown in Figure 2.12 (a) and (c). This angular range decreases monotonically as the crack size increases [75]. The highest rate of HWHM change is from 0.25λ - 2λ. As the size of crack increases to more than 2λ, the sensitivity of this method for sizing cracks decreases [75]. For a crack whose specular reflection from the crack face is measurable, its size can be characterised by measuring the HWHM as is shown in Figure 2.13 (a). The orientation angle of a crack can also be determined as the angle where the maximum amplitude in pulse-echo signal occurs [75]. In Figure 2.13 (a), the HWHM is measured and the size of crack is characterised as 0.6 mm and orientation is measured as 45°, which are the actual size and orientation of the simulated crack. If the specular reflection cannot be measured, or if the maximum amplitude in pulse-echo signal is not the global maximum, the HWHM method fails even in a noise free medium. Figure 2.13 (b) shows that in case of a 1.2 mm, 85° simulated crack, the HWHM method characterises the crack as 1.07 mm and 40° which has a large angle error.

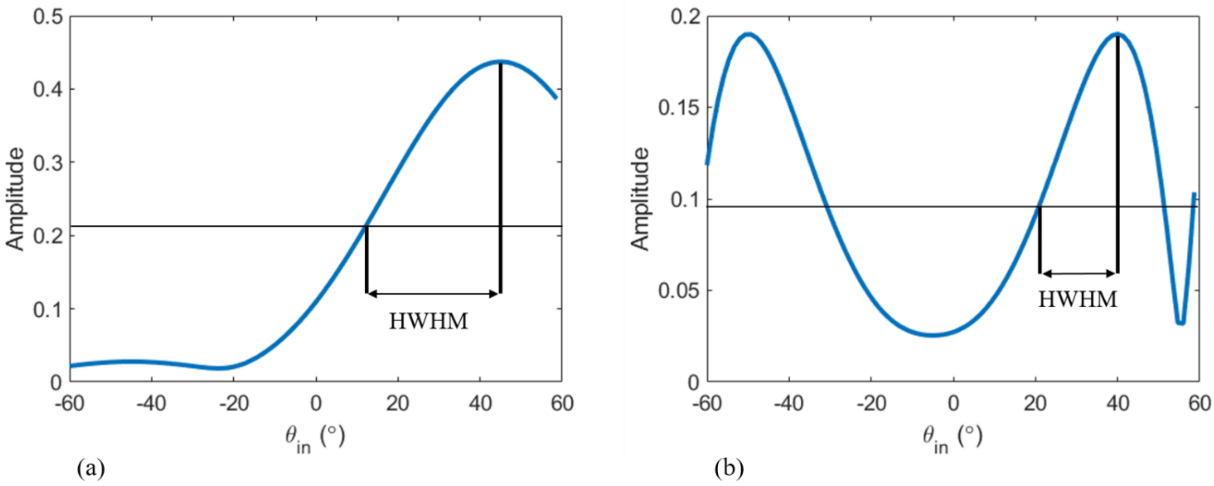

Figure 2.13: Characterisation of (a) a 0.6 mm, 45° crack and (b) a 1.2 mm 85° crack, by measuring the half width at half maximum (HWHM) of the pulse-echo signal.

2.4.3.3 Characterisation of Crack-Like Defects Using Similarity Metrics

In this method, experimentally measured S-matrices (from the subarray method [101]) are compared to a database of analytically simulated S-matrices [56] from a set of reference defects. Prior to the measurement, the database of S-matrices is created for a range of different crack-like defects (in this thesis, sizes varying from 0.1 mm to 3.0 mm with an increment of 0.1 mm and orientation angles ranging from -85° to 90° with an increment of 5° are used). The method of comparison is correlation coefficient (also known as Pearson correlation coefficient) [109], which is a suitable similarity metric for this purpose, as it compares the shapes of S-matrices regardless of their average amplitudes. Correlation coefficient (CC) between the measured S-matrix (S_m) and each analytical S-matrix in the database which is created in the centre frequency (S_a) is given by [68]:

$$\rho = \frac{\sum_{i=1}^{M}\sum_{j=1}^{M}(S_m(i,j) - \bar{S}_m)(S_a(i,j) - \bar{S}_a)}{\sqrt{\left(\sum_{i=1}^{M}\sum_{j=1}^{M}(S_m(i,j) - \bar{S}_m)^2\right)\left(\sum_{i=1}^{M}\sum_{j=1}^{M}(S_a(i,j) - \bar{S}_a)^2\right)}} \qquad (2.11)$$

where S_m is the measured S-matrix, S_a is the analytical database S-matrix, M is the total number of corresponding incident/scattering angles (i.e. number of subarrays as shown in Figure 2.7), S_m and S_a are of size $M \times M$, and $\bar{S}_m$ and $\bar{S}_a$ are the mean values of the matrices S_m and S_a respectively.

The CC can be between -1 and 1, and a higher value corresponds to a better match between the two S-matrices. Since CC is an intensity-based similarity metric [110], it does not rely on any specific features (e.g. the HWHM) of the S-matrix and therefore, it effectively combines the feature detection and matching steps [111]. Furthermore, it is thought to be the optimal method of comparison between two images when the relationship between the signal intensities is linear [112].

The size and orientation of the unknown crack is characterised as the defect in the database with which it has the highest similarity (i.e. the highest CC). The highest similarity or the best match is determined by obtaining the CC between the measured S-matrix from experimental data and each of reference cracks in the simulated database. Therefore, the CC values form a correlation map as shown in Figure 2.14, which shows the correlation map of a crack (0.6 mm, 45°) simulated 20 mm below an array with 64 elements and centre frequency of 5 MHz and pitch of 0.6 mm. The HWHM characterisation failed to measure the properties of this crack. However, the similarity metric method is capable of correctly characterising the defect as the peak in Figure 2.14 (indicated by the arrow) corresponds to the correct size and orientation angle in the database. From Figure 2.14, it can be seen that the changes in CC are faster in the orientation angle direction than in the size direction, suggesting that it is easier to extract angle than size in this case.

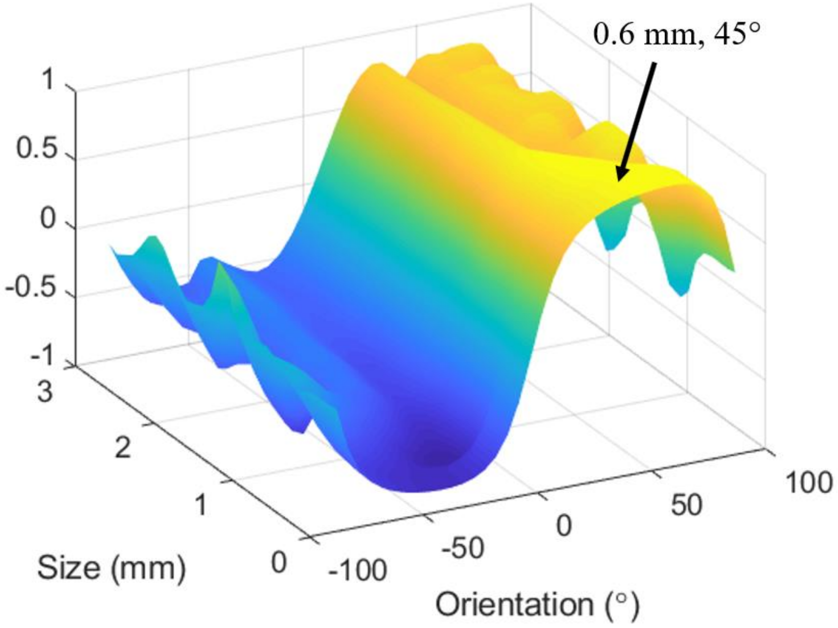

Figure 2.14: Correlation coefficient map of a 0.6 mm, 45 crack, simulated 20 mm below an array with 64 elements and centre frequency of 5 MHz and pitch of 0.6 mm.

This characterisation method (termed the *database similarity metric method* hereafter) is used extensively in this thesis where the following steps are followed:

0. Prior to the measurement, create a database of analytically modelled S-matrices [56] for a range of different crack-like defects (in this thesis we use sizes varying from 0.1 mm to 3.0 mm with an increment of 0.1 mm and orientation angles ranging from -85° to 90° with an increment of 5°).
1. TFM image is produced of the experimental defect.
2. Select a rectangular region (box) around the detected defect on the TFM image to include the defect's peak TFM amplitude.
3. Identify the location (x and z) of the maximum TFM amplitude within the selected box.
4. Extract the S-matrix from the identified defect location using the procedure explained in Section 2.4.2, i.e. the subarray method [101].
5. Compare the S-matrix from step 4 to all S-matrices in the database created in step 0 using correlation coefficient (CC). This gives a CC value for every defect in the database (i.e. CC map).
6. Characterise defect as the crack-like defect in database, with which the measured S-matrix has the maximum CC.

2.5 Conclusion

In this Chapter, ultrasonic phased arrays are reviewed, and their capabilities and applications are discussed. Phased array transducers are able to generate wave fields similar to the ones created from multiple single element probes, and elements can either be fired in-phase or different delay laws can be used in order to steer or focus the beam. The concept of FMC was also explained, which is a matrix of data containing the time domain signals (A-Scans) transmitted and received by every pair of elements. Furthermore, the concept of the S-matrix was discussed, which contains the angular scattering information of the defect. It was further shown that FMC data can be used for post-processing to generate images, extract the S-matrix and characterise defects. Some common imaging techniques including the TFM and IWEX methods were presented and their applications in defect characterisation were reviewed. It was shown that relatively large defects can be characterised directly from their images (e.g. by adopting the 6dB box-fitting approach). However, in case of smaller defects, their images become indistinguishable from each other, and other approaches which take advantage of S-matrices are more effective.

Chapter 3

Hybrid Forward Model

3.1 Introduction

In this Chapter, a forward hybrid model used for the simulation of crack FMC data set as well as noise simulation are described. Throughout the thesis, this model is used extensively in order to simulate the FMC of a range of crack-like defects with varying noise levels and different array configurations. In this Chapter, first, the overall ray model is introduced and then the simulation of each term of the model, such as the input signal, beam spreading, directivity function and crack scattering coefficient matrix are explained in more detail. In this model, the scattered field of the crack is calculated by measuring the crack opening displacements (assuming traction-free boundary conditions at crack sides), and adopting the integral representation of the scattered wave field. The two key characteristics of cracks in this model are size and orientation angle. The noise model works by simulating multiple point scatterers around the defect, which correspond to grains in a polycrystalline metal. Finally, the model is verified by comparing the S-matrices of simulated crack-like defects with experimental measurements.

3.2 Simulation of Array Data

Throughout this thesis, a semi-analytical hybrid forward model based on an algorithm developed by Glushkov et al. [56] is extensively used in order to simulate the full matrix capture (FMC) corresponding to all the transmit-receive signals when an array is placed above a defect as shown in Figure 3.1 (a). The model assumes a two-dimensional (2D) geometry and planar crack-like defects of negligible width, with two key characteristics of size, l, and orientation angle, α, as shown in Figure 3.1 (b). The orientation angle of the crack-like defect refers to the anti-clockwise angle from the horizontal and can vary from $-{}^{\pi}/_{2}$ to ${}^{\pi}/_{2}$. Figure 3.1 (a) also shows the wave path from an array transmitter element to the defect and its return path back to a receiver element. Assuming the defect is in the far field of the array elements and the array elements are in the far field of the defect, the received defect signal in the frequency-domain, transmitted from the element T_x and received by the element R_x can be expressed as [90]:

$$F_d(T_x, R_x, \omega) = F_0(\omega)\,\frac{\sqrt{\lambda}}{\sqrt{R_T R_R}}\,D(\varphi_T, \omega)\,D(\varphi_R, \omega)\,S_d(\theta_{in}, \theta_{sc}, \omega, l)\exp(-i\omega\tau_{TR}) \qquad (3.1)$$

where F_0 is the frequency spectrum of the signal transmitted into the test sample (which is generated by exciting a piezo-element with an electrical input), λ is the wavelength, R_T and R_R are the distances from the defect to the transmitting and receiving elements respectively, D is the element directivity function [46, 113] (which is a radiation pattern describing the relative angular distribution of the field pressure when radiating into the medium), S_d is the defect S-matrix, θ_{in} and θ_{sc} are incident and scattering angles to and from the crack-like defect and τ_{TR} is the traveling time of the signal from transmitter to the defect centre and back to the receiver. The model is termed hybrid as the S-matrix is calculated by a 2D semi-analytical boundary integral method developed in [56] where the crack opening displacements are calculated based on traction-free boundary conditions at crack sides and the integral representation of the scattered wave field [57] is adopted to calculate the scattered field of the crack. Note that equation (3.1) is a general model and hence true for any wave mode and mode conversions, however, in this thesis only the longitudinal wave components (i.e. L-L scattering) are used.

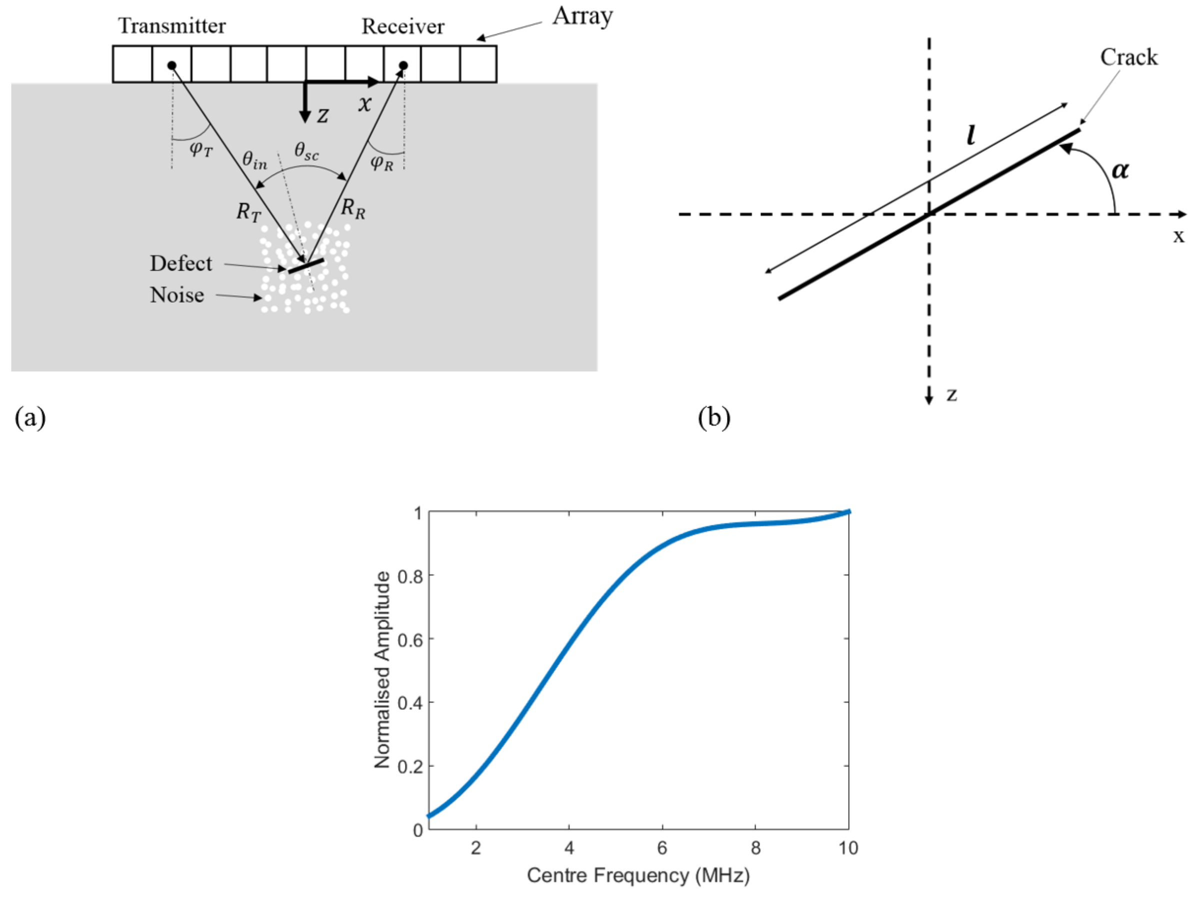

(a) (b)

(c)

Figure 3.1: Schematic diagram of (a) geometry and notations used in equations (3.1) and (3.3) and (b) geometry of crack orientation angles. (c) Shows the normalised point scatterer's S-matrix used in equation (3.3) as a function of centre frequency.

The model is run at many different frequencies in order to cover the frequency spectrum of the input signal that are generated by a piezo-element. A discrete inverse Fourier transform function (iƑ) is then applied to the result of equation (3.1) to obtain the time-domain signal

$f_d(T_x, R_x, t)$. When the third dimension of both $f_d(T_x, R_x, t)$ and $F_d(T_x, R_x, \omega)$ are sequences of n complex numbers, iF is defined as [114]:

$$
\begin{aligned}
f_d(T_x, R_x, j \in n) &= \mathrm{iF}\big(F_d(T_x, R_x, k \in n)\big) \\
&= \frac{1}{n}\sum_{k=1}^{n} F_d(T_x, R_x, k)\exp\left(\frac{i2\pi(j-1)(k-1)}{n}\right)
\end{aligned} \tag{3.2}
$$

This gives a simulated FMC array data set for a given defect at a given location. Figure 3.2 shows a TFM image of a 2 mm, 30° crack-like defect simulated at (x = 0, z = 30 mm) and (x = 20 mm, z = 30 mm) in a block of mild steel, using a 64-element array with centre frequency of 5 MHz and pitch of 0.63 mm. The model is fast and the FMC data set required for the case in Figure 3.2 was computed in 2s on a standard desktop PC.

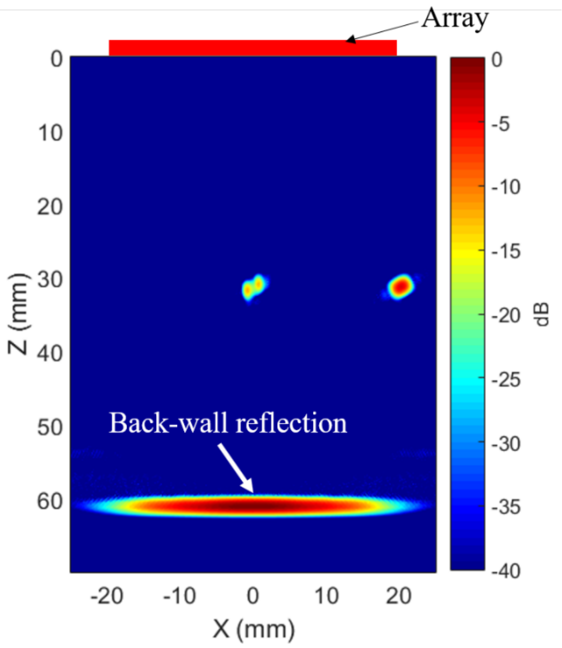

Figure 3.2: TFM image of a simulated crack (l = 2 mm, α = 30°) in a mild steel block using a 64-element array with centre frequency of 5 MHz and element pitch of 0.63 mm.

3.3 Noise Simulation

In order to consider the effect of material noise, a noise model based on [115] is developed where multiple point scatterers, corresponding to grains in a polycrystalline metal, are simulated around the defect. This model assumes an omni-directional scattering for each grain, regardless of incident angle and that there is no spatial correlation between material scattering from different positions [115]. The number of point-scatterers (N) needs to be large enough to satisfy a requirement of a minimum 5 scatterers per wavelength squared [116]. The point-scatterers have been modelled within a square of 10 mm centred to the defect as shown in Figure 3.1 (a) and any grain noise outside this region is considered to have negligible effect on the defect. The received noise signal in the frequency-domain, transmitted from the element T_x and received by the element R_x can be expressed as [90]:

$$F_n(T_x, R_x, \omega) = \sum_{p=1}^{N} F_0(\omega)\, \frac{\sqrt{\lambda}}{\sqrt{\mathrm{R}_T^p \mathrm{R}_R^p}}\, D(\varphi_T^p, \omega)\, D(\varphi_R^p, \omega)\, S_n(\omega) \exp(-i\omega\tau_{TR}^p) \tag{3.3}$$

where N is the number of point scatterers, F_0 is the frequency spectrum of the signal transmitted into the test sample, λ is the wavelength, R_T^p and R_R^p are the distances from each point scatterer to the transmitting and receiving elements respectively, D is the element directivity function [46, 113], S_n is the point (or grain) scatterer's scattering coefficient (illustrated in Figure 3.1 (c)) and τ_{TR}^p is the traveling time of the signal from transmitter to each point scatterer and back to the receiver. This scattering model has been used to model grains in [117] and [118] as well. Figure 3.1 (c) shows the omni-directional scattering amplitude, S_n, as a function of frequency, which is derived from the pulse-echo signal capturing the specular reflection from the centre of a simulated 0.01 mm crack.

This linear systems model was used to simulate material noise quickly for any arbitrary array design, for which a FMC data set (f_n) can be generated and added to the FMC of simulated defect (f_d) in time-domain as:

$$f_c(T_x, R_x, t) = f_d(T_x, R_x, t) + Af_n(T_x, R_x, t) \tag{3.4}$$

where f_c is the total combined FMC in time domain, f_d is the FMC calculated using equation (3.1), A is the amplification factor or noise level and f_n is the noise FMC calculated in equation (3.3). Note that $A = 1$ corresponds to a low noise Aluminium Alloy and $A = 10$ corresponds to a moderate-noise mild steel (EN24). This comparison is from measuring the root mean square of the TFM image of the simulated noise (normalised to a simulated back-wall as a reference) and comparing it with that of experimentally measured grain noise from defect-free samples.

3.4 Pulse Generation

The hybrid model is built entirely in MATLAB and the main calculations are in the frequency domain. For all FMC simulations in this thesis, the array input signal in time-domain is a five-cycle tone burst centred at zero time ($f_0(t)$), which is obtained by multiplying a carrier sin (ωt) by a Hanning window H (t). A five-cycle input pulse is typical in standard phased arrays used in this thesis. In order to use this input signal in the hybrid model, the frequency spectrum of the array input signal, $F_0(\omega)$ is calculated using the discrete Fourier Transform function Ƒ. When both $F_0(\omega)$ and $f_0(t)$ are sequences of n complex numbers, Ƒ is defined as [114]:

$$F_0(k \in n) = \digamma(f_0(j \in n)) = \sum_{j=1}^{n} f_0(j) \exp\left(\frac{-i2\pi(j-1)(k-1)}{n}\right) \tag{3.5}$$

Figure 3.3 (a) and (b) show the time-domain input signal and its corresponding frequency-domain spectrum respectively, for a centre frequency of 5 MHz. Throughout this thesis, a 5-cycle duration pulse is used.

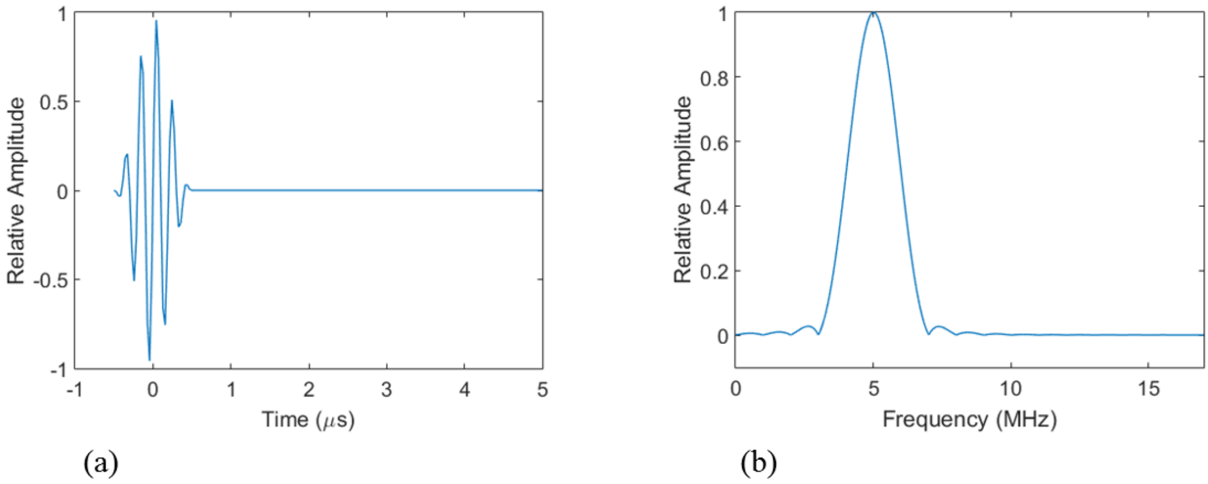

Figure 3.3: (a) Time-domain array input signal with 5 MHz centre frequency. (b) Frequency-domain spectrum of the signal in (a).

3.5 Beam Spread

As the ultrasonic wave propagates in the medium, the acoustic energy will spread out meaning that the receiver R_x receives an amplitude lower than that at the transmitter T_x. Given the assumption that the defect is in the far field of a relatively long and narrow transducer, in a 2D setup, the wave-front is cylindrically spreading (from the line source). Therefore, as the wave travels through the material, the energy is spread out over the cylindrical surface area $2\pi rL$, where r is the radius and L is the height of the cylinder (i.e. the length of the element in the y-dimension as seen in Figure 3.4). This spreading of a fixed amount of energy over an increasing area is called cylindrical spreading loss [119] and at distance r from the transducer, leads to a decay in pressure at the rate of $1/\sqrt{r}$ in a 2D setup (or $1/r$ in a 3D setup). Therefore, considering a wave travelling (in 2D) from the transmitter to the defect and back to the receiver, the beam spreading effect (pressure decay rate) is written as $1/\sqrt{R_T R_R}$.

3.6 Directivity Function

Each array element produces a radiation pattern which describes the angular dependence of the field pressure distribution, both when propagating into the medium and when receiving the reflected signal. In this section, the parameters for modelling this angular dependency of a rectangular array element as shown in Figure 3.4 are explained.

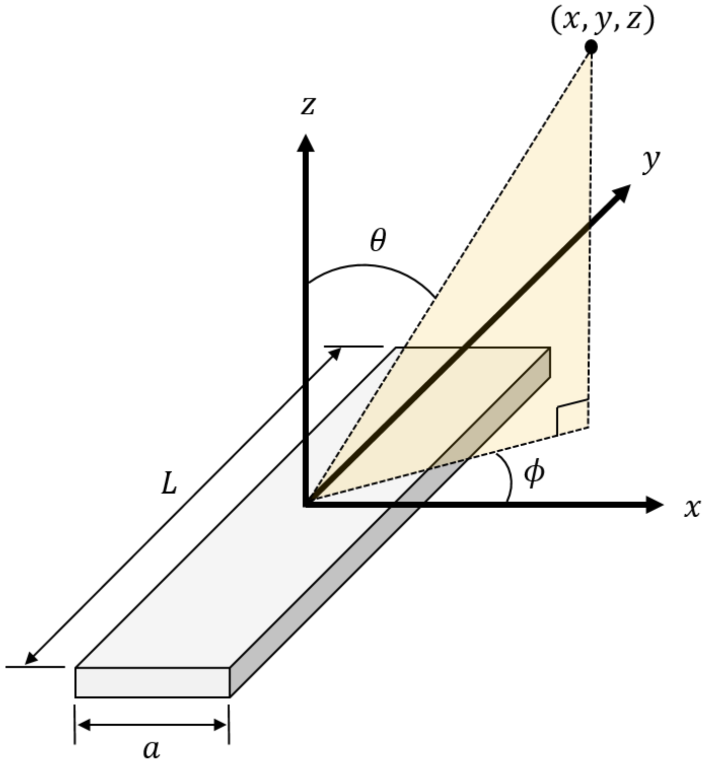

Figure 3.4: Schematic diagram of an array element, showing the parameters used for modelling the directivity.

The area below a radiating transmitter consists of a near field region (Fresnel zone) and a far field region (Fraunhofer zone). The distance between the transducer and the beginning of far field region is called the Rayleigh distance D^R [120]. After this distance, the field spreads spherically or circularly, similar to that of a point source in a 3D setup or line source in a 2D configuration. For a given wavelength, D^R in the x-z plane is calculated by [120]:

$$D^R = \frac{2a^2}{\lambda} \tag{3.6}$$

where a is the width of element and λ is the wavelength in the medium. In a typical case where longitudinal velocity is 6000 m/s, frequency is 5 MHz, and element width is λ/2, D^R = λ/2 = 0.6 mm. Throughout this thesis, it is assumed that the width of array elements are small enough to be characterised only by their far field.

In the far field, 3D pressure distribution from a rectangular element into a fluid can be modelled using the directivity function given in [121]:

$$D_f(\omega, \theta, \phi) = \operatorname{sinc}\left(\frac{\pi a \sin\theta \cos\phi}{\lambda(\omega)}\right) \operatorname{sinc}\left(\frac{\pi L \sin\theta \sin\phi}{\lambda(\omega)}\right) \tag{3.7}$$

where D_f is the directivity function in a fluid, θ and ϕ are the elevation and the azimuth angles respectively, as shown in Figure 3.4.

In this thesis a 2D model is used to describe the wave propagation from a 1D array into the x-z plane and the elements are assumed to behave as infinitely long strips (in y direction). In this 2D model, the azimuthal angle ϕ = 0, and therefore, equation (3.7) can be simplified and written as:

$$D_f(\omega, \theta) = \operatorname{sinc}\left(\frac{\pi a \sin\theta}{\lambda(\omega)}\right) \tag{3.8}$$

Equations (3.7) and (3.8) are valid for arrays radiating into fluid. However, in the case of isotropic solids, the pressure field generated by each array element are modelled using the method in [113]. In the 2D case, where an array is coupled to the surface of a semi-infinite elastic solid, the directivities, D_L and D_S, of longitudinal and shear waves in the far field are given by [113]:

$$D_L(\theta) = \frac{\left(\left({}^{c_L}/_{c_S}\right)^2 - 2\sin^2\theta\right)\cos\theta}{F_0(\sin\theta)} \tag{3.9}$$

$$D_S(\theta) = \left(\frac{c_L}{c_S}\right)^{5/2} \frac{\left(\left({}^{c_L}/_{c_S}\right)^2 \sin^2\theta - 1\right)^{1/2} \sin 2\theta}{F_0(k\sin\theta)} \tag{3.10}$$

where c_L and c_S are the bulk longitudinal and shear wave velocities and:

$$F_0(\xi) = \left(2\xi^2 - \left(\frac{c_L}{c_S}\right)^2\right)^2 - 4\xi^2(\xi^2 - 1)^{1/2}\left(\xi^2 - \left(\frac{c_L}{c_S}\right)^2\right)^{1/2} \tag{3.11}$$

The far field directivity of an array element on the surface of a semi-infinite solid can then be written as:

$$D(\omega,\theta) = D_f(\omega,\theta)\,.\,D_{L,S}(\theta) \tag{3.12}$$

Throughout this thesis, only the longitudinal mode is used. Figure 3.5 illustrates the effect of the terms in equation (3.12), where c_L/c_S = 2 and the amplitudes are normalised by $D_L(0)$. Figure 3.5 (a) and (b) show the directivity patterns of longitudinal wave radiated into fluid by an element of λ/2 width and 2λ width respectively. Figure 3.5 (c) shows the directivity due to line loading of a solid half-space and Figure 3.5 (d) and (e) demonstrate the effect of both the element width (λ/2 and 2λ respectively) and the half-space loading combined. It can be seen that for a larger element width, a greater directionality and side lobes are observed.

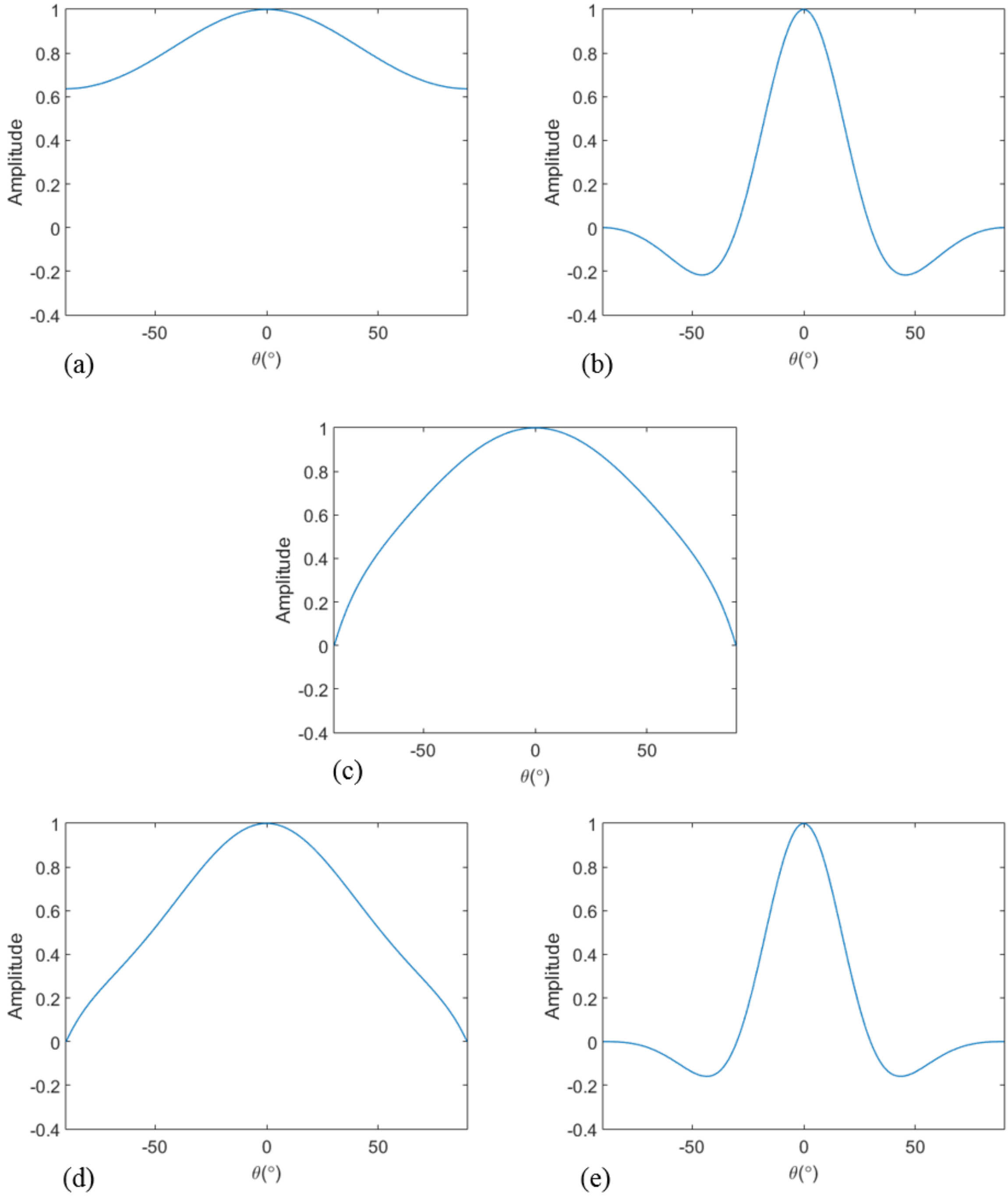

Figure 3.5: Comparison of array element directivity functions: (a) λ/2 width element radiating into fluid, (b) 2λ width element radiating into fluid, (c) longitudinal wave amplitude due to line loading of a solid half-space, (d) λ/2 width element radiating into solid half-space, and (e) 2λ width element radiating into solid half-space. In all cases c_L/c_S = 2 for the solid. All waves are normalised to $D_L(0)$.

3.7 Crack Scattering Coefficient Matrix

In this thesis, the crack S-matrices are simulated by a 2D fast semi-analytical model developed in [56], which is based on a boundary integral equation method. Although this model inherently includes all modes, only the longitudinal-longitudinal (L-L) S-matrix output is considered. In this model, first the opening displacements of cracks are numerically calculated and then an exact integral representation of the scattered wave field [57] is used to model the S-matrix.

In order to speed up the FMC simulation process, a large database of S-matrices was generated in MATLAB (as a 4D matrix file), which contains a range of values of frequencies (from 0 to 18 MHz with increments of 0.05 MHz), crack sizes (from 0.1 mm to 3 mm with increments of 0.1 mm) and incident and scattering angles (from -180º to 180º with increments of 4º). This database was then used with linear interpolation for all the future crack simulations, which significantly reduced the computation time.

Figure 3.6 shows a comparison between the simulation and experimental results for S-matrices of two cracks (defects A and B in Table 3.1). In Figure 3.6 (a) and (b), S-matrices are simulated in a noise-free medium and in Figure 3.6 (c) and (d), the S-matrices are extracted (using the subarray approach described in section 2.4.2 of Chapter 2) from two real cracks (EDM notches cut with a 0.1 mm thick wire) at depth 50 mm (i.e. $x = 0$, $z = 50$ mm) in a low noise mild steel. Figure 3.7 shows the experimental setup and a schematic diagram of the defects. By comparing Figure 3.6 (a) and (b) with Figure 3.6 (c) and (d), an excellent agreement between the experimental and simulated results are shown. Using equation (2.11) in Chapter 2, the correlation coefficient (CC) between simulated and experimental S-matrices are calculated to be 0.9889 and 0.9965 for cracks A and B respectively. This model is also validated in Chapters 4 and 5 by other methods.

Table 3.1: Details of cracks used in the experiment.

Defect	Length (mm)	Orientation angle (°)
A	1	0
B	1	30

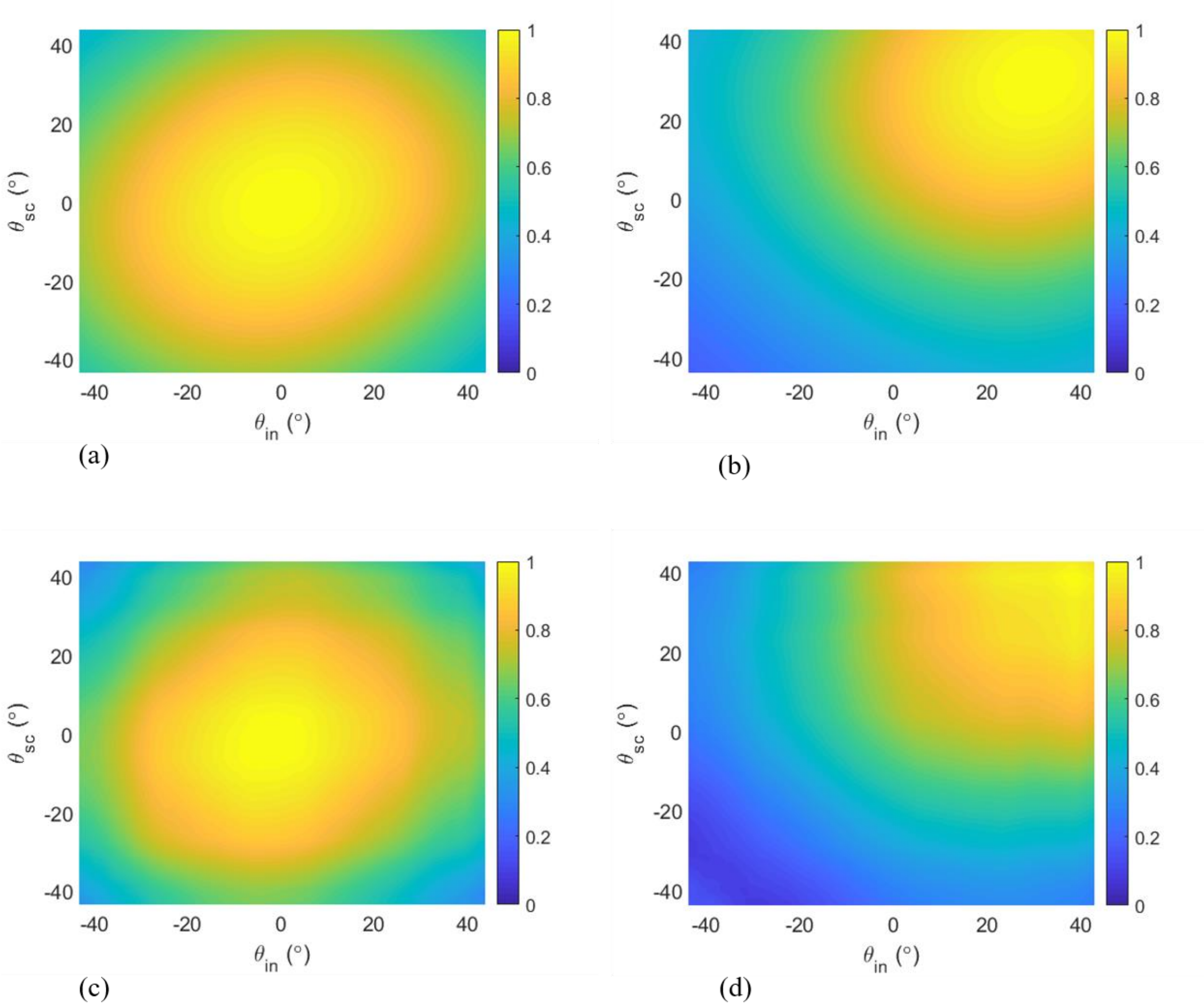

(a)

(b)

(c)

(d)

Figure 3.6: Comparison of simulated and experimentally measured S-matrices for a crack simulated at 50 mm directly below a 64-element array with pitch of 1.57 mm (0.5λ) and centre frequency of 2 MHz. (a) simulated and (c) experimentally measured S-matrices of a 1 mm, 0° crack. (b) simulated and (d) experimentally measured S-matrices of a 1 mm, 30° crack. The CC between (a) and (c) is 0.9889 and the CC between (b) and (d) is 0.9965.

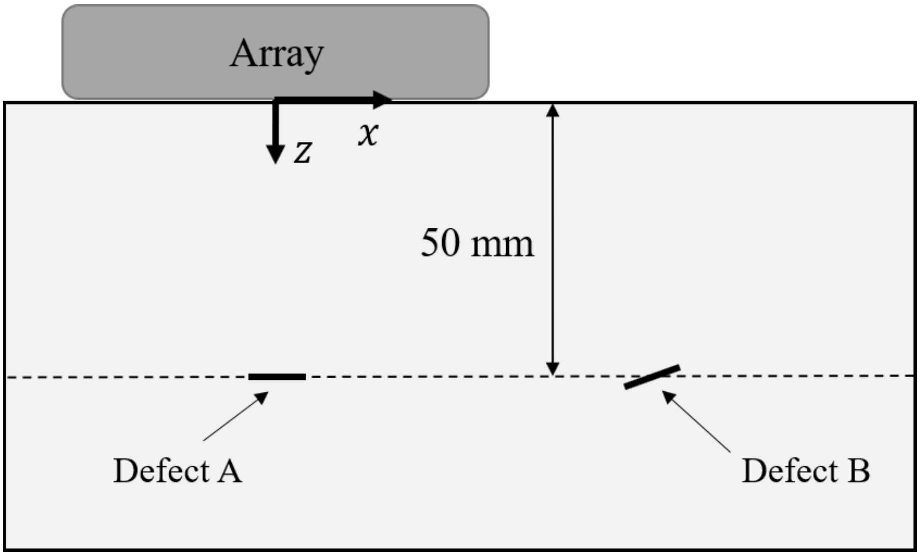

Figure 3.7: Schematic diagram of the experimental setup and defects (EDM notches).

3.8 Conclusion

In this Chapter, the main forward model that is used for simulation of array FMC data set is defined and the noise model used to replicate material grain noise is discussed. It was shown how the input signal is generated in time-domain and the concepts of array element directivity function and beam spreading are explored. A 2D fast semi-analytical model, which is used to simulate the S-matrix of planar cracks was explained. The algorithm works by measuring the crack opening displacements in traction-free boundary conditions at crack sides and the integral representation of the scattered field is used. In the noise model, multiple point scatterers are simulated around the defect, which correspond to material grains. Finally, the model was validated by comparing the S-matrices of simulated cracks with those measured in experiments on a mild steel sample with EDM notches. The average correlation coefficient between simulated and experimentally measured S-matrices was calculated to be 0.9927, which shows a great agreement between the experimental and simulated results.

Chapter 4

Assessment Methodology for Defect Characterisation Methods

4.1 Introduction

This Chapter is based on a journal article published in “NDT & E International” in 2018 [122], where I was the main author and all other co-authors had a supervisory role.

There have been variety of methods introduced to characterise defects using ultrasonic arrays (se refs [68–70, 75, 76]). However, the robustness of these techniques is not fully known, especially with regards to the location of defects relative to arrays, and there is no agreed methodology for assessing their performance. Instead, these methods are typically assessed by simply applying them to a few specific defects located at specific positions and it is assumed that the performance is similar for other defects at other locations [68, 70, 123]. For example, the authors of the *database similarity metric method* [68], assessed its performance by characterising cracks only at depth 20 mm below the centre of array.

In this Chapter a spatial assessment method is introduced to map the performance of ultrasonic array based characterisation algorithms against the key variables that affect their accuracy, such as the location, size and orientation angle of crack-like defects, as well as the extent of any structural noise. In this approach, the FMC data of a specific defect is simulated in turn on the nodes of a 2-D grid in front of the array. Then the characterisation algorithm is applied to the defects at each grid-node location and the result is compared to the true defect characteristics. This would create a performance map and will enable us to understand where the methods work best and where they fail as well as providing a basis for quantifying future developments.

As a case study, the *database similarity metric method* [68], described in Chapter 4, section 4.5, which is developed to characterise small crack-like defects by measuring S-matrix of a defect and comparing it to a large database of pre-computed S-matrices for varying crack-like defects is assessed and the key factors governing its performance are identified. At the end of the Chapter, the simulations are verified by comparing the characterisation performance of simulated crack-like defects with experimental measurements.

4.2 Defect Simulation

In order to investigate the performance of a given characterisation method, the hybrid forward model discussed in Chapter 3 is used to simulate the full matrix capture (FMC) corresponding to a defect at any given location relative to the array. The hybrid model assumes a two-dimensional (2-D) geometry and planar crack-like defects of negligible width, with two key characteristics of size, l, and orientation angle, α, as shown in Figure 4.1 (b). The orientation angle of the crack-like defect refers to the anti-clockwise angle from the horizontal and can vary from $-{}^{\pi}/_{2}$ to ${}^{\pi}/_{2}$.

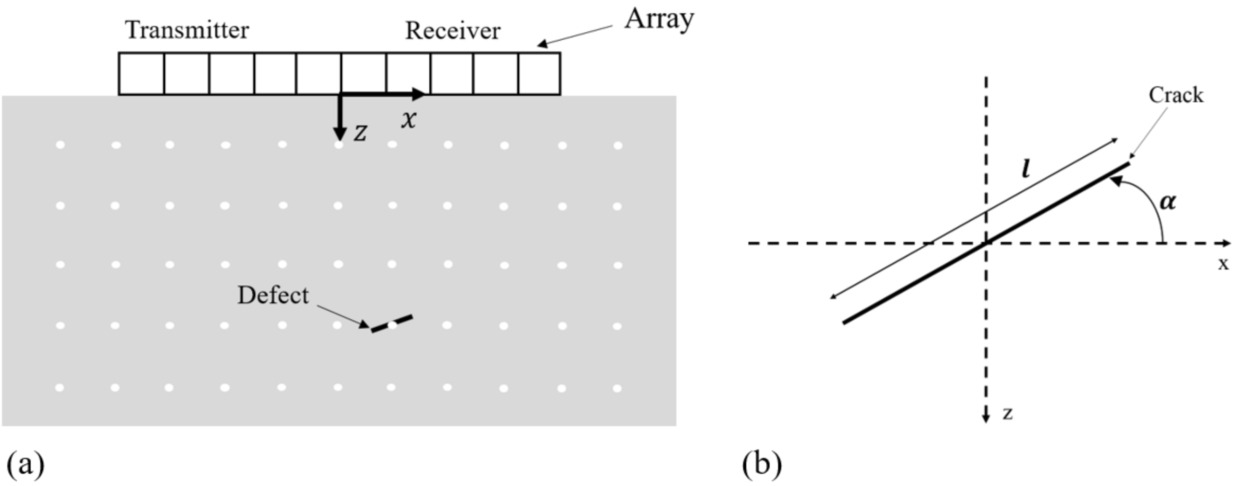

Figure 4.1: Schematic diagram of (a) geometry of 2D space in front of the array that is discretised into a grid and (b) geometry of crack orientation angles.

In this Chapter, a linear ultrasonic array is used throughout with parameters given in Table 4.1. This is an arbitrary choice as it is a commonly used array in industry [46]. However, the proposed assessment method is general and any other array configuration can be used. Figure 4.2 shows TFM images of two 1.5 mm, 30° crack-like defects simulated (using equation (3.1) and the methods described in Chapter 3, section 3.2) at two different locations with respect to the array. From these images, it is apparent that the defect response is strongly dependent on location and for the left-hand defect, it is difficult to say whether it is one or two defects. This makes reliable characterisation, which aims to resolve such uncertainties, challenging and is at the root of the spatial characterisation performance variations discussed in this Chapter.

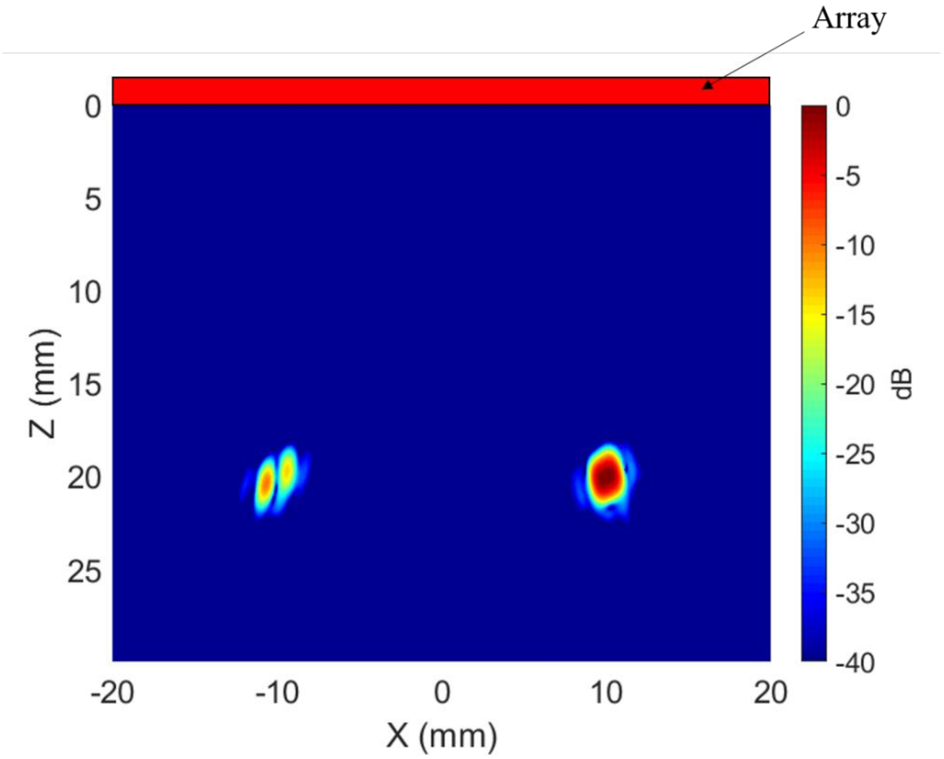

Figure 4.2: TFM image of the same simulated crack-like defect (l = 1.5 mm, α = 30°) at different locations in a noise free material using a 64-element array with centre frequency of 5 MHz and pitch of 0.59 mm (0.5λ).

Table 4.1: Array transducer parameters used in experiments and simulations.

Array parameter	Value
Number of elements	64
Element width (mm)	0.53
Element pitch (mm)	0.63
Element length (mm)	15
Centre frequency (MHz)	5
Bandwidth (-6 dB) (MHz)	3-7

4.3 Spatial Assessment of Characterisation Methods

An assessment method is now developed to spatially map how a given characterisation algorithm performs on a specific type of defect. Firstly, the FMC's corresponding to a specific defect is simulated, located in turn on the nodes of a 2-D grid in front of the array (as shown in Figure 4.1 (a)). At each grid-node location, the characterisation algorithm is applied, and the result is compared to the known true defect, creating a performance map. Maps can then be generated for different conditions such as different defect type, material noise and array type to see the effect of each variable on the performance. This assessment methodology is now introduced and demonstrated using a case study on the *database similarity metric method* [68] which is a characterisation method that has shown promise for small crack-like defects.

4.3.1 Spatial Mapping Assessment Method

In order to assess the *database similarity metric* characterisation method, each step of the algorithm is explored. Firstly, this method as well as other characterisation approaches [69, 70, 75] use the extracted S-matrix and so the quality of this step is examined by simulating defects in a noise free medium. The measured S-matrix, S_m is then extracted (using the method explained in section 2.4.2 of Chapter 2) from this noise free FMC data set at the true centre of the simulated crack-like defect. Then S_m is compared to the true S-matrix in the centre frequency (S_t) of the simulated defect using correlation coefficient [68]:

$$\rho = \frac{\sum_{i=1}^{N}\sum_{j=1}^{N}(S_m(i,j) - \bar{S}_m)(S_t(i,j) - \bar{S}_t)}{\sqrt{\left(\sum_{i=1}^{N}\sum_{j=1}^{N}(S_m(i,j) - \bar{S}_m)^2\right)\left(\sum_{i=1}^{N}\sum_{j=1}^{N}(S_t(i,j) - \bar{S}_t)^2\right)}} \tag{4.1}$$

where N is the total number of corresponding incident/scattering angles (i.e. number of subarrays), S_m and S_t are of size $N \times N$, and $\bar{S}_m$ and $\bar{S}_t$ are the mean values of the matrices

S_m and S_t respectively. By using equation (2.11), a correlation coefficient (CC) can be calculated for each grid point in front the array.

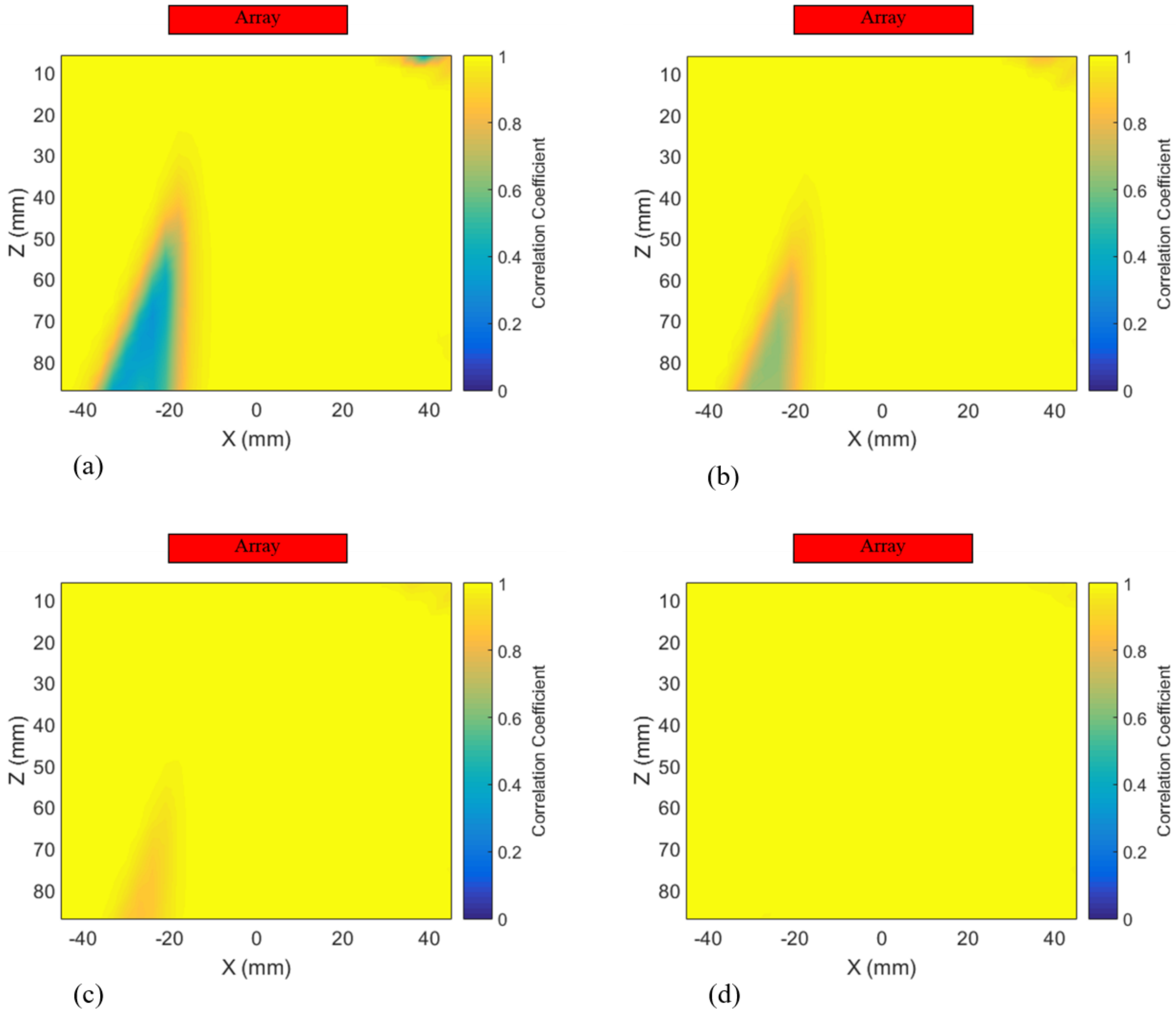

Figure 4.3: Spatial maps of the correlation coefficient between true and measured S-matrices for a simulated crack-like defect (l = 1 mm, α = 30°). Hanning filter with bandwidth of (a) 50%, (b) 25%, (c) 15% and (d) 5% is applied.

Figure 4.3 shows spatial maps of the CC between S_m and S_t for a simulated crack-like defect with a size of 1 mm and orientation angle of 30°. In Figure 4.3 (a - d), Hanning filters of different bandwidths are used, from which it can be seen that a narrower bandwidth, results in a higher CC, which would lead to better characterisation. This is due to the fact that the S-matrices in the database are calculated at a single central frequency and so, as the bandwidth of the simulated measurement narrows, the extracted S-matrix tends to the single frequency case. From Figure 4.3, it is also shown that whilst the filter bandwidth has a major impact on a specific area, much of the region in front of the array is unaffected. Figure 4.4 shows TFM images of a 1 mm, 0° crack when using filter bandwidths of 100% and 15%. For the remainder of this thesis, a bandwidth of 15% is used as a good compromise between imaging resolution and characterisation performance.

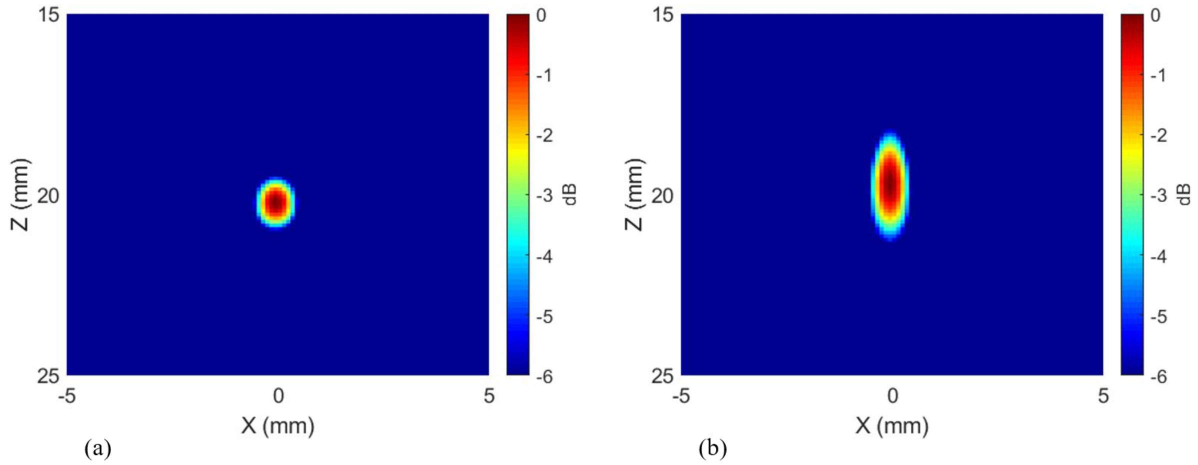

(a) (b)

Figure 4.4: TFM images of a 1 mm, 0° crack, using a 64-element array with centre frequency of 5 MHz and pitch of 0.5λ. In (a) filter bandwidth of 100% and (b) filter bandwidth of 15% is applied.

4.3.2 Assessment of Characterisation Methods

Spatial mapping can be used to quantitatively assess performance of characterisation methods, in which case the measured characteristics of each simulated defect (such as size and orientation angle) are compared with the true characteristics, and the error between them is used in the mapping. The error in size of a crack-like defect is given by:

$$e_l = |l_m - l_t| \tag{4.2}$$

where l_m is the measured length of the crack-like defect using a given characterisation algorithm and l_t is the true length. Similarly, the error in orientation angle of a crack-like defect is given by:

$$e_\alpha = |\alpha_m - \alpha_t| \tag{4.3}$$

where α_m is the measured orientation angle of the crack-like defect using a characterisation algorithm and α_t is the true orientation angle. e_α is always the smallest angular difference between the true and characterised orientation angles, which is necessarily equal or less than $\pi/2$.

This assessment can also be performed in the presence of various forms of noise, such as coherent grain scattering noise, to assess the sensitivity of characterisation methods to the noise. Here, experimentally measured grain noise is added to the simulated FMC data in the time domain [124]. This is done by placing an array with the specifications given in Table 4.1, on a block of bright mild steel (080A15) with no defects and experimentally capturing the FMC data set $f_{n(e)}(T_x, R_x, t)$ which only contains data from material grain noise. In order to produce various levels of material noise, the experimentally measured material noise is multiplied by an amplification factor, A, before being added to the defect's simulated FMC $f_d(T_x, R_x, t)$. This addition of noise is given as:

$$f_c(T_x, R_x, t) = f_d(T_x, R_x, t) + A f_{n(e)}(T_x, R_x, t) \tag{4.4}$$

where f_c is the total combined FMC in time domain, f_d is the FMC simulated using the method in Chapter 33, A is the amplification factor or noise level (level 1 corresponds to bright mild steel noise) and $f_{n(e)}$ is the experimentally captured noise FMC. This results in a FMC data set that contains a simulated defect in a noisy medium. It is noted that the simple addition approach used here inherently ignores multiple scattering between the defect and the grains, which is only physically correct if the scattering is weak. Hence for more highly scattering examples, this method will be prone to errors.

Figure 4.5 illustrates the spatial performance of the *database similarity metric method*. Figure 4.5 (a) and (b) show the error map in size and orientation angle for a simulated crack-like defect (l = 1 mm, α = 60°) respectively. The imperfections seen in these plots are due to the measured S-matrices being extracted from the maximum TFM amplitude, which could be slightly different from the true centre of defects (where the database S-matrices are calculated from). Figure 4.5 (c) and (d) illustrate those with presence of grain noise extracted from bright mild steel (080A15), i.e. A = 1. By comparing Figure 4.5 (a) and (b) with Figure 4.5 (c) and (d), the effect of noise at different locations can be observed, where errors are generally higher and some areas towards the bottom left are more significantly affected.

The effect of noise on the defect characterisation performance is further investigated through a range of noise levels (by varying the amplification factor A). Spatial error maps were then created for six different realisations of noise (by measuring FMC data at six different locations of the defect-free mild steel sample) and then an average of these error maps was taken.

Figure 4.6 shows the spatial error in defect size in presence of a range of noise levels and for different crack sizes and orientation angles. Each column represents a specific level of grain noise starting from A = 0, where simulated defects are noise free. Noise level of A = 1 represents the grain noise from a bright mild steel (080A15). The other two noise levels show the noise amplitude multiplication factor A = 0.5 and A = 2. In Figure 4.6 (a), each row represents a specific orientation angle where the size was kept constant at 1 mm. In Figure 4.6 (b) however, the orientation angle is kept constant at 30° where each row represents different crack lengths. Figure 4.7 is similar to Figure 4.6, except that it shows performance in characterising the orientation angle of crack-like defects. Taken together, Figure 4.6 and Figure 4.7 give an overall spatial view of the performance of the *database similarity metric method* against structural noise and defect type. The next section seeks to understand the reasons for the form of these spatial performance maps.

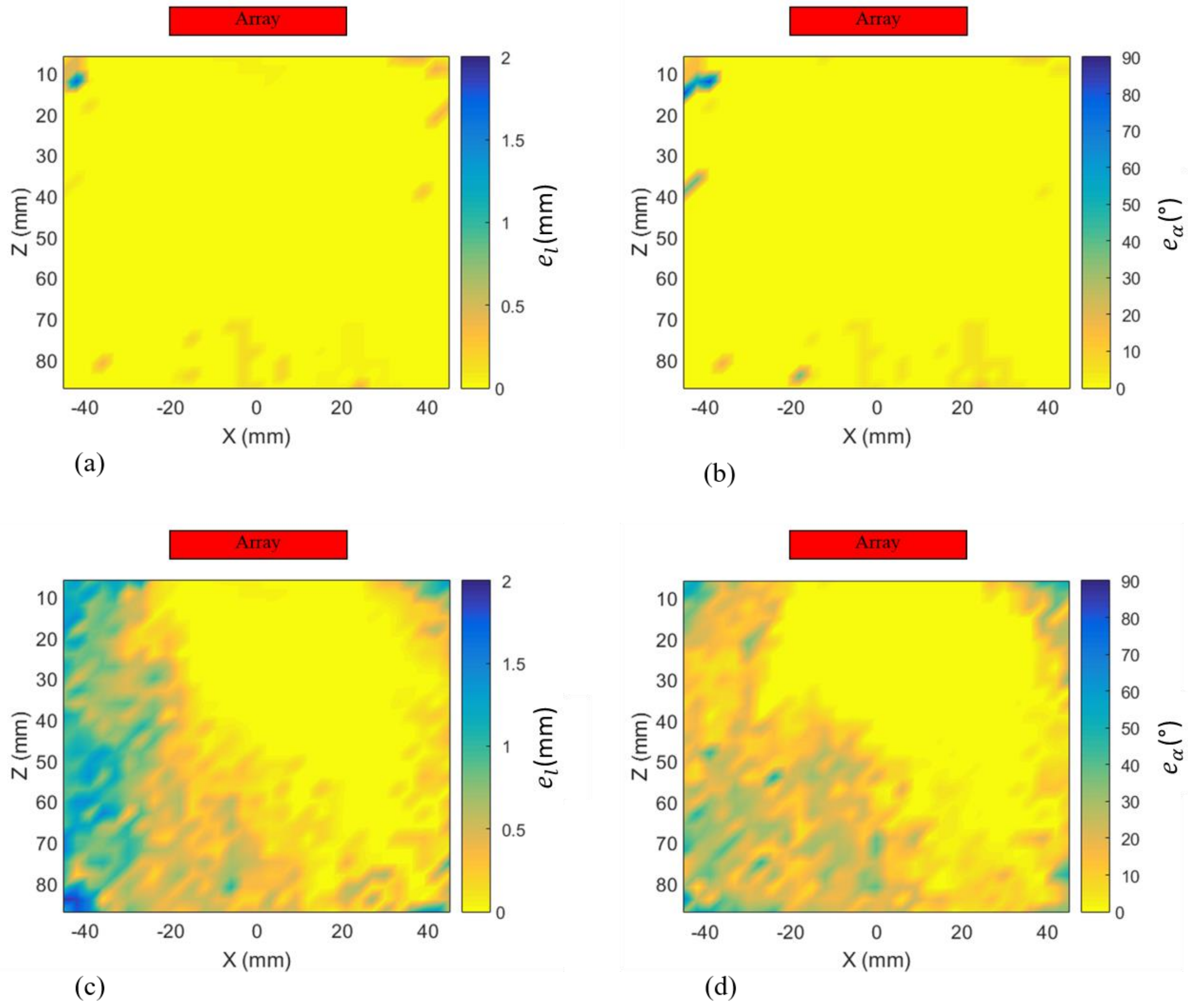

(a) (b) (c) (d)

Figure 4.5: Spatial map of error in (a) size and (b) orientation angle of a simulated crack-like defect (l = 1 mm, α = 60°) in a noise free medium. (c) size error and (d) orientation angle error with presence of steel grain noise, A = 1. All maps cover a 2D (*x*-*z*) space from -45 mm to 45 mm in '*x*' dimension and from 3 mm to 90 mm in '*z*' dimension.

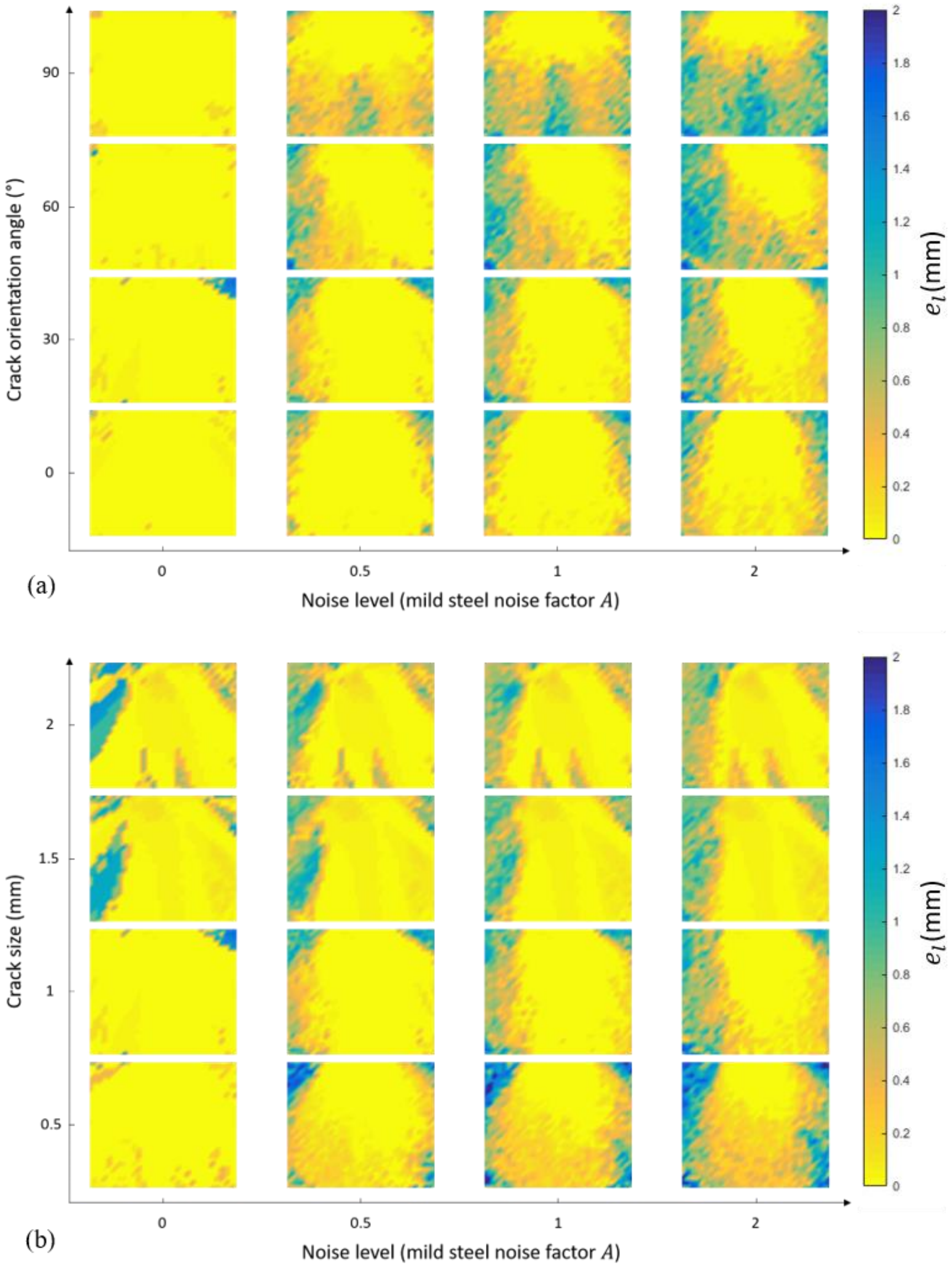

Figure 4.6: Comprehensive graph illustrating performance of *database similarity metric method* in characterising size of crack-like defects against different noise levels. (a) performance against true orientation angle and (b) performance against true size of simulated crack-like defects. True simulated defect size in (a) is 1 mm and true simulated defect orientation angle in (b) is 30°. Geometries are the same as in Figure 4.5.

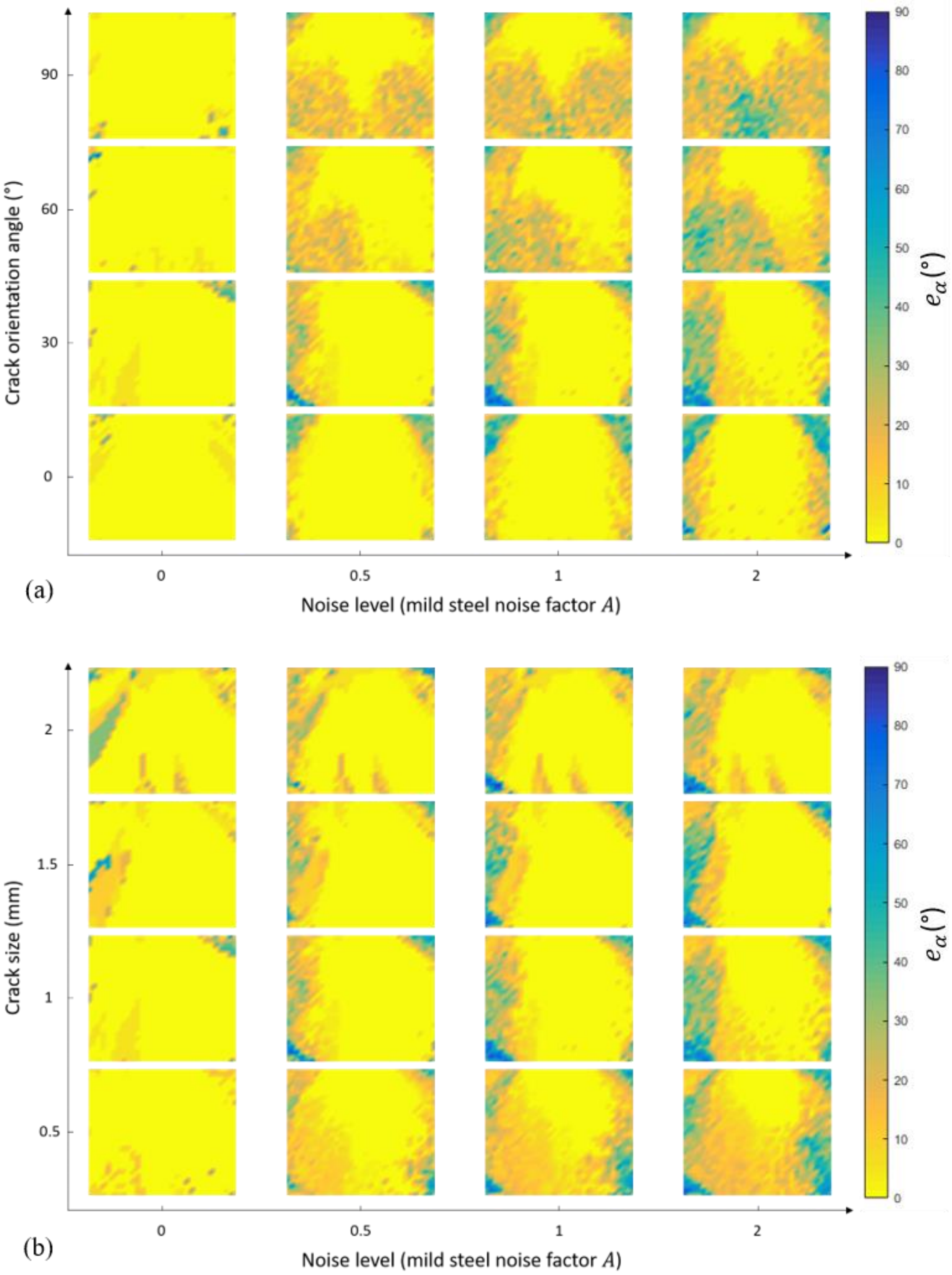

Figure 4.7: Comprehensive graph illustrating performance of *database similarity metric method* in characterising orientation angle of crack-like defects against different noise levels. (a) performance against true orientation angle and (b) performance against true size of simulated crack-like defects. True simulated defect size in (a) is 1 mm and true simulated defect orientation angle in (b) is 30°. Geometries are the same as in Figure 4.5.

4.4 Discussion

As it can be seen from Figure 4.6 and Figure 4.7, the patterns of maps show distinctive shapes. For example, by looking at Figure 4.6 (b) and Figure 4.7 (b), the characterisation performance is better for larger cracks, which can be expected as the reflected signals will be larger and therefore the characterisation becomes less sensitive to noise. However, it can also be seen that the characterisation performance of the larger defects is still sensitive to the location of defect. This can be explained by considering the SNR for each point (assuming a simplified noise model) in the spatial map (x, z) which can be written as [115]:

$$SNR(x,z) = \frac{q(x,z)}{\sigma} \frac{|P(x,z,x,z)|}{\sqrt{\int\int |P(x,z,\ x',z')|^2 dx'dz'}} \tag{4.5}$$

where $q(x, z)$ is the maximum TFM amplitude from the defect (i.e. signal), σ is the noise intensity equivalent to the Figure of Merit (FOM) [125], $P(x, z, x', z')$ is the point spread function (PSF) of the point of interest in the map (x, z) as a function of the surrounding area (x', z'). The quantity $|P(x,z,x,z)|/\sqrt{\int\int |P(x,z,\ x',z')|^2 dx'dz'}$ is equivalent to the reciprocal of the normalised root sum square of the PSF. Equation (4.5) assumes that each grain is an omni-directional scatterer regardless of incident angle and there is no spatial correlation between material scattering from different positions [115].

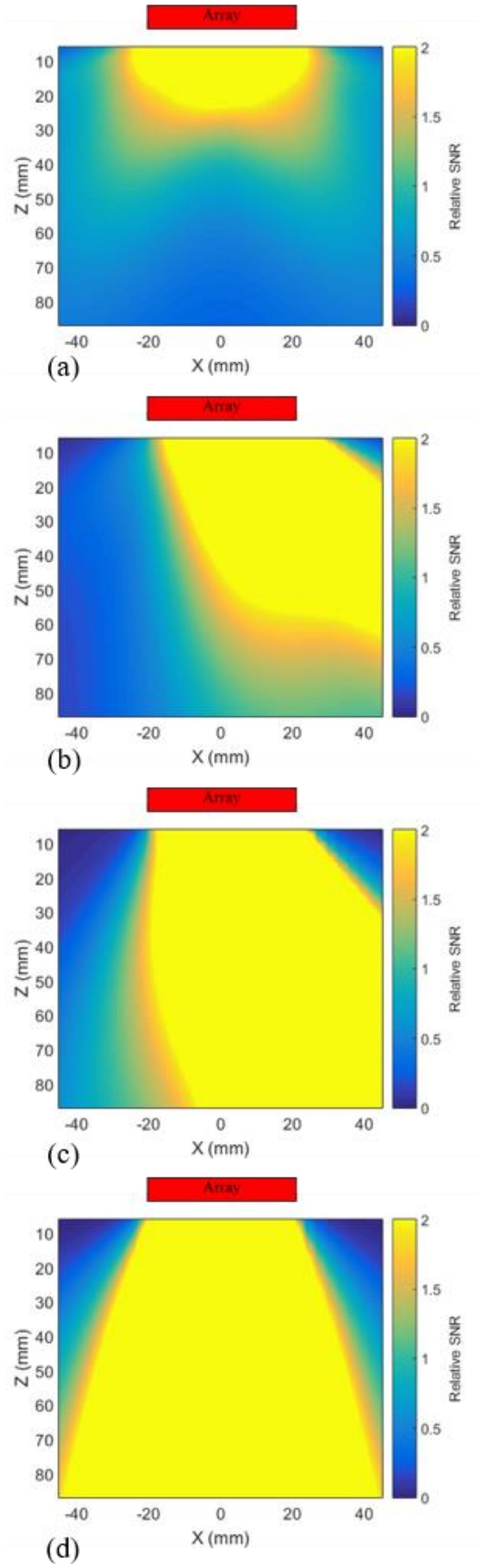

Figure 4.8: Spatial maps of the relative SNR for crack-like defects of size 1 mm and orientation angles of (a) 90°, (b) 60°, (c) 30° and (d) 0°, calculated from equation (4.5).

Figure 4.8 (a) to (d) show the spatial maps of SNR, calculated from equation (4.5), for crack-like defects of size 1 mm and various orientation angles. Figure 4.8 suggests that the general patterns of the error maps in Figure 4.6 (a) and Figure 4.7 (a), with high levels of noise, can be explained by the defect SNR. This will, for example, mean that crack-like defects are better characterised when the array receives the high amplitude (and hence high SNR) specular reflection for the crack face. This is most obvious when comparing the columns on the right-hand side of Figure 4.6 (a) and Figure 4.7 (a), where noise level is highest, with Figure 4.8.

It is also important that the measured S-matrices correlate well with a single element of the database and poorly with the other elements. It is hypothesised that this is most likely to happen when the S-matrices are *information rich*, which means that the S-matrix varies (i.e. has distinct features) over the measured angular range. Conversely, if the measured S-matrix is constant over the angular range, this would be *information poor* and hence it is likely to show a high correlation with other similar shaped S-matrices, including the correct S-matrix in database. This is analogous to the situation in voice recognition and fingerprinting, where the recorded voice or the scanned fingerprint is checked with a large database to find the best match [126–129]. The more features in the captured data, the more likely to find the right match. One simple way to quantify this uniqueness, is to see how many S-matrices in the database have a CC with the measured S-matrix equal or greater than a specific threshold in a noise-free condition. The more database S-matrices above this threshold, the more likely the characterisation method is to fail in presence of noise.

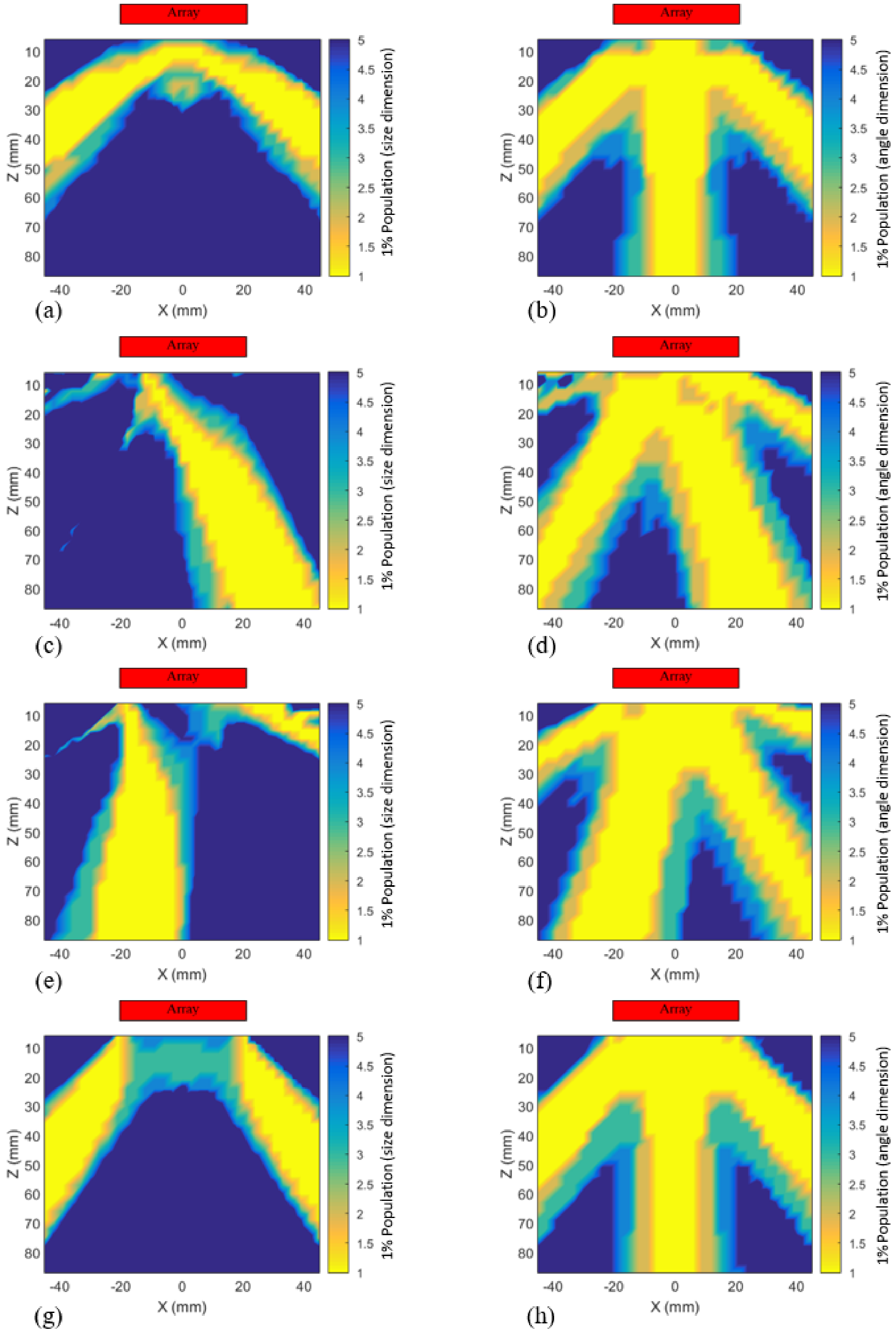

Figure 4.9: Spatial maps of the 1% population in the field of correlation coefficient with the database in (a), (c), (e), (g) size dimension and (b), (d), (f), (h) angle dimension. Rows one to four from the top correspond to crack-like defects of size 1 mm and orientation angles of 90°, 60°, 30° and 0° respectively.

Figure 4.9 illustrates this by taking the number of S-matrices in database whose CC with the measured S-matrix is above 0.99 of the maximum CC with the entire database (or within 1% from the max CC). This metric (termed the 1% population) can be used to measure uncertainty in both size and orientation angle characterisation. The left column of Figure 4.9 shows uncertainty in size characterisation (corresponding to Figure 4.6 (a)), and the right column demonstrates uncertainty in orientation angle characterisation (corresponding to Figure 4.7 (a)). Figure 4.9 suggests that characterisation in the regions with large 1% population (blue regions) should be more sensitive to the material noise. This information uniqueness metric again favours crack-like defects located such that the array receives the specular reflection, however, other regions also have high uniqueness leading to features, such as the three-pronged shapes seen in Figure 4.6 (a) and Figure 4.7 (a). The 1% population metric together with the SNR, explain the forms of the results seen earlier in Figure 4.6 and Figure 4.7.

4.5 Experimental Results

The proposed spatial mapping assessment method is now validated through experimental measurements. Figure 4.12 shows a comparison between the error in characterising simulated crack-like defects and characterising real experimental crack-like defects (EDM notches cut with a 0.1 mm thick wire) in bright mild steel (080A15). Figure 4.10 shows the experimental setup and a schematic diagram of the defects and Figure 4.11 shows photos of the actual samples. All experiments are carried out by me using an array controller manufactured by Peak NDT and phased arrays manufactured by Imasonic. Array parameters are shown in Table 4.1 and Table 4.2 shows the details of the experimental defects. It should be noted that it is difficult to manufacture real cracks with different orientation angles at different locations. Instead, EDM notches were used as the closest manufactured crack-like defects. In order to plot the error in characterising simulated crack-like defects, 16 coherent noise realisations have been used for each location along *x*-axis and the maximum error (dashed lines), minimum error (dotted lines) and mean error (solid lines) are plotted in increments of 3 mm along *x*-axis. Measurements along the *x*-axis were taken in increments of 15 mm by moving the array from the far right (such that the defect is located at -45 mm in *x*-axis from the centre of the array) to far left (such that the defect is located at 45 mm in *x*-axis from the centre of the array). Each error bar represents 5 measurements along the y-direction (in thickness direction) and shows the mean error of the 5 measurements and the maximum and minimum errors. The left and right columns in Figure 4.12 show error in size and orientation angle respectively. Rows one to four from the top represent defects A to D respectively (see Table 4.2). Figure 4.12 suggests a good overall agreement between the experimental and simulated characterisation errors. The average error differences between simulation and experimental results in size characterisation is 0.20 mm and in orientation characterisation is 5.87°. The small differences seen, are thought to be due to the assumption in simulations that crack-like defects have zero width. So, the diffraction from experimental notch tip would be slightly different from the zero-width simulated crack-like defect tips. Experimental results can also be affected by the steel block’s surface and coupling conditions at specific locations and the spatial variation in grain noise.

Table 4.2: Details of crack-like defects used in experiments.

Defect	Z (mm)	Length (mm)	Orientation angle (°)
A	20	1	0
B	50	1	0
C	20	1	30
D	50	1	30

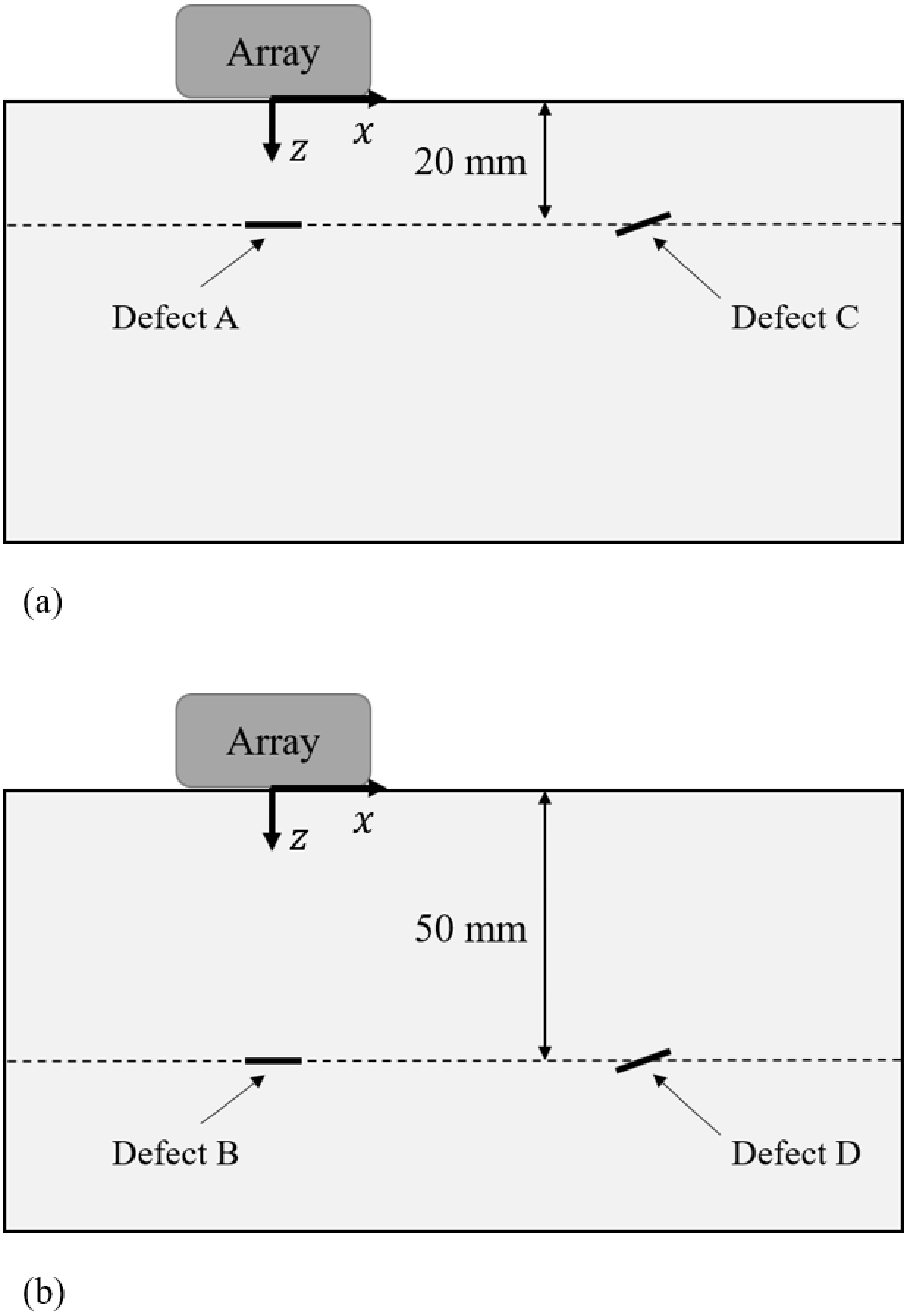

Figure 4.10: Schematic diagram of the experimental setup and defects (EDM notches). (a) shows defects A and C and (b) shows defects B and D from Table 4.2.

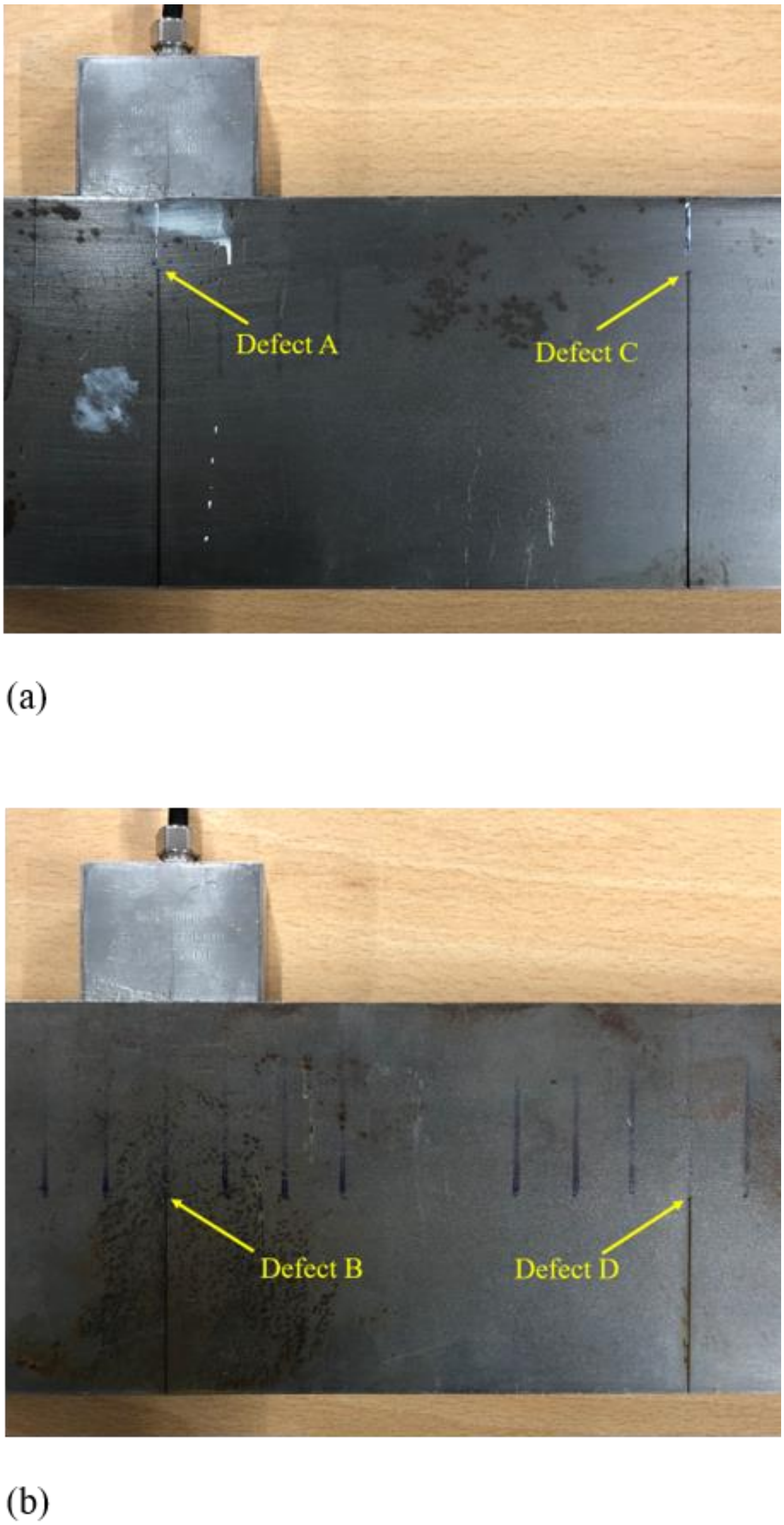

Figure 4.11: Photos of the actual samples corresponding to Figure 4.10.

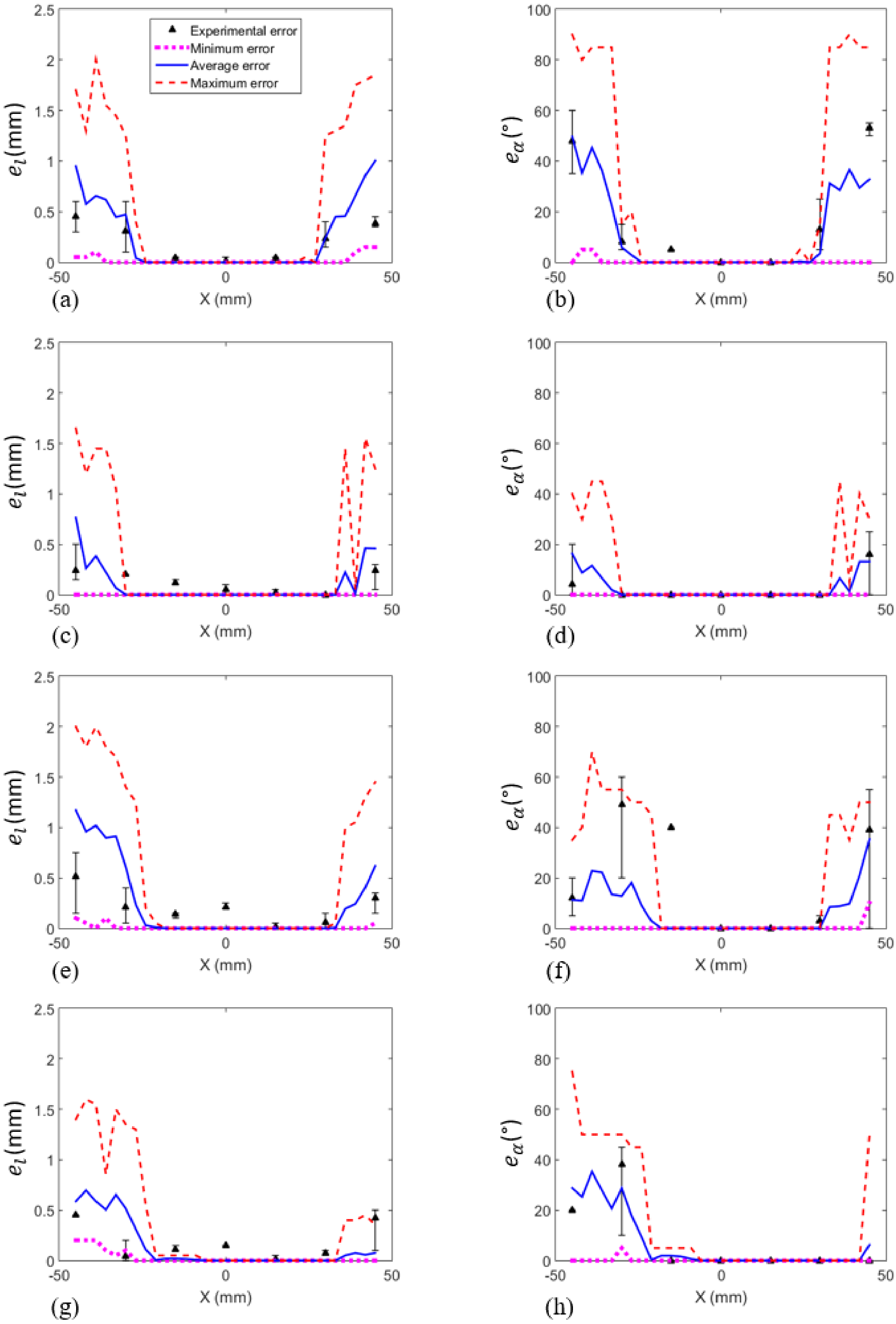

Figure 4.12: Experimental error in measuring (a), (c), (e), (g) size and (b), (d), (f), (h) orientation angle of two different crack-like defects (l = 1 mm, α = 0° and l = 1 mm, α = 30°) at two different depths. Rows one to four from the top represent defects A to D respectively.

4.6 Implications for NDE

With the increasing availability of computing power, it is expected that more complex algorithms for defect characterisation will emerge and therefore, a robust evaluation method is required in order to identify their strengths and weaknesses. The approach described here is believed to be the first example of an assessment methodology for defect characterisation in NDE, which provides a comprehensive and quantitative evaluation. The main finding of this Chapter is the fact that in a defect characterisation method, there could be a wide range of variables, which can affect the performance of the method. For example, in a method that is based on extraction of the defect's S-matrix, the extraction algorithm is critical and as an example, the frequency filter bandwidth can impact the results significantly. The performance of characterisation methods also depends on many other conditions such as the ultrasonic instrument that is being used and its properties, the level and type of present noise and the position, shape and type of defects. As a result, in order to fully assess the performance of a characterisation approach, ideally, all these variables need to be taken into consideration, otherwise, assumptions must be made to reduce the number of variables. Here it is attempted to consider some of these variables (i.e. level of noise, location, size and orientation of cracks). By knowing what variables can affect a specific defect characterisation method and to what extent, it can be fine-tuned and improved to achieve the desired performance for specific scenarios. Even though here only a particular array and characterisation method for small cracks are used, the proposed approach is general and hence has the potential to be used in or adopted to other occasions and can be extended to any characterisation method, defect type and array configuration.

4.7 Conclusion

A spatial mapping approach is introduced to assess the performance of characterisation methods in the imaging plane of an array. This method takes advantage of modern computer power to rapidly simulate the FMC data from arbitrary defects at arbitrary locations and then apply the characterisation method of interest to each simulated defect. As a case study, the performance of the *database similarity metric method* for the characterisation of small crack-like defects has been examined. Using spatial assessment, the key factors impacting the performance of the *database similarity metric method* have been identified and it is shown that grain noise can have a significant effect on particular regions whilst leaving other regions relatively unaffected. It is further shown that the location of regions of good performance can vary significantly depending on the size and orientation of the crack. It was shown that the defect SNR and the S-matrix uniqueness govern this spatial distribution characterisation performance. Simple models were developed that allow the regions of good performance to be predicted. Finally, the spatial error maps have been verified by comparing the characterisation errors found in simulation with those measured in experiments on steel samples with EDM notches. The average of differences between simulation and experimental results were 0.20 mm in size and 5.87° in orientation characterisation. It is also worth noting that the proposed assessment methodology could be extended to produce a 3D spatial map, in order to assess more characterisation methods that would be possible with 2D arrays.

Chapter 5

Array Design Optimisation for Defect Characterisation

5.1 Introduction

This Chapter is based on a journal article submitted to “Ultrasonics” in November 2019 for publication, where I was the main author and all other co-authors had a supervisory role.

There have been variety of methods introduced to characterise crack-like defects using ultrasonic arrays, some of which have been discussed in the literature review in Chapter 2. For larger cracks, defect characteristics can be measured directly from the images, for example by selecting a box around the defect which covers the pixels within −6 dB of its maximum amplitude [75] as explained in Chapter 2, section 2.4.3.1. For cracks comparable to or smaller than the ultrasonic wavelength, characterisation techniques have been developed to extract the scattering coefficient matrix (S-matrix) and use this as the basis for defect characterisation [68, 101]. Two of these methods are discussed in Chapter 2, section 2.4.3. This family of S-matrix characterisation methods has been shown to have good performance, particularly for small defects; hence one such method is adopted in this Chapter.

Ultrasonic phased arrays are typically designed to achieve optimal imaging performance, for example by keeping the pitch to half wavelength of the centre frequency to avoid grating lobes and selecting the highest frequency available to achieve adequate signal-to-noise performance at some predefined penetration depth. However, it is currently unknown whether an optimal phased array for detection and imaging is also optimal for defect characterisation in all scenarios and in what way and to what extent characterisation is affected by array parameters.

This Chapter aims to investigate the effect of ultrasonic array parameters on defect characterisation and explore the possibility of optimised array designs for this purpose. In order to achieve this, it is assumed that the defect has been detected and the requirement is now to determine its characteristics, i.e. size and orientation angle in the case of a crack. The effect of array parameters and parameters associated with the sample and the defect, which have a significant impact on characterisation accuracy, are then explored. Such parameters include aperture size, centre frequency, material noise, defect type and the presence of geometric features such as the back-wall. To simplify the process, here only small crack-like defects are considered since they are challenging to characterise directly from the image as they are comparable in size to the point spread function of the array. The approach used in this Chapter is to simulate defects and grain noise using the method described in Chapter 3, and characterise the defects with the *database similarity metric method* [68] described in Chapter 2, section 2.4.3.3. This allows the comparison of different array designs by measuring their performance in various scenarios. Using the scenario of a crack in a mild steel plate as a case study, various optimal arrays are proposed dependent on the design requirements.

5.2 Defect Simulation

In order to examine the performance of a given array design, the hybrid forward model discussed in Chapter 3 is used to simulate the full matrix capture (FMC) corresponding to all the transmit-receive signals. The hybrid model assumes a two-dimensional (2-D) geometry and planar crack-like defects of negligible width, with two key characteristics of size, l, and orientation angle, α, as shown in Figure 5.1 (b). As before, the orientation angle of the crack-like defect refers to the anti-clockwise angle from the horizontal and can vary from $-\pi/2$ to $\pi/2$. Noise is also simulated as described in Chapter 3, where multiple point scatterers are simulated within a square of 10 mm centred to the defect as shown in Figure 5.1 (a).

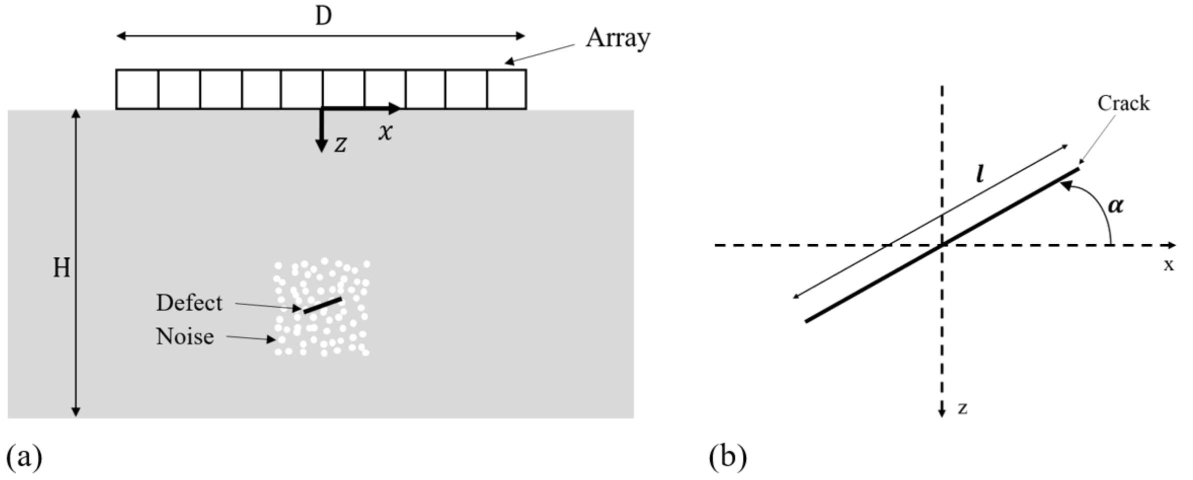

Figure 5.1: Schematic diagram of (a) geometry of the array defect and noise and notations used in equation (5.1) and (b) geometry of crack orientation angles.

Figure 5.2 shows TFM images of two 2 mm, 30° crack-like defects simulated (using equation (3.1) and the method descried in Chapter 3, section 3.2) at 30 mm depth in a block of mild steel and imaged using two arrays with different aperture sizes. From these images, it is apparent that the defect response is strongly dependent on the array specifications.

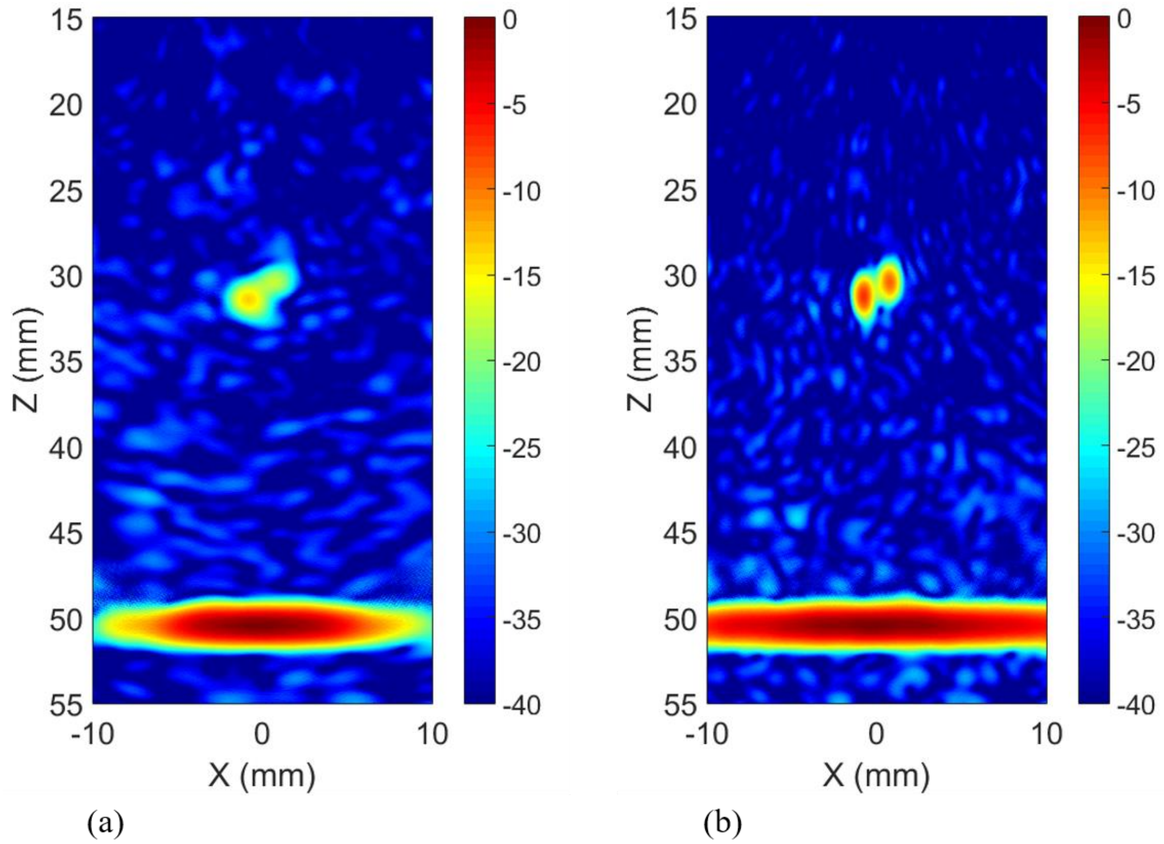

Figure 5.2: TFM image of the same simulated crack-like defect (l = 2 mm, α = 30°) in a mild steel block with (a) a 32-element array and (b) a 64-element array. In both cases, array centre frequency is 5 MHz, with element width of 0.53 mm and pitch of 0.59 mm (0.5λ).

5.3 Effect of Array and Sample Parameters on Characterisation

5.3.1 Array Parameters

Here, the *database similarity metric method* is used to explore the effect of various parameters on defect characterisation. First, the effect of array aperture size and centre frequency on characterisation performance are considered. In order to investigate the effect of each variable, a small crack-like defect with known size and orientation is simulated at depth 30 mm directly below the array (i.e. x = 0, z = 30 mm), as shown in Figure 5.1 (a). This simulation is repeated for arrays of varying aperture size and centre frequencies, while scaling the pitch size to maintain it at half wavelength in order to avoid grating lobes. This pitch scaling was applied as it was found that the presence of grating lobes always led to poor characterisation. For every simulation, a FMC data set ($f_c(T_x, R_x, t)$ in equation (3.4)) is generated and the *database similarity metric method* is applied to assess the characteristics of the defect (i.e. size and orientation angle). The measured defect characteristics are then compared with the true characteristics and the error between them is calculated. The error in size of a crack-like defect is given by equation (4.2) in the previous Chapter:

$$e_l = |l_m - l_t| \tag{4.2}$$

where l_m is the measured length of the crack-like defect using the characterisation algorithm and l_t is the true length. Similarly, the error in orientation angle of a crack-like defect is given by equation (4.3):

$$e_\alpha = |\alpha_m - \alpha_t| \tag{4.3}$$

where α_m is the measured orientation angle of the crack-like defect using our characterisation algorithm and α_t is the true orientation angle. e_α is always the smallest angular difference between the true and characterised orientation angles, which is necessarily equal or less than ${}^{\pi}/_{2}$.

Figure 5.3 (a) to (d) illustrates the error in characterising a simulated crack (l = 1 mm, α = 30°). (a) and (c) show the error in size and orientation angle respectively against array aperture size and material noise level (i.e. A in equation (3.4)), whereas (b) and (d) show the characterisation errors against array centre frequency and material noise. To compare array performance in defect characterisation and detection, the signal to noise ratio (SNR) of the same simulated crack is shown in (e) as a function of array aperture size and material noise level and in (f) as a function of array centre frequency and material noise. In order to calculate the SNR, first the defect is simulated in a noise-free medium (i.e. $A = 0$ in equation (3.4)) and its maximum TFM amplitude is taken as the signal. Then grain noise is simulated at the desired level without the presence of any defect and the root mean square (RMS) of a 10×10 mm box centred at the location of the defect is taken as the noise. It should be noted that when noise level is zero, the SNR would be signal divided by zero, hence the empty results. All error and SNR values are averaged over 120 different realisations of noise.

In Figure 5.3 (a), (c) and (e), centre frequency is kept constant at 5 MHz, the pitch is maintained at $\lambda/2$ and the aperture size is increased by adding elements to the array. Similarly, in Figure 5.3 (b), (d) and (f), aperture size is kept constant at 75 mm and since pitch size is always equal to half wavelength, as the centre frequency increases, the number of elements is increased to compensate for the reduction in pitch size. From the SNR plots (Figure 5.3 (e) and (f)) it can be seen that defect detection has a relatively weak dependency on the array aperture and centre frequency, and is governed primarily by the level of material noise. The exception being the SNR which is improved as the aperture increases from zero to 50 mm. Figure 5.3 (a) – (d) show that defect characterisation is governed by a combination of material noise and the array parameters, and that typically a higher frequency and larger aperture size lead to better characterisation performance. It should be noted that attenuation has been ignored in simulations, which would increase with frequency, meaning that the performance at higher frequencies would in reality be worse than predicted here.

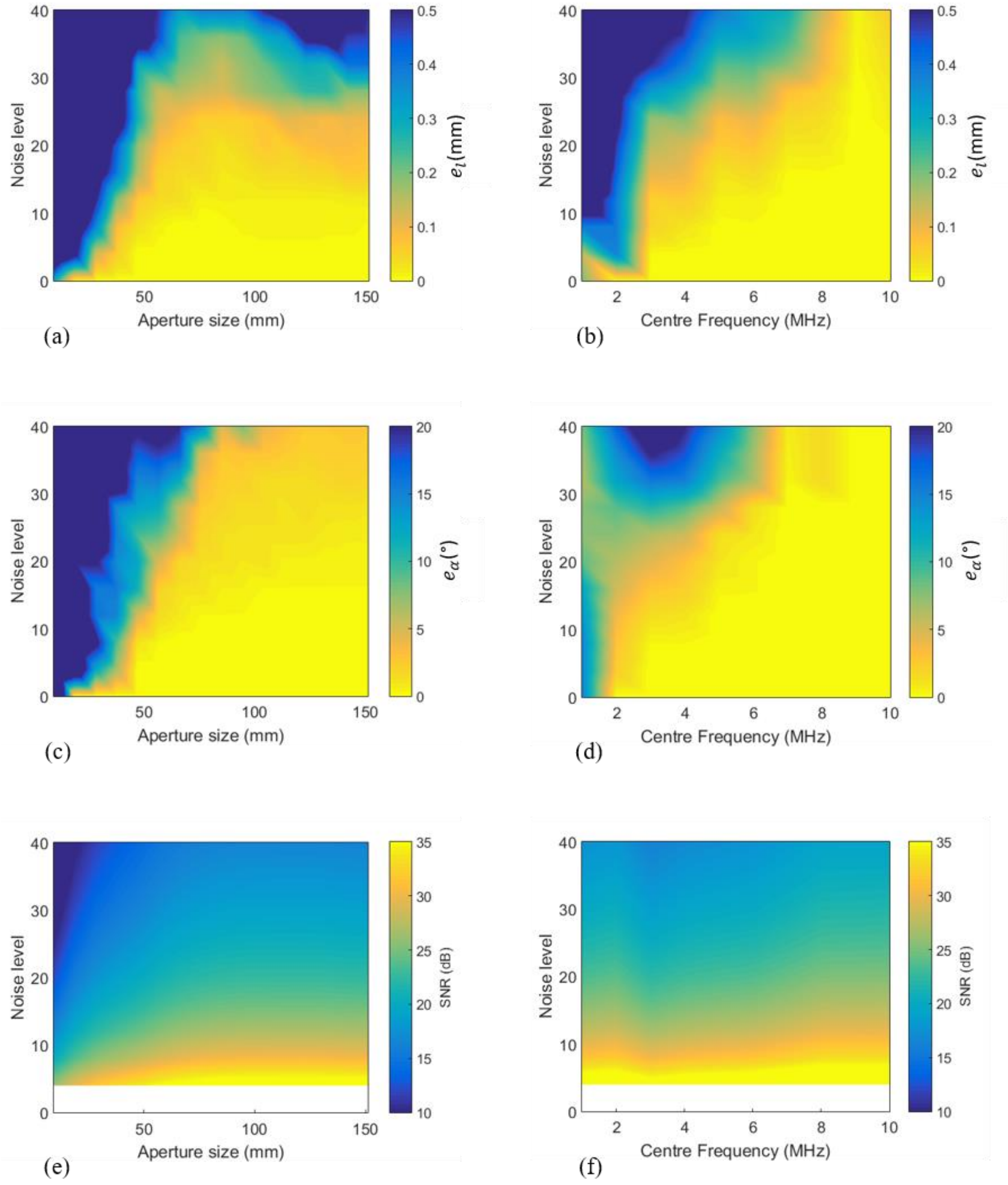

Figure 5.3: Characterisation results for a crack-like defect (l = 1 mm, α = 30°). (a) error in size, (c) error in orientation angle and (e) SNR, with each plot showing this error as a function of array aperture size and material noise level, where array centre frequency is 5 MHz and pitch is 0.5 λ. (b) error in size, (d) error in orientation angle and (f) SNR, with each plot showing this error as a function of centre frequency and noise level, where array aperture size is 75 mm and pitch is 0.5λ.

The plots in Figure 5.3 (a) and (c), which explore the effect of aperture, are now extended for crack-like defects with a range of sizes and orientation angles in Figure 5.4 (a) and (b) respectively. Similarly, the plots in Figure 5.3 (b) and (d), which explore the effect of frequency, are extended for various types of crack-like defects in Figure 5.4 (a) and (b) respectively. Figure 5.4 shows that, overall, by increasing the aperture size of an array, errors in size and angle reduce (the yellow regions grow, and the blue regions shrink) meaning that the characterisation performance is improved. This is thought to be due to the focusing enhancement that is achieved with a larger aperture, as well as the fact that the extracted S-matrices will have a larger range of incident and scattering angles, meaning that it is more likely that the dominating features of the crack’s scattered signal, such as specular reflection, are captured. However, there also seems to be an optimal aperture size for some of the defect types, which is not necessarily the maximum aperture, such as in the 1.5 mm 90° crack in Figure 5.4 (b), where in higher noise materials, there is an optimal aperture size of 130 mm for orientation angle characterisation. This could be due to the fact that by adding more elements to the array, the S-matrix range is expanded, hence capturing further low-amplitude signals that become dominated by noise. This effect can be seen to be particularly significant for 90° cracks where increasing the aperture does not help with capturing the specular reflections. Figure 5.4 also suggests that the accurate characterisation of larger crack sizes and smaller orientation angle cracks, requires a smaller aperture. This is in-line with intuitive thinking that large and normally oriented defects are the easiest to detect and size.

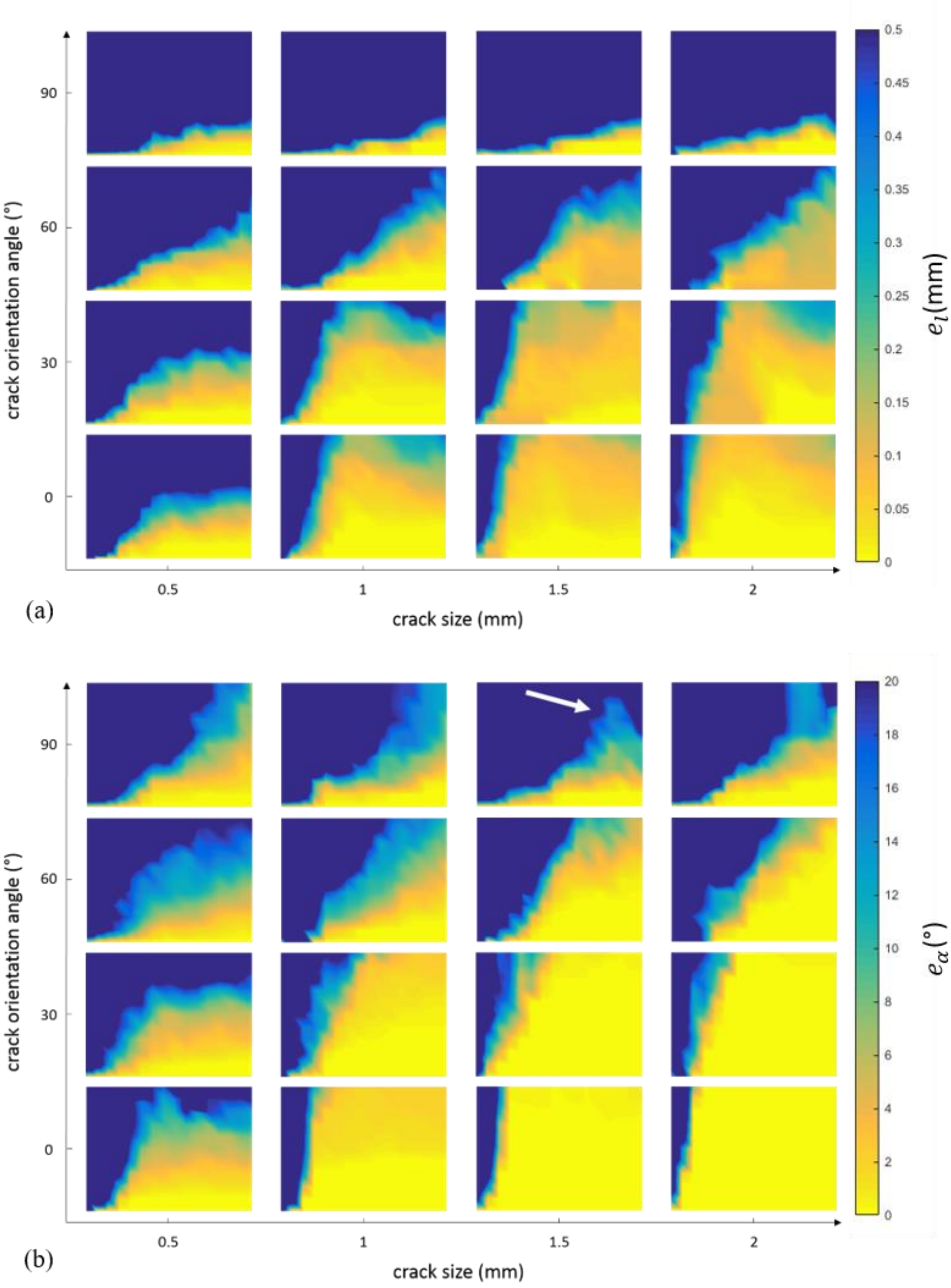

Figure 5.4: Characterisation results for different simulated cracks. (a) error in size and (b) error in orientation angle with each plot showing this error as a function of array aperture size and material noise level, where array centre frequency is 5 MHz and pitch is 0.5λ (similar to Figure 5.3 (a) and (c)).

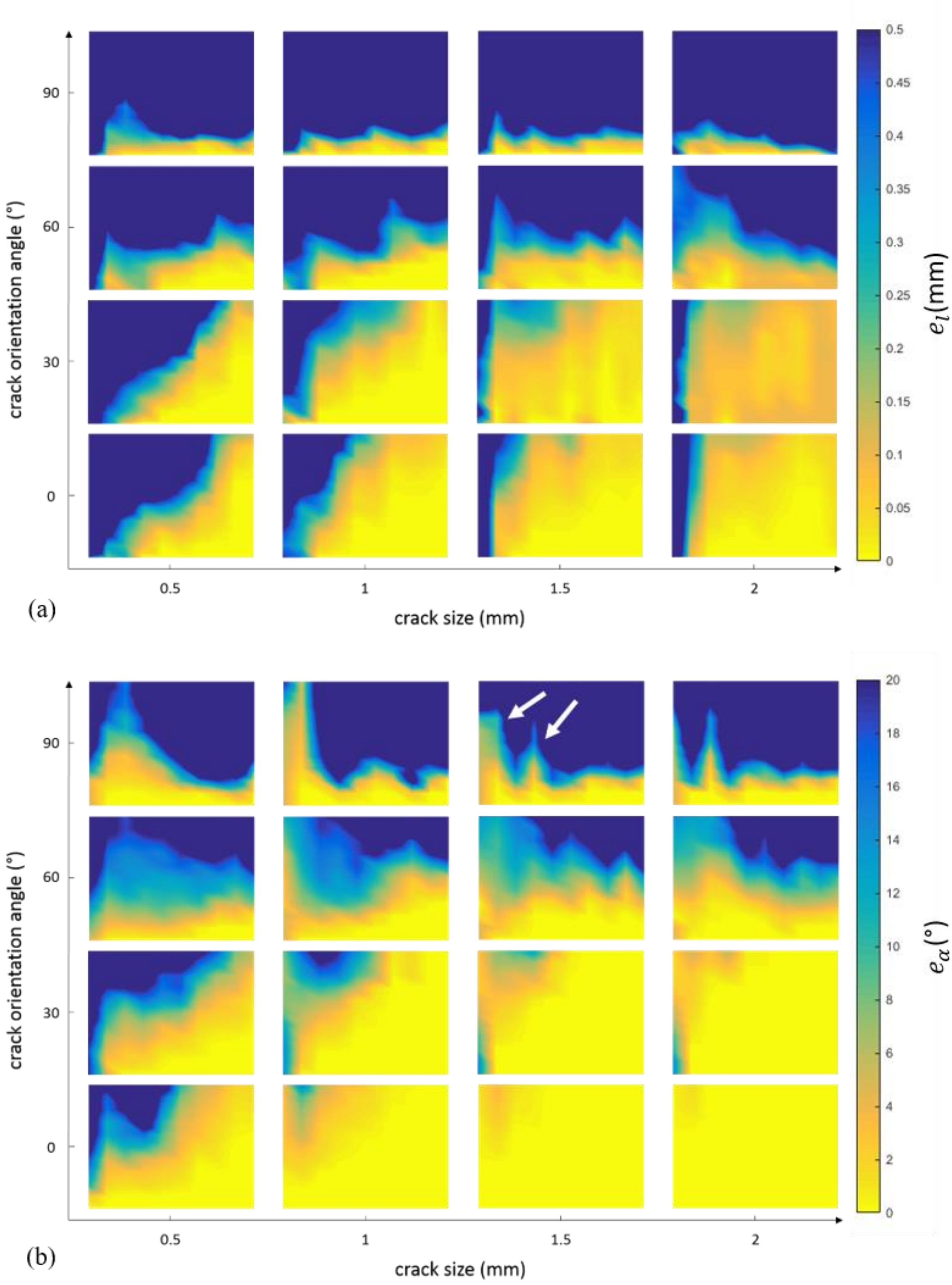

Figure 5.5: Characterisation results for different simulated cracks. (a) error in size and (b) error in orientation angle with each plot showing this error as a function of centre frequency and material noise level, where array aperture size is 75 mm and pitch is 0.5λ (similar to Figure 5.3 (b) and (d)).

Looking at Figure 5.5, it can be seen that for larger crack orientation angles, a higher centre frequency does not necessarily help the characterisation. The different maxima appearing in some of the figures such as in 1.5 mm 90° crack in Figure 5.5 (b) could be due to the fact that by increasing centre frequency, noise intensity is increased as well (because $S_n(\omega)$ is increased in equation (3.3)). This means increasing frequency is a compromise between the effect of noise and resolution, meaning that higher frequencies worsen the effect of noise (see Figure 3.1 (c)), but also improve the ratio of crack size to the wavelength. This causes the CC between the defect's measured S-matrix and its correct analytical S-matrix in the database to oscillate with frequency. For example, for a 1.5 mm, 90° crack, the optimal frequency for orientation characterisation with higher material noise levels would either be 2 MHz or 4 MHz. These frequencies provide the best balance between the effect of noise and resolution.

By looking at the overall extent of the good characterisation regions (yellow), in both Figure 5.4 and Figure 5.5, it can be seen that it is somewhat more challenging to characterise size compared to orientation angle, which is due to the fact that S-matrices are more sensitive to changes in defect orientation than to changes in defect size. That is because changes in the orientation angle cause a simple shift whereas changes in the size cause a more subtle shape change in the measured S-matrices. For example, as the crack size increases, the peaks and troughs of the S-matrix become sharper. This means that the CC is more sensitive to changes in orientation angles than size and therefore orientation characterisation performs somewhat better than sizing. Figure 5.6 (a) shows the normalised S-matrix of a 1 mm, 0° crack. In Figure 5.6 (b), only the size of the crack is increased to 1.5 mm and orientation is kept at 0° whereas in Figure 5.6 (c), only the orientation is changed to 30° and the size is 1 mm. By comparing (a) with (b) and (a) with (c), it is apparent that S-matrices are more sensitive to changes in defect orientation.

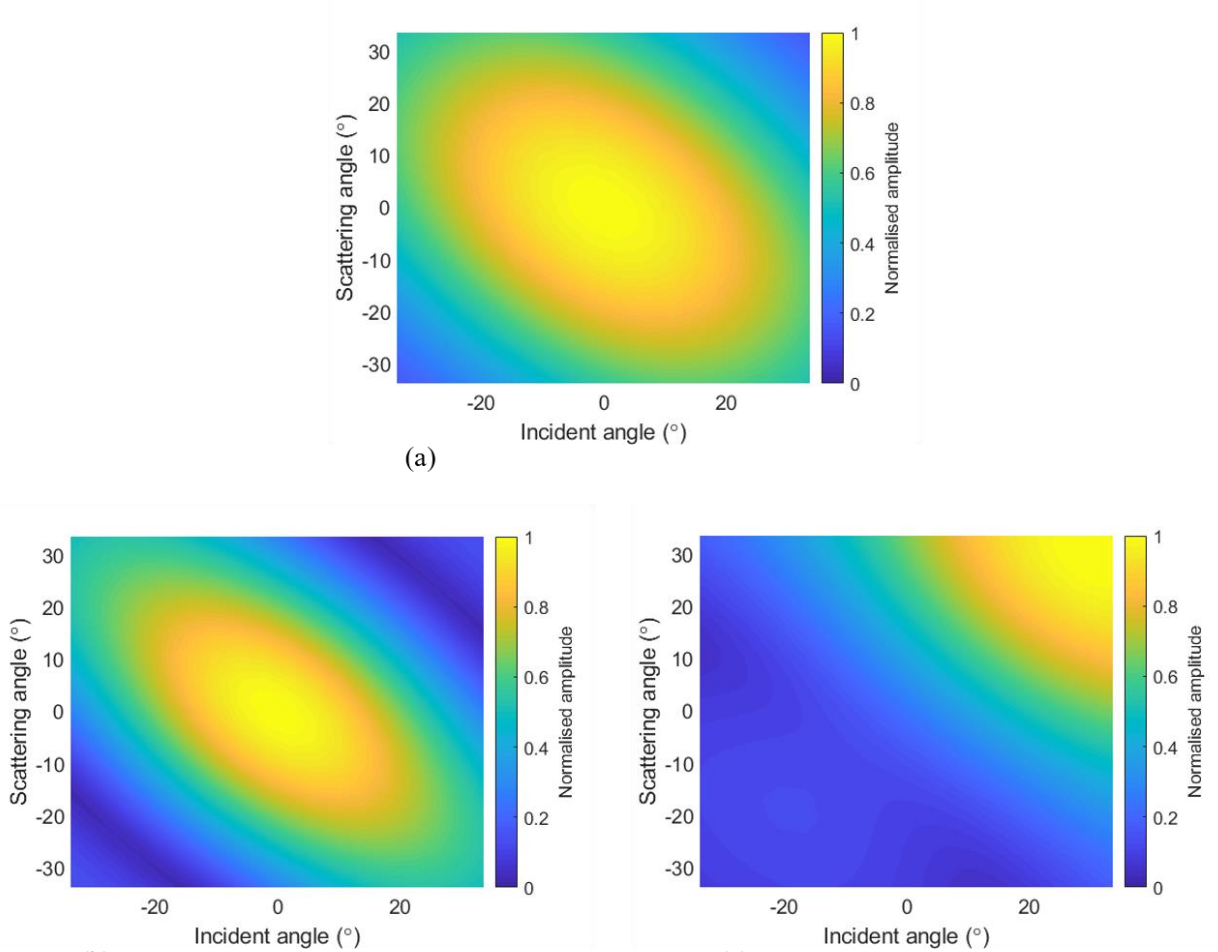

(a)

(b)

(c)

Figure 5.6: Normalised S-matrices of defect with (a) l = 1 mm, α = 0°, (b) l = 1.5 mm, α = 0° and (c) l = 1 mm, α = 30°. Each plot shows the angular range covered by an array of 40 mm aperture size placed 30 mm directly above the defect.

5.3.2 Back-wall Imaging Artefacts

Other than the effects of array parameters, such as frequency and aperture, there are other factors that can interfere with the quality of characterisation. During the investigation of array parameters, it was found that there is always a TFM imaging artefact associated with the back-wall. Figure 5.7 illustrates this artefact for various pitch sizes and as it can be seen, varying the pitch, while the aperture size is fixed, does not change the area affected, but only changes the amplitude of the artefact. It is also noted that when pitch is increased to 2λ, the grating lobe of the defect starts to appear at around -40 dB from the back-wall. The parameters that govern the back-wall TFM artefact region are the array aperture size and the distance from array to the back-wall. Figure 5.8 illustrates how the aperture size can change the extent of this artefact, where widening the aperture, also expands the artefact area. In order to study this effect further, the spatial assessment approach described in Chapter 4 was used to simulate a defect at different positions relative to the array with 2.5 mm increments in both x and z dimensions, and for each case, the defect was characterised and the error between characterisation and true values was mapped. Figure 5.9 demonstrates the spatial map using a 1 mm, 30° simulated crack. Figure 5.9 (a) and (b) are maps of error in size and orientation angle respectively when a back-wall is not present and Figure 5.9 (c) and (d) are those with presence of a back-wall. This figure shows a clear pattern of high error in characterisation, which matches the region of the back-wall imaging artefact whose edges are indicated with red lines. This suggests another factor needs to be considered when optimising an array design, which is the location of the back-wall and defect with respect to the array. Generally, the larger the array aperture and the closer the back-wall is to the array, the larger the region of the artefact in the image. In order for a defect with coordinates (x, z) to remain outside this artefact region, the distsance between the defect and nearest element, and the distance between the defect and farthest element should either be both shorter or both longer than the distance between the array and back-wall (H). Therefore, from geometry, the relationship below must be satisfied:

$$\left| |x| - \sqrt{H^2 - z^2} \right| > \frac{D}{2} \tag{5.1}$$

where D is the aperture size and H is the distance from array to back-wall (see Figure 5.1 (a)). This means either both x and z should be small enough so that the defect falls above the affected region or they both should be high enough so that the defect falls outside the region.

An apparent solution for this is moving the array to change the x coordinate of defect, so that it does not fall within that region, but this might not always be achievable and would reduce the angular window of the extracted S-matrix. Therefore, the desired array aperture can be limited by the geometrical features and defect location and this must be included as part of any inspection development for array-based characterisation.

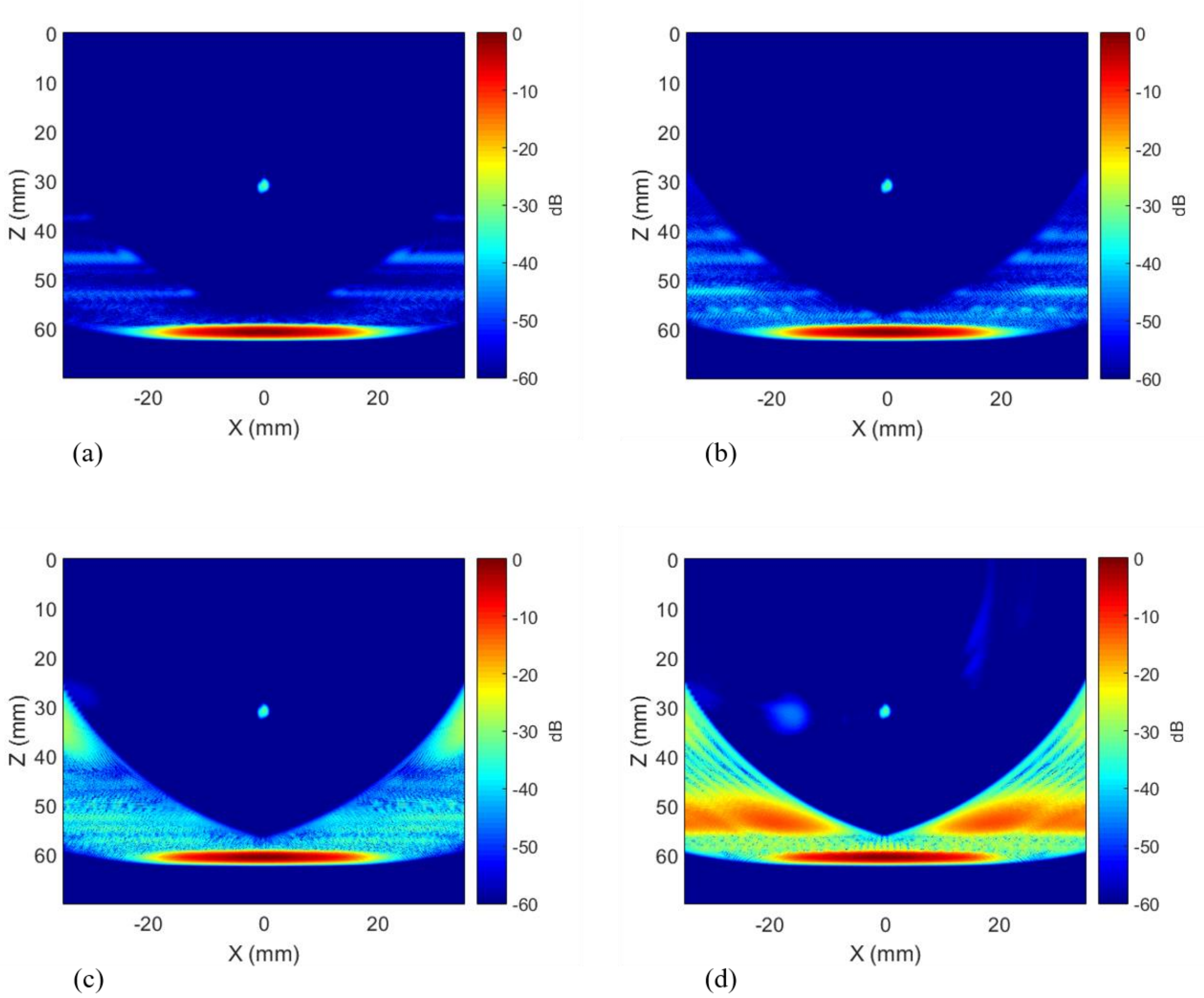

Figure 5.7: Back-wall imaging artefact against different array pitch sizes of (a) 0.25λ, (b) 0.5λ, (c) 1λ and (d) 2λ, while the array aperture size is fixed at 37.7 mm with centre frequency of 5 MHz. The simulated defect here is 1mm, 30°.

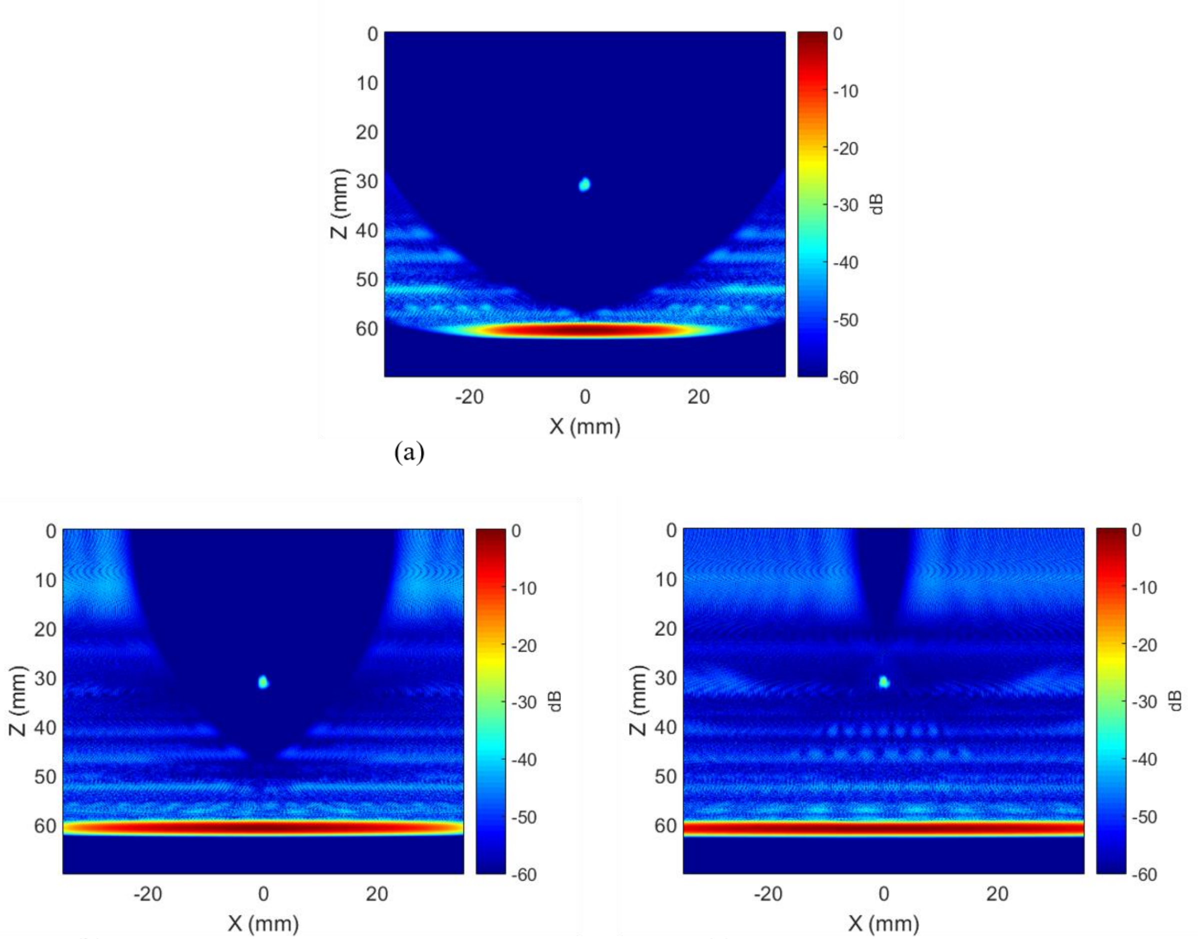

(a)

(b)

(c)

Figure 5.8: Back-wall imaging artefact against different array aperture sizes of (a) 37.7 mm, (b) 75.5 mm and (c) 113.2 mm, while the array pitch size is fixed 0.5λ with centre frequency of 5 MHz. The simulated defect here is 1mm, 30°.

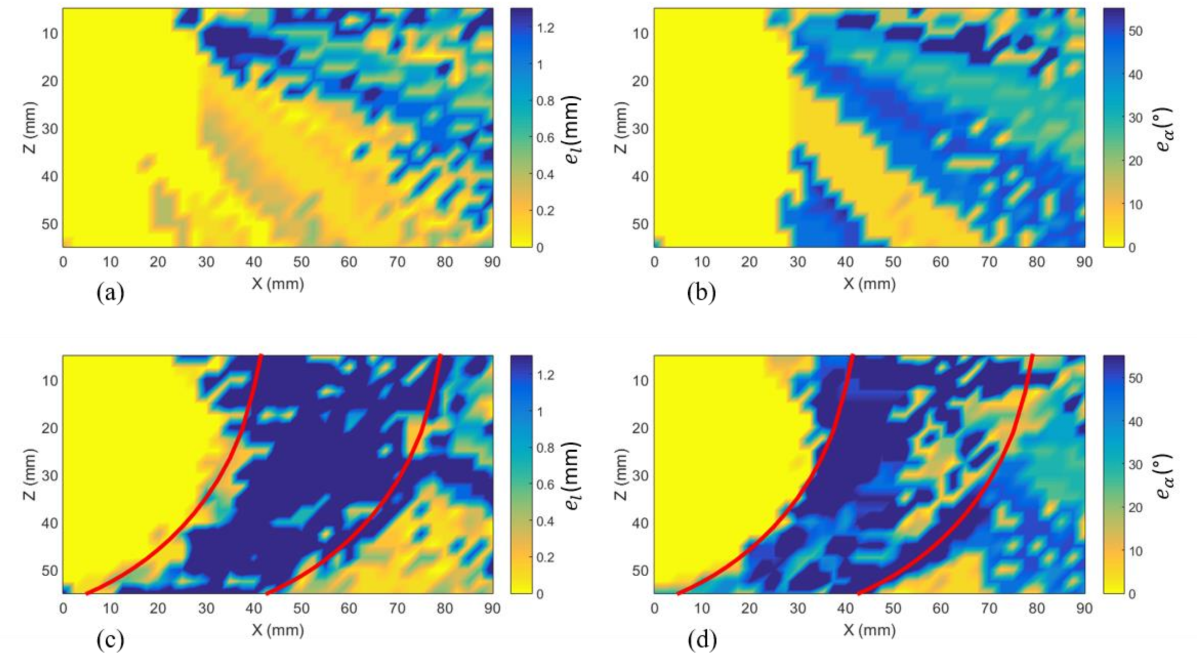

Figure 5.9: Spatial map of the impact of back-wall artefact on characterising a crack-like defect (l = 1 mm, α = 30°) using a 64-element array with pitch of 0.5λ (0.59 mm) and centre frequency of 5 MHz. (a) error in size and (b) error in orientation angle without the presence of a wall. (c) error in size and (d) error in orientation angle with the presence of a wall. Red lines indicate the actual edges of the back-wall artefact.

5.4 Crack Characterisation Case Study

In order to design an optimal array specifically for characterisation, a case study of a particular scenario is considered. This optimal design could be simply the best performing configuration, or the lowest-frequency or lowest-cost array to achieve a required level of performance, etc. Here we take a 1 mm, 30° crack positioned at 30 mm directly below the array inside a material with similar properties to a moderate-noise mild steel (EN24), where the back-wall is 60 mm away from the array. A plot of characterisation performance is then produced to find the optimal combination of array aperture and centre frequency. Figure 5.10 shows characterisation error in (a) size and (b) orientation angle against aperture size and centre frequency, where a back-wall is present at z = 60 mm, a noise level of A=20 has been added to the simulation and 120 noise realisations have been used. The pitch size is kept at half wavelength as before. It should be noted that, when the centre frequency is too low and aperture size is too small, the whole array aperture can be smaller than 4λ, and therefore the S-matrix extraction using subarray approach cannot be performed (see Chapter 2, section 2.4.2), hence the empty results in Figure 5.10 (a) and (b). Figure 5.10 shows rapidly reducing characterisation performance when the aperture exceeds 100 mm which is due to the back-wall artefacts overlapping the defect location. Indeed, equation (5.1) reveals that the maximum acceptable aperture is 104 mm (shown with white dashed lines on Figure 5.10). In this scenario, an optimal array can be the lowest-cost array capable of achieving a given level of performance, considering the manufacturing limitations such as minimum pitch size (if frequency is too high, then pitch might be too small to be manufactured), maximum frequency, cost of adding elements, etc. For example, if for this case study, the required accuracy (i.e. maximum acceptable errors) are 0.2 mm and 10° for size and orientation angle respectively, and the limiting manufacturing factor is the maximum achievable centre frequency at 8 MHz, and the dominating cost factor is the number of elements, then Figure 5.10 (c) can be plotted which shows a binary representation of acceptable characterisation errors, where a black cross means the required accuracy (for both size and orientation) is satisfied and a blue empty circle means it is not satisfied. As we move towards the larger aperture sizes, number of elements increase linearly (when frequency is fixed) and as we move towards the higher frequencies, the number of elements increase again linearly (when aperture size is fixed) due to the reduction in wavelength and pitch size. This means, the number of elements and therefore the cost of the array increase as we move towards the top right of the figures (with high frequencies and large apertures) and the optimal parameters are the ones that are closest to the bottom left. Therefore, from Figure 5.10 (c), the optimal combination of aperture and centre frequency that satisfies both size and orientation accuracy is aperture of 75 mm and centre frequency of 3 MHz (the cross on the plot pointed by a black arrow). Such array would have a pitch of 0.98 mm, with 78 elements. In another scenario, if the requirement is to achieve the same level of performance as above but with the lowest possible centre frequency where the size of array aperture does not exceed 65 mm, Figure 5.10 (c) can be used again to identify the combination of aperture and centre frequency to satisfy the new requirements. Therefore, the new optimal array would have a centre frequency of 5 MHz with an aperture in the range of 55 – 65 mm (the circled region on the plot pointed by a black arrow). Such array would have a pitch of 0.59 mm, with minimum 95 and maximum 111 elements. Hence it is apparent that the optimal array for characterisation depends subtly on the optimisation cost function by definition.

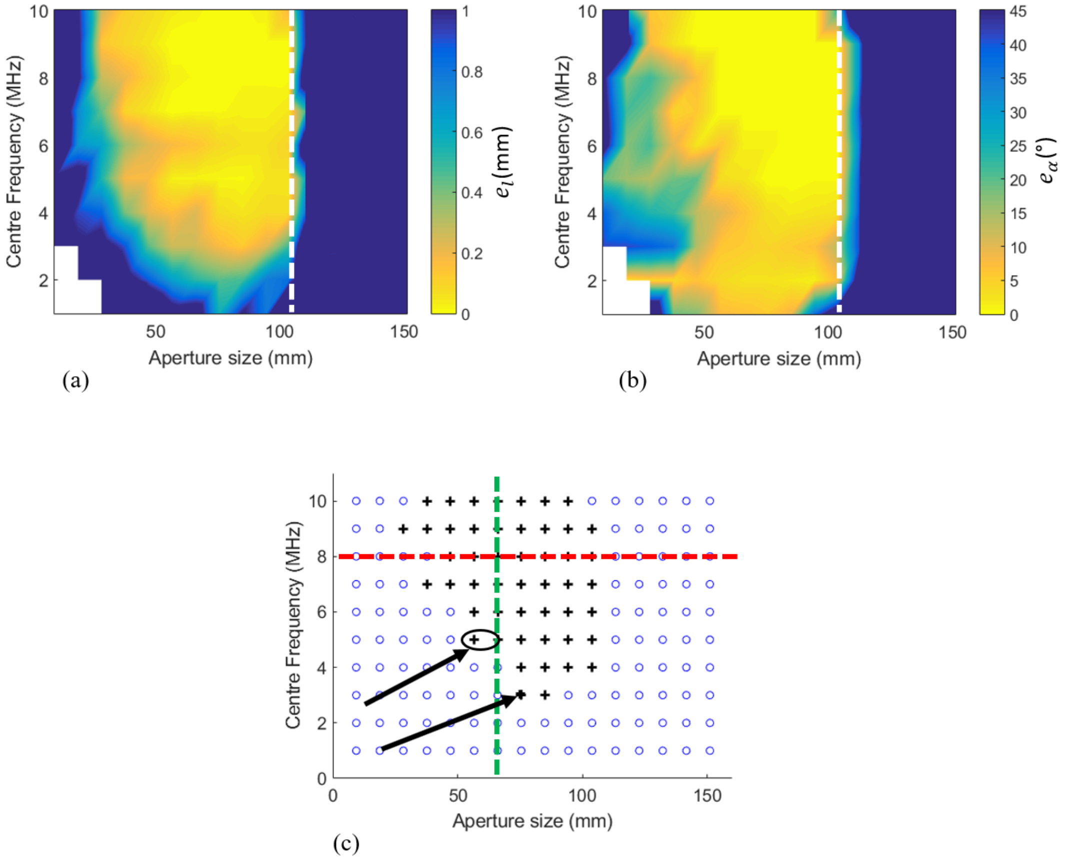

(a)

(b)

(c)

Figure 5.10: (a) error in size and (b) error in orientation angle of a simulated crack-like defect (l = 1 mm, α = 30°) with each plot showing this error as a function of array aperture size and centre frequency. (c) is a binary representation of the area where the maximum characterisation errors in size and orientation angle are both satisfied (black crosses) and where it is not satisfied (blue circles).

5.5 Experimental Validation

In order to validate the models used for simulation of crack-like defects and material noise, experimental characterisation results have been taken and compared with the simulated results. Figure 5.13 shows a comparison between the errors in characterising simulated crack-like defects with simulated noise and characterising real experimental crack-like defects (EDM notches cut with a 0.1 mm thick wire) in bright mild steel (080A15). This is the same sample used in Chapter 4. Figure 5.11 shows the experimental setup and a schematic diagram of the defects and Figure 5.12 shows photos of the actual samples. All experiments are carried out by me using an array controller manufactured by Peak NDT and phased arrays manufactured by Imasonic. Array parameters are shown in Table 5.1 and Table 5.2 shows the details of the experimental defects. As before, due to the difficulty in manufacturing real cracks with different orientation angles, EDM notches were used as the closest manufactured crack-like defects. In order to plot the error in characterising simulated crack-like defects, 120 noise realisations have been used for each defect and the maximum error (dashed lines), minimum error (dotted lines) and mean error (solid lines) are plotted against aperture size. For the experiments, each error bar represents 5 experimental measurements along the y-direction (in thickness direction) and shows the mean error of the 5 measurements and the maximum and minimum errors. Different aperture sizes in the experimental measurements were achieved by turning off the outer elements in post-processing. The left and right columns in Figure 5.13 show error in size and orientation angle respectively. Rows one to four from the top represent defects A to D respectively (see Table 5.2). Figure 5.13 suggests a good overall agreement between the experimental and simulated characterisation errors. The average error differences between simulation and experimental results in size characterisation is 0.31 mm and in orientation characterisation is 2.50°. As explained in Chapter 4, section 4.5, the small differences seen, are thought to be due to the assumption in simulations that crack-like defects have zero width. So, the diffraction from experimental notch tip (i.e. the S-matrix) would be slightly different from the zero-width simulated crack-like defect tips, particularly when the array aperture is larger, and the crack is oriented at 30°. Experimental results can also be affected by the steel block's surface and coupling conditions at specific locations and the spatial variation in grain noise. Furthermore, the ideal input pulse in simulations cannot be exactly reproduced using the experimental electronics. For defect A, if the requirement is to find the least number of elements needed to achieve an accuracy of 0.2 mm in size and 2° in orientation characterisation, while the centre frequency is 2 MHz, then the experimental data suggests an array aperture of 62.5 mm (40 elements) and the model would suggest an aperture of 75 mm (48 elements).

Table 5.1: Array transducer parameters used in experiments.

Array parameter	Value
Number of elements	64
Element width (mm)	1.32
Element pitch (mm)	1.57
Element length (mm)	22
Centre frequency (MHz)	2
Bandwidth (-6 dB) (MHz)	1.45 - 2.55

Table 5.2: Details of crack-like defects used in experiments.

Defect	Z (mm)	Length (mm)	Orientation angle (°)
A	20	1	0
B	50	1	0
C	20	1	30
D	50	1	30

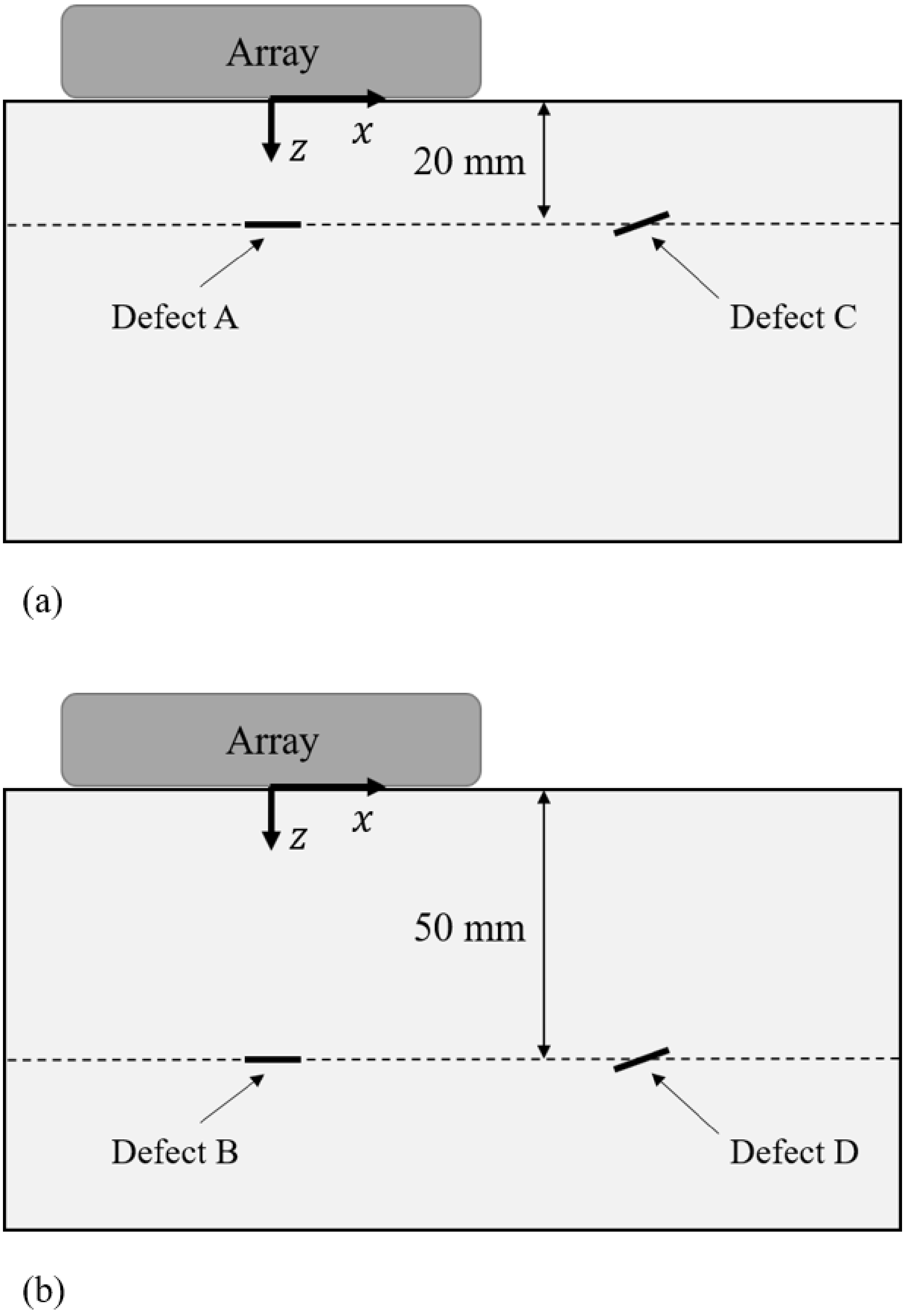

Figure 5.11: Schematic diagram of the experimental setup and defects (EDM notches). (a) shows defects A and C and (b) shows defects B and D from Table 5.2.

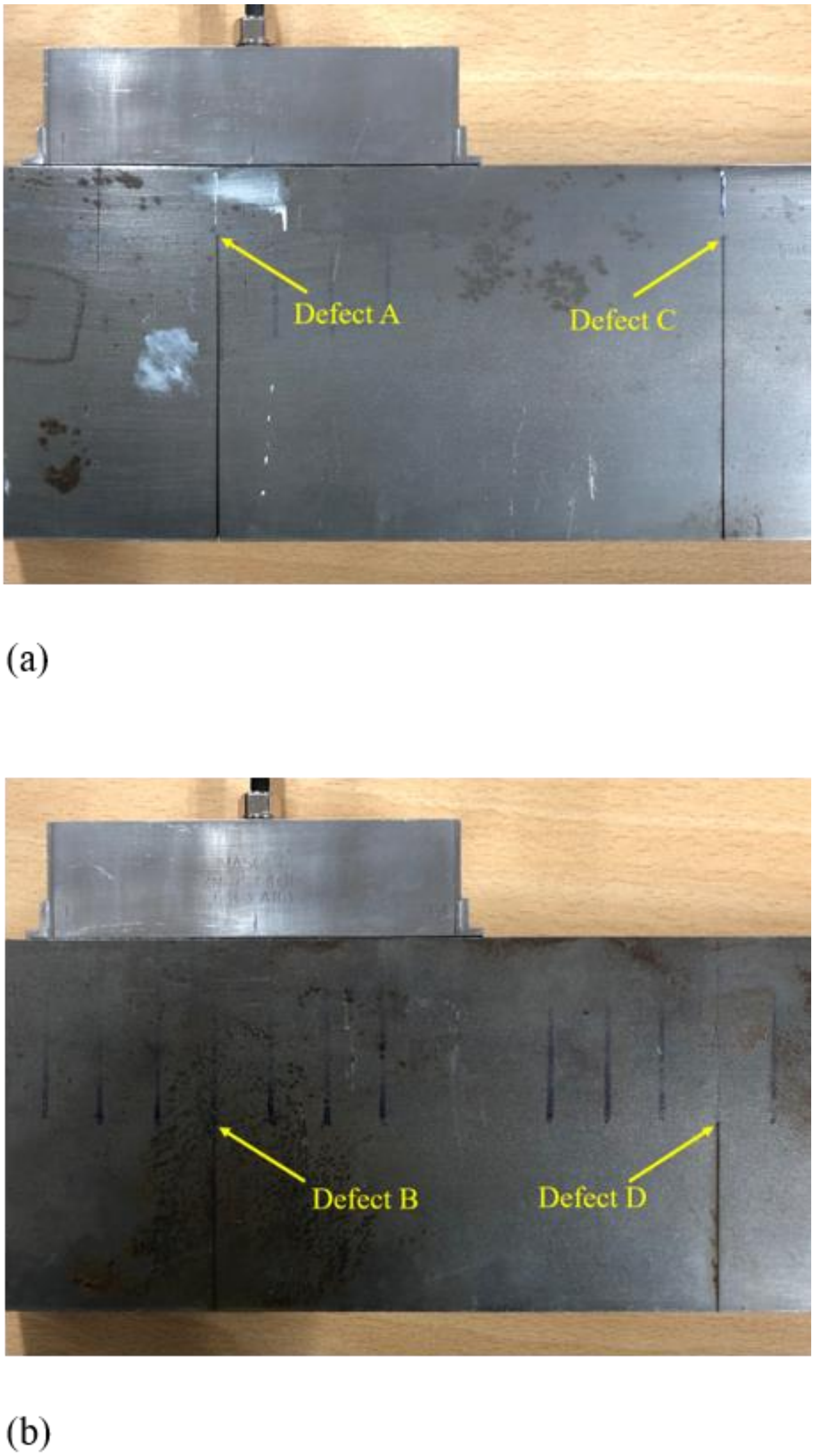

Figure 5.12: Photos of the actual samples corresponding to Figure 5.11.

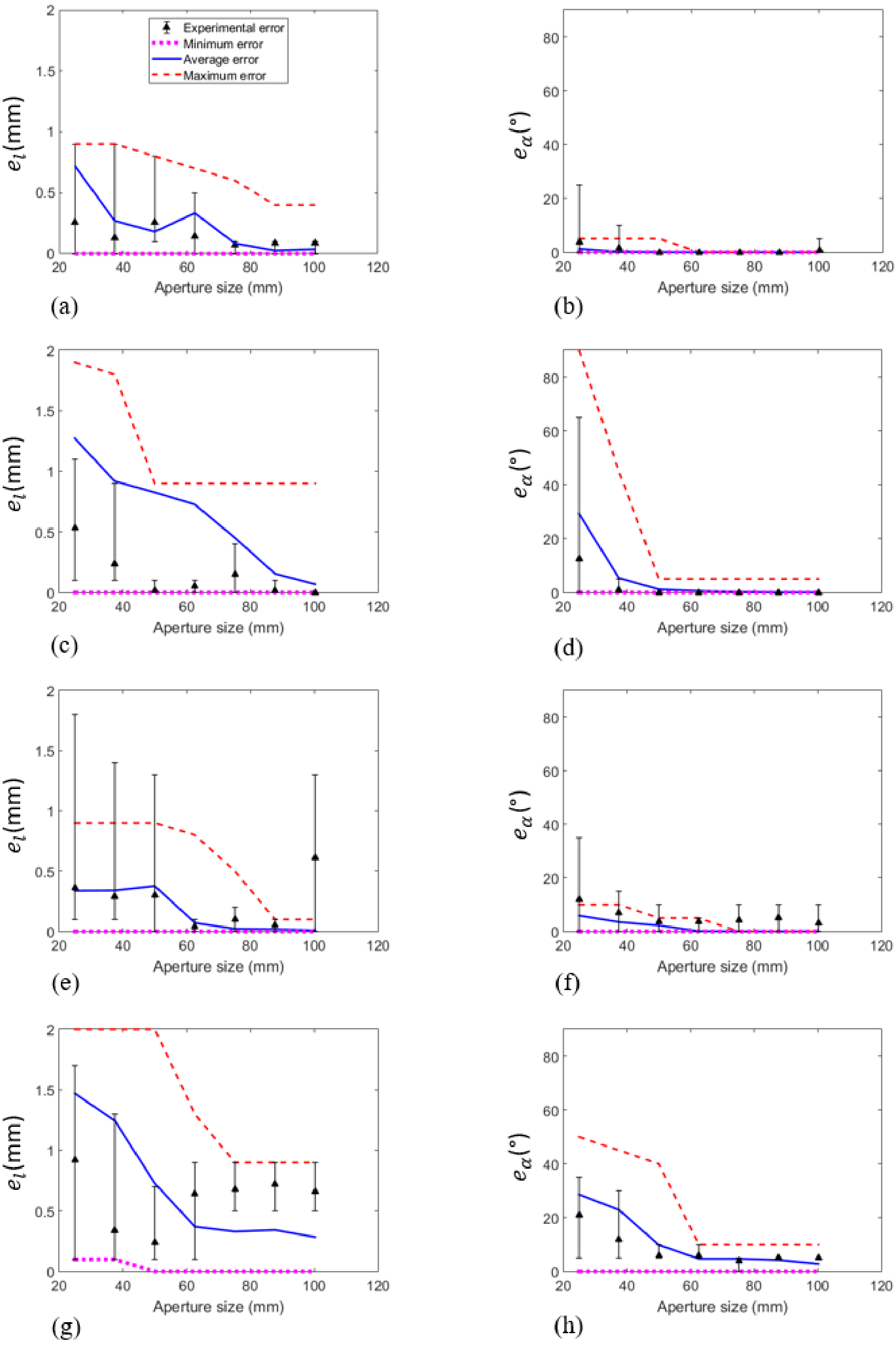

(a) (b)

(c) (d)

(e) (f)

(g) (h)

Figure 5.13: Experimental error in measuring (a), (c), (e), (g) size and (b), (d), (f), (h) orientation angle of two different crack-like defects (l = 1 mm, α = 0° and l = 1 mm, α = 30°) at two different depths. Rows one to four from the top represent defects A to D respectively. Array specifications are given in Table 5.2.

5.6 Implications for NDE

In the field of NDE, there has been a significant focus on development of defect characterisation algorithms, which are designed to be used with the typical and readily available ultrasonic arrays. The approach proposed here is believed to be the first study on the optimisation of array design specifically for the purpose of defect characterisation. The main finding of this Chapter is that the typical arrays, which are normally optimised for imaging, may not necessarily be optimal for all defect characterisation scenarios and therefore after defect detection, a different array design might be needed for the sole purpose of characterisation to the desirable level of accuracy. Like the last Chapter, here some assumptions had to be made due to the large number of variables. For example, the pitch size is kept at 0.5λ and the element width and directivity are assumed to be fixed. The optimal array would also depend on the method of characterisation and the types of defects. It was also discovered that there is no optimal array that would be ideal for all configurations and for any specific scenario such as material noise, type of defect, manufacturing limits, etc. the optimal design would vary. This suggests that for a higher level of characterisation accuracy, arrays need to be designed for the purpose, depending on the characterisation algorithm and the critical variables, in order to enhance the accuracy and capability of the algorithms.

5.7 Conclusion

The effects of different array parameters as well as geometrical features on defect characterisation are investigated to explore the optimal array for characterisation. The inspection of small crack-like defects (which are one of the most challenging types of defects for characterisation) were simulated using the linear systems hybrid model described in Chapter 3. The *database similarity metric method* was used, which works by measuring the S-matrices from defects and comparing them to a database of pre-computed S-matrices. The effect of array aperture size and centre frequency as well as material noise and TFM back-wall’s artefact were considered. It was shown that optimisation for characterisation leads to different solutions depending on the specific requirements, such as the required level of accuracy or cost. In a case study, the key factors impacting the performance of characterisation for a 1 mm, 30° crack in a moderate-noise mild steel have been identified and in two separate scenarios, based on an example of required accuracy of 0.2 mm for size and 10° for orientation angle with the manufacturing limit of 8 MHz as the maximum achievable centre frequency, the optimal arrays were found to be one with 78 elements, 3 MHz centre frequency and pitch of 0.98 mm and another one with 95 to 111 elements, 5 MHz centre frequency and pitch of 0.59 mm. It was further shown that the optimal array design can vary significantly depending on the size and orientation of the crack. For example, a larger aperture might be required for cracks with steeper orientation angles. It was also shown that the back-wall’s artefact has a major impact on characterisation and the affected region can be identified by knowing the back-wall geometry and location of the defect. Finally, the forward model for defect and noise simulation has been verified by comparing the characterisation errors found in simulations with those measured in experiments on steel samples with EDM notches. The average of differences between simulation and experimental results were 0.31 mm in size and 2.50° in orientation characterisation.

Chapter 6

Conclusion

6.1 Thesis Review

In Chapter 2, a review of the literature on ultrasonic phased arrays was presented, discussing their capabilities and applications. The typical array arrangements (1D, 2D and annular) were introduced and discussed. It was shown that phased array transducers can produce the fields generated from a range of different single element probes, and elements are able to fire signals either in-phase or different delay laws can be applied to steer or focus the beam. The concept of full matrix capture (FMC) was also explained, which is a matrix containing the time domain signals (A-Scans) transmitted and received by every pair of elements. Moreover, the concept of the scattering coefficient matrix (S-matrix) was discussed, which contains the angular scattering information of the defect. It was further shown that FMC data can be used for post-processing to generate images and characterise defects. Some of the imaging techniques including the TFM and IWEX methods as well as defect characterisation approaches, which take advantage of S-matrices, such as the *database similarity metric method* were presented, and their applications were reviewed.

Chapter 3 introduced the hybrid model for simulation of an array FMC data set as well as the noise model used to replicate material grain noise. The generation of the input signal in time-domain was shown and the concepts of array element directivity function and beam spreading were explored. A 2D fast semi-analytical model was explained, which is used to simulate the S-matrix of planar cracks, and finally, the model was validated by comparing the TFM images and S-matrices of simulated cracks with those measured in experiments and an excellent agreement between the experimental and simulated results was shown with an average correlation coefficient (CC) of 0.9927 between simulated and experimentally extracted S-matrices.

A spatial mapping approach was proposed in Chapter 4, which was used to assess the performance of characterisation methods. This method takes advantage of modern computer power to rapidly simulate the FMC data of defects at arbitrary locations and then apply the characterisation method of interest to each simulated defect. In a case study, the performance of the *database similarity metric method* was studied and by using spatial assessment, the governing factors impacting its performance were identified. Grain noise was found to have a significant effect on particular regions whilst leaving other areas relatively unaffected and it was further shown that the location of regions of good performance can vary considerably depending on the size and orientation of the crack. The defect SNR and the S-matrix uniqueness was shown to govern this spatial distribution characterisation performance. Then simple models were developed to allow prediction of the regions of good performance. Finally, the spatial error maps were verified by comparing the characterisation errors found in simulation with those measured in experiments. The average of size differences between simulation and experimental results was 0.20 mm and the average of orientation angle differences was 5.87°.

In Chapter 5, the impact of different array parameters and geometrical features on defect characterisation was studied to explore the optimal array for characterisation. Using the linear systems hybrid model described in Chapter 3, the inspection of small crack-like defects was simulated, and the *database similarity metric method* was used. The effect of array aperture size and centre frequency as well as material noise and TFM back-wall's artefact were examined. It was shown that array optimisation for characterisation leads to different solutions depending on the specific requirements, such as the required level of accuracy. In a case study, the key parameters impacting the performance of characterisation for a 1 mm, 30° crack in a mild steel were identified and in two separate scenarios, based on an example of required accuracy and manufacturing limits, the optimal arrays were identified as one with 78 elements, 3 MHz centre frequency and pitch of 0.98 mm and another one with 95 to 111 elements, 5 MHz centre frequency and pitch of 0.59 mm. It was further shown that the optimal array design can vary significantly depending on the size and orientation of the crack. For example, a larger aperture might be required for cracks with steeper orientation angles. Also, the back-wall's artefact was shown to have a major impact on characterisation and the affected region can be identified by knowing the back-wall geometry and location of the defect. Finally, the forward model used in simulation of defects and noise was verified by comparing the characterisation errors found in simulations with those measured in experiments. The average of differences between simulation and experimental results were found to be 0.31 mm and 2.50° in size and orientation angle respectively.

6.2 Key Contributions and Implications for NDE

It is expected that with the increasing availability of computing power, more complex defect characterisation algorithms will emerge and in order to identify their strengths and weaknesses, a robust evaluation method is required [122]. The assessment approach described in Chapter 4 is believed to be the first example of an assessment methodology for defect characterisation in NDE, which provides a comprehensive and quantitative evaluation. The main finding of this research is the fact that in a defect characterisation method, a wide range of variables can affect the performance and therefore, they all need to be taken into consideration for a proper evaluation of algorithms. For example, in a method that is based on extraction of the defect's S-matrix, the extraction algorithm is critical and as an example, the frequency filter bandwidth can impact the results significantly. The performance of characterisation methods also depends on many other conditions such as the ultrasonic instrument that is being used and its properties, the level and type of present noise and the position, shape and type of defects. Ideally, all these variables need to be taken into consideration in order to fully examine the performance of a characterisation approach, otherwise, assumptions must be made to reduce the number of variables. In Chapter 4, it was attempted to consider some of these variables (i.e. level of noise, location, size and orientation of cracks). By knowing what variables can affect a specific defect characterisation method and to what extent, the algorithm can be fine-tuned and improved to achieve the desired performance for specific scenarios. The proposed approach is general and hence has the potential to be used in or adopted to other occasions and can be extended to any characterisation method, defect type and array configuration.

On the other hand, characterisation algorithms are often designed to be used with the typical and readily available ultrasonic arrays. The approach proposed in Chapter 5 is believed to be the first study on the optimisation of array design specifically for the purpose of defect characterisation. The main finding of this Chapter was that the typical arrays, which are generally optimised for imaging, may not necessarily be optimal for all defect characterisation scenarios and hence, after defect detection, a different array design might be required for the sole purpose of characterisation to the desirable level of accuracy. As before, due to the large number of variables, some assumptions had to be made. For example, the array pitch size was kept constant at 0.5λ and the element width and directivity were assumed to be fixed. It was found that the optimal array would depend on the method of characterisation and the types of defects, and more importantly, there is no optimal array that would be ideal for all configurations and for any specific scenario such as material noise, type of defect, manufacturing limits, etc. the optimal design would vary. This means, for a better characterisation result, the approach proposed in this thesis can be used and fine-tuned based on the method of characterisation and critical variables to allow the selection of an array to enhance the accuracy and capability of the characterisation methods.

6.3 Future Work

In both Chapters 4 and 5, assumptions were made on some of the variables such as the array pitch. However, in industrial applications, these variables might be unknown (i.e. to be optimised or assessed) and instead, some others might be known/fixed. The presented approaches in this thesis can be modified to incorporate such differences. For example, instead of optimising arrays for aperture and centre frequency, they can be optimised for pitch size or element directivity.

With future advancements in computer power and FE analysis, the noise simulation used in Chapter 5, can be replaced by a more accurate numerical model to allow a more precise selection of optimal array designs. Also, all the simulations and experiments in this thesis assume a 2-dimensional geometry of the defect and wave scattering. However, the proposed approaches, can be extended to 3-dimentional geometries, although the computational cost of the forward modelling would increase. Hence, the proposed assessment methodology in Chapter 4 could be extended to produce a 3D spatial map, in order to assess more characterisation methods that would be possible with 2D arrays. The array optimisation approach in Chapter 5 can also be extended for optimisation of other types of arrays such as

2D and annular arrays. Both proposed approaches can also be used and modelled with complex structured materials which are widely used in industry (e.g. in nuclear power plants).

Another key direction for future work is to apply the ideas developed in this thesis to more industrially relevant samples/scenarios, in order to understand how such approaches can be made to work in practice and what their practical benefits are. Also, combining the ideas in Chapters 4 and 5 together can potentially be beneficial and lead to solutions for an optimal combination of characterisation method and array design. This can potentially be done by trained machine learning models, where for any given scenario, the optimal array and characterisation approach are selected by the artificial intelligence for the operator.

Finally, the approaches proposed in this thesis can potentially be used in other inspection setups (such as electromagnetic techniques) as well as other fields such as sonar and radar, all of which have similar objectives and challenges in target detection and characterisation.

References

[1] Callister WD. Materials Science and Engineering: an Introduction. New York: John Wiley & Sons, Inc. 1997;

[2] Dobmann G., and Cioclov D, and Kurz J H. The Role of Probabilistic Approaches in NDT Defect-Detection, -Classification, and -Sizing. Welding in the World. 2007;51(5):9–15.

[3] Achenbach JD. Quantitative nondestructive evaluation. International Journal of Solids and Structures. 2000;37(1–2):13–27.

[4] Worden K, Farrar CR, Manson G, Park G. The fundamental axioms of structural health monitoring. Proceedings of the Royal Society A: Mathematical, Physical and Engineering Sciences. 2007;463(2082):1639–64.

[5] Bray DE, Stanley RK. Nondestructive evaluation: a tool in design, manufacturing and service. revised ed. Boca Raton: CRC Press; 1997.

[6] Kundu T. Ultrasonic nondestructive evaluation: engineering and biological material characterization. Boca Raton: CRC Press; 2004.

[7] Farrar CR, Worden K. An introduction to structural health monitoring. Philosophical Transactions of the Royal Society A. 2007;365(1851):303–15.

[8] Kelly, Stephen P., Farlow, Roger, Hayward, Gordon. Applications of Through-Air Ultrasound for Rapid {NDE} Scanning in the Aerospace Industry. IEEE Transactions on Ultrasonics, Ferroelectrics, and Frequency Control. 1996;43(4):581–91.

[9] Brotherhood CJ, Drinkwater BW, Freemantle RJ. An ultrasonic wheel-array sensor and its application to aerospace structures. Insight: Non-Destructive Testing and Condition Monitoring. 2003;45(11):729–34.

[10] Cuadra J, Vanniamparambil PA, Hazeli K, Bartoli I, Kontsos A. Damage quantification in polymer composites using a hybrid NDT approach. Composites Science and Technology. 2013;83:11–21.

[11] Pitropakis I, Pfeiffer H, Wevers M. Crack detection in aluminium plates for aerospace applications by electromagnetic impedance spectroscopy using flat coil sensors. Sensors and Actuators, A: Physical. 2012;176:57–63.

[12] Yang B, Huang Y, Cheng L. Defect detection and evaluation of ultrasonic infrared thermography for aerospace CFRP composites. Infrared Physics and Technology. 2013;60:166–73.

[13] Gunarathne GPP, Keatch RW. Novel techniques for monitoring and enhancing dissolution of mineral deposits in petroleum pipelines. Ultrasonics. 1996;34(2–5):411–9.

[14] Pandey MD. Probabilistic models for condition assessment of oil and gas pipelines. NDT and E International. 1998;31(5):349–58.

[15] Zahran O, Al-Nuaimy W. Automatic segmentation of time-of-flight diffraction images using time-frequency techniques - Application to rail-track defect detection. Insight: Non-Destructive Testing and Condition Monitoring. 2004;46(6):338–43.

[16] Pohl R, Erhard A, Montag HJ, Thomas HM, Wüstenberg H. NDT techniques for railroad

wheel and gauge corner inspection. NDT and E International. 2004;37(2):89–94.

[17] Gallagher GP, Leiper Q, Williamson R, Clark MR, Forde MC. The application of time domain ground penetrating radar to evaluate railway track ballast. NDT and E International. 1999;32(8):463–8.

[18] Colla C, Krause M, Maierhofer C, Höhberger HJ, Sommer H. Combination of NDT techniques for site investigation of non-ballasted railway tracks. NDT and E International. 2002;35(2):95–105.

[19] Topp D, Smith M. Application of the ACFM inspection method to rail and rail vehicles. Insight: Non-Destructive Testing and Condition Monitoring. 2005;47(6):354–7.

[20] Carboni M, Beretta S. Effect of probability of detection upon the definition of inspection intervals for railway axles. Proceedings of the Institution of Mechanical Engineers, Part F: Journal of Rail and Rapid Transit. 2007;221(3):409–17.

[21] Dixon S, Edwards RS, Jian X. Inspection of rail track head surfaces using electromagnetic acoustic transducers (EMATs). Insight: Non-Destructive Testing and Condition Monitoring. 2004;46(6):326–30.

[22] Oukhellou L, Côme E, Bouillaut L, Aknin P. Combined use of sensor data and structural knowledge processed by Bayesian network: Application to a railway diagnosis aid scheme. Transportation Research Part C: Emerging Technologies. 2008;16(6):755–67.

[23] Yang R, He Y, Gao B, Yun Tian G, Peng J. Lateral heat conduction based eddy current thermography for detection of parallel cracks and rail tread oblique cracks. Measurement. 2015;66:54–61.

[24] Clark R. Rail flaw detection: Overview and needs for future developments. NDT and E International. 2004;37(2):111–8.

[25] Calmon P, Lhémery A, Lecœur-Taïbi I, Raillon R, Paradis L. Models for the computation of ultrasonic fields and their interaction with defects in realistic NDT configurations. Nuclear Engineering and Design. 1998;180(3):271–83.

[26] Madruga FJ, González DA, Mirapeix JM, López Higuera JM. Application of infrared thermography to the fabrication process of nuclear fuel containers. NDT and E International. 2005;38(5):397–401.

[27] Whittle MJ. A review of worldwide practice and experience in the qualification of ultrasonic inspections of nuclear components over the past two decades. Insight: Non-Destructive Testing and Condition Monitoring. 2009;51(3):140–50.

[28] Lee JR, Jeong H, Ciang CC, Yoon DJ, Lee SS. Application of ultrasonic wave propagation imaging method to automatic damage visualization of nuclear power plant pipeline. Nuclear Engineering and Design. 2010;240(10):3513–20.

[29] Drai R, Sellidj F, Khelil M, Benchaala A. Elaboration of some signal processing algorithms in ultrasonic techniques: Application to materials NDT. Ultrasonics. 2000;38(1):503–7.

[30] Ludwig R, Lord W. A Finite-Element Formulation for the Study of Ultrasonic NDT Systems. IEEE Transactions on Ultrasonics, Ferroelectrics, and Frequency Control. 1988;35(6):809–20.

[31] Pardo E, San Emeterio JL, Rodriguez MA, Ramos A. Noise reduction in ultrasonic NDT

using undecimated wavelet transforms. Ultrasonics. 2006;44(SUPPL.).

[32] Rajkumar K V., Rao BPC, Sasi B, Kumar A, Jayakumar T, Raj B, et al. Characterization of aging behaviour in M250 grade maraging steel using eddy current non-destructive methodology. Materials Science and Engineering A. 2007;464(1–2):233–40.

[33] De Goeje MP, Wapenaar KED. Non-destructive inspection of carbon fibre-reinforced plastics using eddy current methods. Composites. 1992;23(3):147–57.

[34] Auld BA, Moulder JC. Review of advances in quantitative eddy current nondestructive evaluation. Journal of Nondestructive Evaluation. 1999;18(1):3–36.

[35] Brence JR, Brown DE. Data mining corrosion from eddy current non-destructive tests. Computers and Industrial Engineering. 2002;43(4):821–40.

[36] Sophian A, Tian GY, Taylor D, Rudlin J. A feature extraction technique based on principal component analysis for pulsed Eddy current NDT. NDT and E International. 2003;36(1):37–41.

[37] Monebhurrun V, Duchêne B, Lesselier D. Three-dimensional inversion of eddy current data for non-destructive evaluation of steam generator tubes. Inverse Problems. 1998;14(3):707–24.

[38] Vasić D, Bilas V, Ambruš D. Pulsed eddy-current nondestructive testing of ferromagnetic tubes. IEEE Transactions on Instrumentation and Measurement. 2004;53(4):1289–94.

[39] Ketcham RA, Carlson WD. Acquisition, optimization and interpretation of x-ray computed tomographic imagery: Applications to the geosciences. Computers and

Geosciences. 2001;27(4):381–400.

[40] Johns RA, Steude JS, Castanier LM, Roberts P V. Nondestructive measurements of fracture aperture in crystalline rock cores using X ray computed tomography. Journal of Geophysical Research. 1993;98(B2):1889–900.

[41] Qin YW, Bao NK. Infrared thermography and its application in the NDT of sandwich structures. Optics and Lasers in Engineering. 1996;25(2-3 SPEC. ISS.):205–11.

[42] Park GS, Park ES. Improvement of the sensor system in magnetic flux leakage-type nondestructive testing (NDT). IEEE Transactions on Magnetics. 2002;38(2 I):1277–80.

[43] Sophian A, Tian GY, Zairi S. Pulsed magnetic flux leakage techniques for crack detection and characterisation. Sensors and Actuators, A: Physical. 2006;125(2):186–91.

[44] Ivanov PA, Zhang Z, Yeoh CH, Udpa L, Sun Y, Udpa SS, et al. Magnetic flux leakage modeling for mechanical damage in transmission pipelines. IEEE Transactions on Magnetics. 1998;34(5 PART 1):3016–9.

[45] Liu B, He L yao, Zhang H, Cao Y, Fernandes H. The axial crack testing model for long distance oil-gas pipeline based on magnetic flux leakage internal inspection method. Measurement. 2017;103:275–82.

[46] Drinkwater BW, Wilcox PD. Ultrasonic arrays for non-destructive evaluation: A review. NDT & E International. 2006 Oct;39(7):525–41.

[47] Van Pamel A. Ultrasonic inspection of highly scattering materials [dissertation]. London: Imperial College London; 2015.

[48] Cheeke JDN. Fundamentals and Applications of Ultrasonic Waves. 2nd ed. Fundamentals and Applications of Ultrasonic Waves. Boca Raton: CRC Press; 2012.

[49] Ying CF, Truell R. Scattering of a plane longitudinal wave by a spherical obstacle in an isotropically elastic solid. Journal of Applied Physics. 1956;27(9):1086–97.

[50] Brind RJ, Achenbach JD, Gubernatis JE. High-frequency scattering of elastic waves from cylindrical cavities. Wave Motion. 1984;6(1):41–60.

[51] Connolly GD, Lowe MJS, Temple JAG, Rokhlin SI. The application of Fermat's principle for imaging anisotropic and inhomogeneous media with application to austenitic steel weld inspection. Proceedings of the Royal Society A: Mathematical, Physical and Engineering Sciences. 2009;465(2111):3401–23.

[52] Callister WD. Materials Science and Engineering: an Introduction. 7th ed. New York: Wiley; 2006.

[53] Chapman RK. A system model for the ultrasonic inspection of smooth planar cracks. Journal of Nondestructive Evaluation. 1990;9(2–3):197–210.

[54] Boström A, Wirdelius H. Ultrasonic probe modeling and nondestructive crack detection. The Journal of the Acoustical Society of America. 1995;97(5):2836–48.

[55] Bovik P, Bostrom A. A model of ultrasonic nondestructive testing for internal and subsurface cracks. Journal of Acoustic Society of America. 1997;102(November 1997):2723–33.

[56] Glushkov E, Glushkova N, Ekhlakov A, Shapar E. An analytically based computer model for surface measurements in ultrasonic crack detection. Wave Motion.

2006;43(6):458–73.

[57] Schmerr Jr. LW. Fundamentals of Ultrasonic Nondestructive Evaluation: A Modeling Approach [Internet]. New York: Plenum; 1998.

[58] Zhang J, Drinkwater BW, Wilcox PD. Longitudinal wave scattering from rough crack-like defects. IEEE Transactions on Ultrasonics, Ferroelectrics, and Frequency Control. 2011;58(10):2171–80.

[59] Ogilvy JA. Wave scattering from rough surfaces. Reports on Progress in Physics. 1987;50(12):1553–608.

[60] Thorsos EI. The validity of the Kirchhoff approximation for rough surface scattering using a Gaussian roughness spectrum. Journal of the Acoustical Society of America. 1988;83(1):78–92.

[61] Bass FG, Fuks IM. Wave scattering from statistically rough surfaces. Elmsford: Pergamon; 1979.

[62] Velichko A, Wilcox PD. A generalized approach for efficient finite element modeling of elastodynamic scattering in two and three dimensions. The Journal of the Acoustical Society of America. 2010;128(3):1004.

[63] Smith WD. The Application of Finite Element Analysis to Body Wave Propagation Problems. Geophysical Journal International. 1975;42(2):747–68.

[64] Kelly KR, Ward RW, Treitel S, Alford RM. Synthetic Seismograms: a Finite-Difference Approach. Geophysics. 1976;41(1):2–27.

[65] Schafbuch PJ, Rizzo FJ, Thompson RB. Boundary element method solutions for elastic wave scattering in 3D. International Journal for Numerical Methods in Engineering. 1993;36(3):437–55.

[66] Frehner M, Schmalholz SM, Saenger EH, Steeb H. Comparison of finite difference and finite element methods for simulating two-dimensional scattering of elastic waves. Physics of the Earth and Planetary Interiors. 2008;171(1–4):112–21.

[67] Wilcox PD, Velichko A. Efficient frequency-domain finite element modeling of two-dimensional elastodynamic scattering. The Journal of the Acoustical Society of America. 2010;127(1):155–65.

[68] Bai L, Velichko A, Drinkwater BW. Ultrasonic characterization of crack-like defects using scattering matrix similarity metrics. IEEE Transactions on Ultrasonics, Ferroelectrics, and Frequency Control. 2015;62(3):545–59.

[69] Bai L, Velichko A, Drinkwater BW. Characterization of defects using ultrasonic arrays: A dynamic classifier approach. IEEE Transactions on Ultrasonics, Ferroelectrics, and Frequency Control. 2015;62(12):2146–60.

[70] Velichko A, Bai L, Drinkwater BW. Ultrasonic defect characterization using parametric-manifold mapping. Proceedings of the Royal Society A: Mathematical, Physical and Engineering Science. 2017;473(2202):20170056.

[71] Baby S, Balasubramanian T, Pardikar RJ, Palaniappan M, Subbaratnam R. Time-of-flight diffraction (TOFD) technique for accurate sizing of surface-breaking cracks. Insight: Non-Destructive Testing and Condition Monitoring. 2003;45(6):426–30.

[72] Blitz J, Simpson G. Ultrasonic methods of non-destructive testing. 1st ed. London: Chapman & Hall; 1996.

[73] Holmes C, Drinkwater BW, Wilcox PD. Post-processing of the full matrix of ultrasonic transmit–receive array data for non-destructive evaluation. NDT & E International. 2005;38(8):701–11.

[74] Pörtzgen N, Gisolf D, Blacquière G. Inverse wave field extrapolation: A different NDI approach to imaging defects. IEEE Transactions on Ultrasonics, Ferroelectrics, and Frequency Control. 2007;54(1):118–27.

[75] Zhang J, Drinkwater BW, Wilcox PD. The Use of Ultrasonic Arrays to Characterize Crack-Like Defects. Journal of Nondestructive Evaluation. 2010;29(4):222–32.

[76] Felice M V., Velichko A, Wilcox PD. Accurate depth measurement of small surface-breaking cracks using an ultrasonic array post-processing technique. NDT & E International. 2014 Dec;68:105–12.

[77] Krautkrämer J, Krautkrämer H. Ultrasonic Testing of Materials. Springer. 1983.

[78] Birks AS, Green Jr RY MP. Ultrasonic Testing: Nondestructive Testing Handbook. American Society for Nondestructive. 1991;893.

[79] Martínez O, Akhnak M, Ullate LG, Montero de Espinosa F. A small 2D ultrasonic array for NDT applications. NDT and E International. 2003;36(1):57–63.

[80] Norton SJ. Annular array imaging with full-aperture resolution. The Journal of the Acoustical Society of America. 1992;92(6):3202–6.

[81] Mondal SC, Wilcox PD, Drinkwater BW. Design of Two-Dimensional Ultrasonic Phased Array Transducers. Journal of Pressure Vessel Technology. 2005;127(3):336.

[82] Shung KK. The principle of multidimensional arrays. European Journal of Echocardiography. 2002;3(2):149–53.

[83] Casula O, Poidevin C, Cattiaux G, Dumas P. Control of complex components with smart flexible phased arrays. AIP Conference Proceedings. 2006;820 I:829–36.

[84] Akhnak M, Martinez O, Ullate LG, Montero De Espinosa F. 64 Elements two-dimensional piezoelectric array for 3D imaging. Ultrasonics. 2002;40(1–8):139–43.

[85] Hayward G, Bennett J. Assessing the influence of pillar aspect ratio on the behavior of 1-3 connectivity composite transducers. IEEE Transactions on Ultrasonics, Ferroelectrics, and Frequency Control. 1996;43(1):98–108.

[86] Wooh S-C, Shi Y. Optimum beam steering of linear phased arrays. Wave Motion. 1999;29(3):245–65.

[87] Berkhout AJ. The Seismic Method in the Search for Oil and Gas: Current Techniques and Future Developments. Proceedings of the IEEE. 1986;74(8):1133–59.

[88] Velichko A. Near-field model of ultrasonic array data. AIP Conference Proceedings. 2017;1806(February).

[89] Felice MV. Ultrasonic Array Inspections For Complex Defects [dissertation]. Bristol: University of Bristol; 2015.

[90] Zhang J, Drinkwater BW, Wilcox PD, Hunter AJ. Defect detection using ultrasonic

arrays: The multi-mode total focusing method. NDT & E International. 2010 Mar;43(2):123–33.

[91] Oralkan Ö, Ergun AS, Johnson JA, Karaman M, Demirci U, Kaviani K, et al. Capacitive micromachined ultrasonic transducers: Next-generation arrays for acoustic imaging? IEEE Transactions on Ultrasonics, Ferroelectrics, and Frequency Control. 2002;49(11):1596–610.

[92] Holmes C, Drinkwater B, Wilcox P. The post-processing of ultrasonic array data using the total focusing method. Insight: Non-Destructive Testing and Condition Monitoring. 2004;46(11):677–80.

[93] Wilcox PD, Holmes C, Drinkwater BW. Advanced reflector characterization with ultrasonic phased arrays in NDE applications. IEEE Transactions on Ultrasonics, Ferroelectrics, and Frequency Control. 2007;54(8):1541–50.

[94] Hunter AJ, Drinkwater BW, Wilcox PD. The wavenumber algorithm for full-matrix imaging using an ultrasonic array. IEEE Transactions on Ultrasonics, Ferroelectrics, and Frequency Control. 2008;55(11):2450–62.

[95] Velichko A, Wilcox PD. Reversible back-propagation imaging algorithm for postprocessing of ultrasonic array data. IEEE Transactions on Ultrasonics, Ferroelectrics, and Frequency Control. 2009 Nov;56(11):2492–503.

[96] Velichko A, Wilcox PD. An analytical comparison of ultrasonic array imaging algorithms. The Journal of the Acoustical Society of America. 2010;127(4):2377–84.

[97] Kline RA. Saft Imaging in Anisotropic Media. Review of Progress in Quantitative

Nondestructive Evaluation. 1999;913–8.

[98] Spies M, Jager W. Synthetic aperture focusing for defect reconstruction in anisotropic media. Ultrasonics. 2003;41(2):125–31.

[99] Wilcox PD. Ultrasonic arrays in NDE: Beyond the B-scan. AIP Conference Proceedings. 2013;33(January 2013):33–50.

[100] Hunter AJ, Drinkwater BW, Wilcox PD. Autofocusing ultrasonic imagery for non-destructive testing and evaluation of specimens with complicated geometries. NDT and E International. 2010;43(2):78–85.

[101] Zhang J, Drinkwater BW, Wilcox PD. Defect characterization using an ultrasonic array to measure the scattering coefficient matrix. IEEE Transactions on Ultrasonics, Ferroelectrics, and Frequency Control. 2008;55(10):2254–65.

[102] Zhang J, Drinkwater BW, Wilcox PD. Effect of roughness on imaging and sizing rough crack-like defects using ultrasonic arrays. IEEE Transactions on Ultrasonics, Ferroelectrics, and Frequency Control. 2012;59(5):939–48.

[103] Gebru H. Assessment of ultrasonic inspection techniques and models for nuclear power plant components [dissertation]. London: Imperial College London; 2013.

[104] Berkhout AJ. Applied seismic wave theory. Amsterdam: Elsevier; 1987.

[105] Drinkwater BW, Bowler AI. Ultrasonic array inspection of the Clifton Suspension Bridge chain-links. Insight. 2009;51(9):491–8.

[106] Ben-Menahem A, Singh SJ. Seismic waves and sources. New York: Springer Verlag;

1981.

[107] Long R, Cawley P. Phased array inspection of irregular surfaces. AIP Conference Proceedings. 2007;894(March 2007):814–21.

[108] Weston M, Mudge P, Davis C, Peyton A. Time efficient auto-focussing algorithms for ultrasonic inspection of dual-layered media using Full Matrix Capture. NDT and E International. 2012;47:43–50.

[109] Pearson K. Mathematical contributions to the theory of evolution. III. Regression, heredity and panmixia. Philosophical Transactions of the Royal Society of London. 1896;A 187:253–318.

[110] Kim J. Intensity based image registration using robust similarity measure and constrained optimization: Applications for radiation therapy [dissertation]. Ann Arbor, Michigan: The University of Michigan; 2004.

[111] Zitová B, Flusser J. Image registration methods: A survey. Image and Vision Computing. 2003;21(11):977–1000.

[112] Sotiras A, Davatzikos C, Paragios N. Deformable medical image registration: A survey. IEEE Transactions on Medical Imaging. 2013;32(7):1153–90.

[113] Miller GF, Pursey H. The field and radiation impedance of mechanical radiators on the free surface of a semi-infinite isotropic solid. In Proceedings of the Royal Society of London A: Mathematical, Physical and Engineering Sciences; 1954. p. 521–41.

[114] Weinstein SB, Ebert PM. Data Transmission by Frequency-Division Multiplexing Using the Discrete Fourier Transform. IEEE Transactions on Communication

Technology. 1971;19(5):628–34.

[115] Wilcox PD. Array imaging of noisy materials. AIP Conference Proceedings. 2011;1335:890–7.

[116] Zhang J, Drinkwater B, Wilcox PD. Comparison of ultrasonic array imaging algorithms for nondestructive evaluation. IEEE Transactions on Ultrasonics, Ferroelectrics, and Frequency Control. 2013;60(8):1732–45.

[117] Van Pamel A, Huthwaite P, Brett CR, Lowe MJS. Numerical simulations of ultrasonic array imaging of highly scattering materials. NDT & E International. 2016;81:9–19.

[118] Felice M V., Velichko A, Wilcox PD, Barden T, Dunhill T. Optimization of ultrasonic array inspections using an efficient hybrid model and real crack shapes. AIP Conference Proceedings. 2015;1650(April):978–86.

[119] Smith JO. Physical Audio Signal Processing [Internet]. W3K publishing; 2010.

[120] Mailloux R. Phased Array Antenna Handbook. 2nd ed. Vol. 19, Sensor Review. Artech House; 2005.

[121] Wooh S-C, Shi Y. Three-dimensional beam directivity of phase-steered ultrasound. The Journal of the Acoustical Society of America. 1999;105(6):3275–82.

[122] Safari A, Zhang J, Velichko A, Drinkwater BW. Assessment methodology for defect characterisation using ultrasonic arrays. NDT & E International. 2018;94(December 2017):126–36.

[123] Jacques F, Moreau F, Ginzel E. Ultrasonic backscatter sizing using phased array -

Developments in tip diffraction flaw sizing. Insight: Non-Destructive Testing and Condition Monitoring. 2003;45(11):724–8.

[124] Bloxham H, Velichko A, Wilcox P. Combining simulated and experimental data to simulate ultrasonic array data from defects in materials with high structural noise. IEEE Transactions on Ultrasonics, Ferroelectrics, and Frequency Control. 2016;PP(99):2198–206.

[125] Margetan FJ, Thompson RB, Yalda-Mooshabad I. Modeling Ultrasonic Microstructural Noise in Titanium Alloys. Review of Progress in Quantitative Nondestructive Evaluation. 1993;1735–42.

[126] Peacocke RD, Graf DH. An Introduction to Speech and Speaker Recognition. Computer. 1990;23(8):26–33.

[127] Doddington GR. Speaker recognition: Identifying people by their voices. Proceedings of the IEEE. 1985;73(11):1651–1664.

[128] Bebis G, Deaconu T, Georgiopoulos M. Fingerprint identification using Delaunay triangulation. Proceedings - 1999 International Conference on Information Intelligence and Systems, ICIIS 1999. 1999;452–9.

[129] Ratha NK, Bolle RM, Pandit VD, Vaish V. Robust fingerprint authentication using local structural similarity. Proceedings of IEEE Workshop on Applications of Computer Vision. 2000;2000-Janua:29–34.